Eindhoven University of Technology

MASTER

Novel deposition of magnetic nanostructures
electron beam induced deposition of magnetic iron

Ellis, T.H.

Award date:
2011

Link to publication

Disclaimer
This document contains a student thesis (bachelor's or master's), as authored by a student at Eindhoven University of Technology. Student theses are made available in the TU/e repository upon obtaining the required degree. The grade received is not published on the document as presented in the repository. The required complexity or quality of research of student theses may vary by program, and the required minimum study period may vary in duration.

General rights
Copyright and moral rights for the publications made accessible in the public portal are retained by the authors and/or other copyright owners and it is a condition of accessing publications that users recognise and abide by the legal requirements associated with these rights.

- Users may download and print one copy of any publication from the public portal for the purpose of private study or research.
- You may not further distribute the material or use it for any profit-making activity or commercial gain

Research carried out as part of an ongoing collaboration between FNA and FEI Company

M.Sc. Thesis

Novel Deposition of Magnetic Nanostructures

Electron Beam Induced Deposition of Iron

T.H. Ellis

February 2011

Supervisors:
dr.ir. R. Lavrijsen
prof.dr.ir. H.J.M. Swagten
dr.ir. J.J.L. Mulders (FEI company)

Eindhoven University of Technology
Department of Applied Physics
Physics of Nanostructures (FNA)

Abstract

Electron Beam Induced Deposition (EBID) is a versatile direct-write material deposition technique. Deposition is achieved by using a focused electron beam to selectively decompose a precursor gas adsorbed on a substrate. Not only does this technique permit nanoscale fabrication in three dimensions, but the large number of precursors available also means a broad range of materials can be deposited.

This work details the EBID of magnetic iron using a novel precursor ($Fe_2(CO)_9$). Deposits containing as much as 80 at.% iron have been achieved. Iron microwires have been characterised as a function of oxygen content. In addition to a structural evolution from polycrystalline iron to polycrystalline iron-oxide, large increases in resistance, and changes in the magnetoresistive mechanism have been observed.

Freestanding iron nanopillars have also been investigated. In a pilot experiment their magnetic influence on domain-wall-motion has been explored, which may be relevant for future spintronic devices such as the recently proposed 'racetrack memory'.

Contents

Introduction **7**

1 Fundamental Concepts **9**

1.1 The EBID Process 9

1.2 Magnetic Deposits 11

1.2.1 Magnetisation Behaviour 11

1.2.2 Magnetotransport 13

1.2.3 Iron Oxides 17

1.3 This and Previous Work 19

1.3.1 A Short Review of Magnetic EBID 19

1.3.2 A New Iron Precursor: A Collaboration with FEI 20

1.3.3 This Work 22

2 Experimental Equipment & Techniques **25**

2.1 The Dualbeam 25

2.1.1 Detectors & Imaging 26

2.1.2 Depositing 28

2.2 Additional Characterisation Tools 29

2.2.1 Transmission Electron Microscopy & Electron Diffraction 29

2.2.2 Atomic Force Microscopy 29

2.2.3 Electrical Methods 30

2.2.4 Kerr Microscopy 30

3 Exploring Iron Microwires **33**

3.1 Deposit Fabrication 33

3.2 Microstructure 34

3.3 Conductivity 37

3.4 Magnetism 39

3.5 Annealing . . . 43
3.6 Conclusions . . . 45

4 Tuning Iron Content **47**
4.1 Production Details . . . 48
4.2 Microstructure . . . 49
4.3 Conductivity . . . 50
4.4 Magnetism . . . 52
4.5 Concluding Discussion . . . 55

5 Functional Magnetic Nanopillars **57**
5.1 Growth Dependencies . . . 57
5.1.1 Beam Current . . . 59
5.1.2 Beam Energy . . . 60
5.2 Beam Induced Heating . . . 62
5.2.1 A Qualitative Description . . . 64
5.2.2 Semi-Quantitative Simulations . . . 65
5.2.3 Concluding Discussion . . . 67
5.3 Preliminary Application: Influencing Domain Wall Motion . . . 69
5.3.1 Experimental Considerations . . . 70
5.3.2 Pilot Experiment . . . 72
5.3.3 Conclusions . . . 77

A Deposit Longevity **83**

B Deposition on Thin Films: Thermal Effects **85**

C Modelling Beam Induced Heating **87**

D Larger Depositions **91**

E Ion Beam Induced Deposition **93**

Introduction

For hundreds, if not thousands of years, the seemingly magical effects of magnetism have been the subject of much intrigue. This fascination has brought with it a desire to understand the phenomenon. Today, ferromagnetism is known to be a result of the alignment of the intrinsic magnetic moment or spin of the electron.

Together with this better understanding have come ever more ingenious and complex applications. Perhaps the best known of these today is the now ubiquitous magnetic hard disk drive. In such devices, nanoscale magnetic information is manipulated billions of times per second. This development remains ongoing. In the case of hard disk drive, further miniaturisation has allowed data density to almost double every 18 months. However, at a certain point, in addition to evolution, a technological revolution is required. One candidate is for such a revolution is spintronics, the union of ordinary electronics (charge transport) and magnetism (spin manipulation).

To permit such substantial development and more specifically, to uncover and realize the next technological revolution, novel nanofabrication techniques are also required. There are currently many methods available to an experimentalist for the deposition of material layers down to monolayer sensitivity. However, for the fabrication of more intricate structures, complex multi-step lithographic techniques are usually required. An alternative, and the subject of this thesis, is *electron beam induced deposition*.

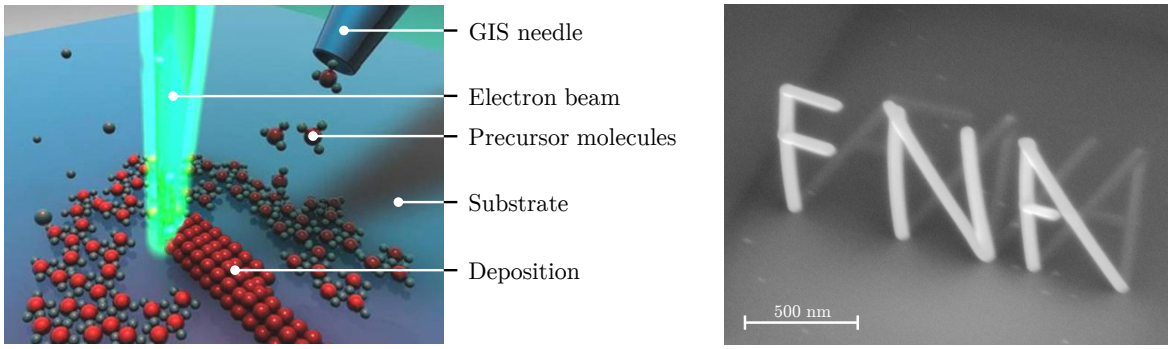

(a) **(b)**

Figure 1: **(a)** The basic concept of EBID: A focused electron beam decomposes a precursor adsorbed on a substrate leaving behind a deposition. **(b)** A SEM image of freestanding iron 'nano letters' deposited by EBID. As indicated by the bright shadow behind the letters, this deposit was produced with the substrate at angle to the electron beam. Each element is just 65 nm in diameter.

The basic principle of EBID is quite simple, and is shown in figure 1a. In a vacuum environment, a gas of precursor molecules is applied to a substrate where it adsorbs. Then, a focused beam of electrons is used to selectively decompose the molecules into volatile and non-volatile

components, the latter of which forms a deposit. Since deposition is limited to a region in the focus of the beam, very selective nanoscale fabrication on almost any surface in three dimensions is possible. This unique pattering ability is perfectly illustrated in figure 1b. Here, by sweeping the electron beam across a tilted substrate, intricate freestanding nanostructures have been effortlessly deposited. Furthermore, with a large number of different precursors available, EBID is also capable of depositing a broad range of materials too, including ferromagnets.

In this thesis, EBID of iron is investigated. The ultimate goal of this line of research is to illustrate the ability of the EBID technique for depositing functional magnetic nanostructures. This work specifically concentrates on two different aspects of this overall goal: the (continued) characterisation of a new iron precursor ($Fe_2(CO)_9$) and preliminary investigations into practical magnetic deposits (chapter 5).

In addition to this introduction, this thesis is divided into five chapters, a conclusion and outlook and a number of appendices. Chapter 1 covers the fundamental principles of EBID in detail and reviews the properties of magnetic deposits made using this technique. In chapter 2, the details of the experimental methods and equipment utilised during this work are presented. Chapter 3 presents the first results, the characterisation of microwire deposits containing a high percentage of iron. Following this, in chapter 4, further characterisation work is presented, but now of microwire deposits containing varying degrees of iron (and oxygen). Chapter 5 describes an investigation into a different kind of deposit, specifically, freestanding nanopillars. It is in this last chapter where the first results on functionality are presented.

Chapter 1

Fundamental Concepts

Expanding on what was discussed in the introduction, in this chapter the fundamental processes of EBID are described. The specific deposition of magnetic material is also further reviewed, including some basic principles of ferromagnetism. At the end of this chapter previous work involving EBID of magnetic materials is briefly reviewed, before a more detailed overview of the work of this thesis is presented.

1.1 The EBID Process

As was mentioned in the introduction and depicted in figure 1a, in theory, EBID is a rather straightforward concept. In practice, things are much more complex. In this section the cause of this complexity is made clear as some of the more important processes relevant to EBID are briefly* detailed.

As shown in figure 1.1a, the EBID process can effectively be decomposed into three interacting systems consisting of the electrons, the precursor, and the substrate. The often complex interactions between these three systems will be considered individually.

Substrate-precursor interactions

In the simplified picture of figure 1a, substrate-precursor interactions involve nothing more than the application of a gas to a surface, where it subsequently remains. In reality substrate-precursor interactions can be substantially more complex. In addition to 'sticking' to the surface (adsorption), the precursor molecules can also be transported across it via diffusion or even detach completely (desorption). The rate with which all these processes occur depends on numerous factors, from the type of precursor and substrate used, to the temperature, to the presence of additional vacuum contaminate species. With the precursor a fundamental component of EBID, this ultimately has a large influence on resulting depositions. Complicating things even further is the fact that after deposition begins, the substrate itself becomes less relevant and it is now, often different, deposition-precursor interactions which must be considered.

These interactions were investigated in detail by Beljaars[4] as will be further discussed at the end of this chapter.

*For a more thorough description see references 1–3.

Electron-substrate interactions

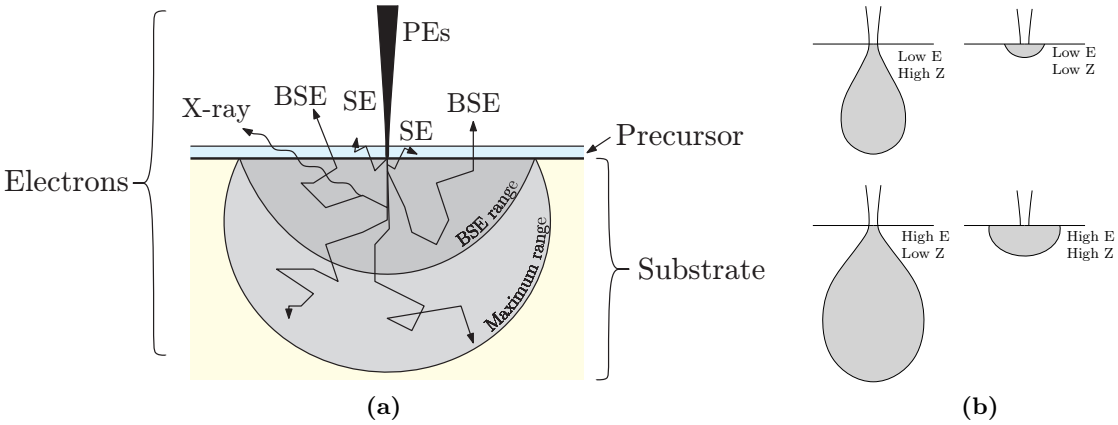

Figure 1.1: **(a)** A schematic illustration of the common processes taking place when a beam of electrons is focused onto a substrate. The primary electrons (PEs) can scatter through the solid, freeing additional electrons, some of which escape the surface in the form of higher energy backscattered electrons (BSEs) or low energy secondary electrons (SEs). The total interaction volume (light grey) and the BSE depth range (dark grey) are also indicated. **(b)** The influence on the interaction volume of beam energy (E) and target atomic number (Z).

A summary of the electron-substrate interactions important in EBID is shown in figure 1.1a. The electrons making up the focused beam are known as primary electrons (PE), and are shown in black in the figure. As these PEs impact the substrate both elastic and inelastic collisions can take place. The energy lost during inelastic collisions can be transferred to other electrons in the solid which can subsequently continue to interact and scatter, even reaching the surface. Depending on their energy, these escaping electrons are commonly classified as either secondary electrons (SEs, $E < 50$ eV) or backscattered electrons (BSEs, $E > 50$ eV). Key to imaging in SEMs, these surface electrons also play a very important role in precursor dissociation in EBID, as will be discussed below. As shown in figure 1.1b, the depth to which these electron scattering processes can occur depends both on the initial energy of the PEs and the material properties of the substrate. Higher energies and lower atomic numbers lead to increased penetration depths and vice versa.

In addition to SE and BSE scattering a number of other processes can also take place. Less important to EBID, but still significant, these include Auger and photoelectron processes, and X-ray and bremsstrahlung emission. Thermal effects can also often become important, particularly at high beam currents. Due to possible variations both in composition and geometry, as with substrate-precursor interactions, once deposition begins these processes can change substantially. This is most significant when depositing freestanding structures, as is considered in chapter 5.

Electron-precursor interactions

For EBID, the most important electron-precursor interactions are those leading to dissociation and hence deposition. The probability that an electron will break the bonds holding a precursor molecule together can be represented by an energy dependent cross-section. Unfortunately, these cross-sections are not trivial to determine. It is clear that there will be some dependency on the strength of the bonds to be broken, but this cross-section can also be strongly influenced by the environment of a molecule as well as the different reaction paths available. Furthermore, the molecules used in EBID are often rather exotic and hence unexplored to such extents. There

have been some attempts to calculate this parameter for some of the more popular precursors.[1] These studies found that the dissociation cross-section is largest at very low electron energies, typically below 1 keV. Although due to their significantly higher number, PEs undoubtedly play some role, there is a growing consensus that it is the low energy SEs which are primarily responsible for the dissociation of the precursor molecules in EBID.[1] The stochastic nature of these electron-induced precursor decomposition processes effectively makes 100% efficiency impossible. As a result, EBID materials can often contain a significant proportion of contaminate species. Low deposit purity is perhaps the most significant drawback of the EBID technique.

EBID is thus not so straightforward, a large number of different variables can influence the process. Many of these dependencies and issues can have a detrimental effect, a changing precursor concentration or electron scattering behaviour can ultimately affect both the quantity and quality of resulting deposits. A better understanding of these processes through further research investigations, such as detailed in this thesis, is essential.

The ionic analogue of EBID, ion beam induced deposition (IBID) is not detailed in this thesis. However, many of these principles still hold in the case of ions. There are two primary differences between EBID and IBID techniques. Firstly, due to their much larger mass, IBID tends to be more effective in dissociating the precursor, often yielding growth rates orders of magnitude higher than with EBID. At the same time though, the atomic ions used in IBID tend to become incorporated into deposits, leading to comparatively low purities. IBID of $Fe_2(CO)_9$ was attempted, and limited results are presented in appendix E. A thorough review of IBID (and EBID) can be found in reference 3.

1.2 Magnetic Deposits

This section details some fundamental magnetic principles, the understanding of which will aid the interpretation of results presented later in this thesis. Both static and dynamic magnetisation behaviour is discussed.

1.2.1 Magnetisation Behaviour

Ferromagnetism is caused by the interaction and subsequent alignment of neighbouring electronic moments via the exchange interaction. The details of this fundamental interaction will not be discussed any deeper than this here but it is this collective behaviour which gives rise to the macroscopic magnetic moment observed in ferromagnetic materials. This bulk magnetisation can be influenced by many different things, from temperature to external magnetic fields, but in their absence a key factor determining its orientation is magnetic anisotropy. There are multiple sources of magnetic anisotropy. One of particular importance is crystalline anisotropy, where a preferential magnetisation direction is induced by the atomic structure of a crystal lattice. Of most concern for this work however, is shape anisotropy, as is discussed below.

As illustrated in figure 1.2a, a magnetised body produces magnetic charges, or poles, at its surface. As a result, an internal magnetic field develops, opposing the magnetisation. This is known as the demagnetising field, $\vec{H}_d$. As illustrated in the figure, the strength of this field depends on the geometry over which it is produced. Longer dimensions produce smaller demagnetising fields. This geometrical dependence is defined in terms of the demagnetising factor $0 < N < 1$, which is inversely dependent (in a non-trivial way)[5] to the relative length of a dimension. In the limiting case of an infinitely thin film, $N = 0$ for the in-plane direction and

$N = 1$ for the out-of-plane direction. Subsequently, for a magnetisation $\vec{M}$

$$\vec{H}_d = -N\vec{M}. \tag{1.1}$$

In order to minimise this internal field and hence energy, magnetic bodies with an anisotropic geometry develop a preferential magnetisation direction coinciding with their longest dimension, a so called easy axis. As will be discussed, this preference influences the behaviour of the magnetisation when trying to manipulate it with an externally applied magnetic field.

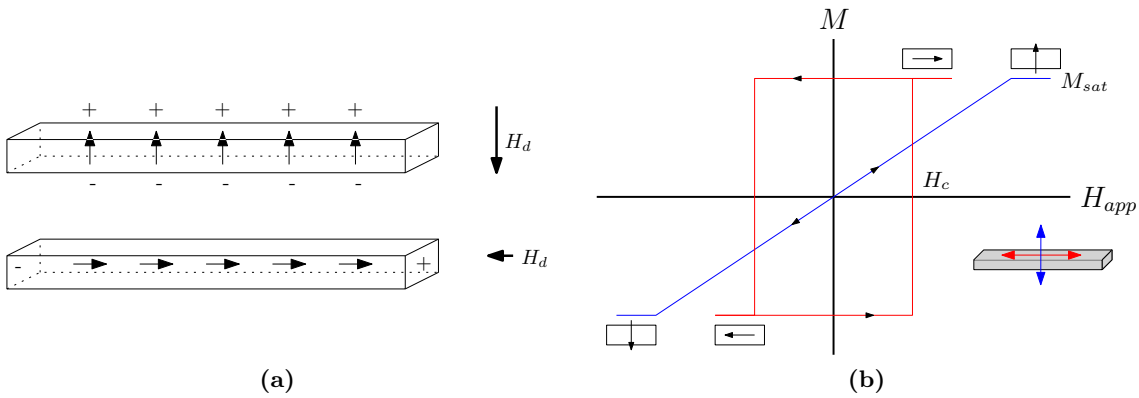

Figure 1.2: **(a)** A schematic illustration indicating how a magnetised object can give rise to demagnetising fields, which are responsible for shape anisotropy. **(b)** The influence of an external magnetic field on the magnetisation of a simple rectangular body. When a field is applied along the long, easy axis of the structure a hysteretic switching of the magnetisation is observed (red). When applied perpendicular to the easy axis, a more gradual saturation of the magnetisation results (blue).

Rotation of the magnetisation away from its easy axis is governed, in its ideal case (uniform, coherent magnetisation), by Stoner-Wohlfarth theory. This model considers the competition between an external magnetic field and this just described magnetic anisotropy. This competition is modelled by considering the minimisation of energy as

$$E = \frac{\mu_0}{2} N V M_{sat}^2 - \mu_0 M_{sat} V H \cos(\theta) \tag{1.2}$$

where H is the applied field, θ is the angle between the magnetisation and this field, M_{sat} is the saturation magnetisation, V is the volume of the object and μ_0 is the vacuum permeability. The first term in this equation describes the (shape) anisotropic energy and the second the Zeeman energy.

Applying this theory to a simple rectangular magnetic body, a trace of how the magnetisation behaves as a function of applied field is created, as shown in figure 1.2b. When a field is applied along the hard axis of the sample the opposing Zeeman and anisotropic energies yield a linear response and the magnetisation rotates very gradually. However, when a field is applied along the easy axis, saturation is achieved more easily and a switching type of behaviour results. Due to the significant preference for the magnetisation to remain along the easy axis, when an external field is applied to attempt to reverse the magnetisation, rather than gradually rotate through the hard axis the magnetisation flips at once at the so called coercive field H_c. This ultimately leads to a hysteretic behaviour, an important indicator of ferromagnetism.

Beyond the idealised case of a uniformly magnetised material, in reality, as a further consequence of energy minimisation, magnetic bodies tend to take on a multi-domained structure.

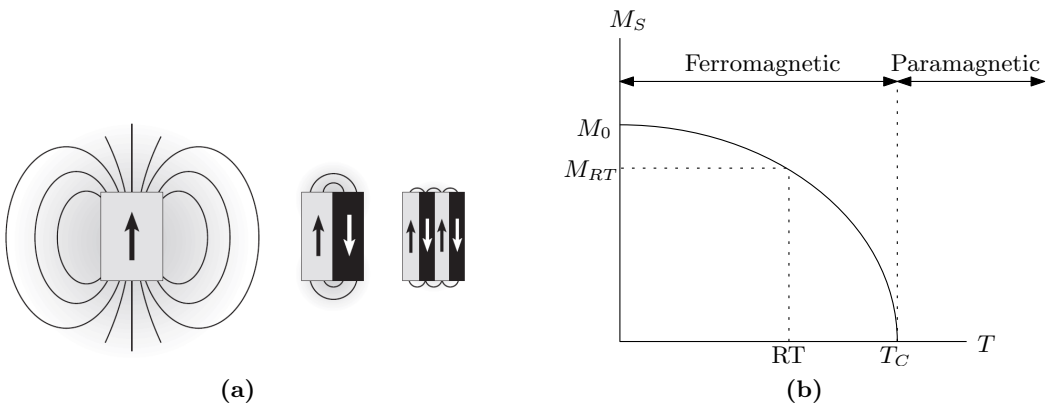

Figure 1.3: **(a)** The influence of domain formation on the external stray fields emitted by a magnetic body. Figure from reference 6. **(b)** The temperature dependence of the saturation magnetisation of a ferromagnet. Discussed in the text.

As illustrated in figure 1.3a, a single domain object produces a large, energetically unfavourable external stray field. Domain formation is the result of a compromise between the exchange interaction, which favours the alignment of adjacent magnetic moments, and the dipole interaction, which prefers anti-alignment. For the magnetisation reversal behaviour illustrated in figure 1.2b, domain formation can have two consequences. Firstly, the field required to switch the magnetisation (H_c) can be greatly reduced, since now some some fraction of all the domains already preferentially lie in that direction. Also, since individual domains need not be identical in size, each can have a slightly different anisotropy, and consequently, can switch at a slightly different field, leading to a rounding off previously sudden switching behaviour.

In addition to external fields, temperature can also have a significant influence on the magnetisation. Random thermal energy fluctuations constantly act to randomise the magnetic ordering of a ferromagnet. As illustrated in figure 1.3b, at room temperature (RT) this effect is generally small, leading to a small decrease in the magnetisation (M_{RT}). However, above the so called Curie temperature (T_C), this thermal energy becomes sufficient to completely destroy ferromagnetic ordering, causing materials to become paramagnetic.

One final magnetisation concept of relevance for this work, following on from a number of just described concepts, is that of superparamagnetism. As was mentioned, domain formation occurs on the basis of a balance between exchange and dipole interactions. With the former strong but short ranged and the latter weak but long ranged, in very small particles (<10 nm) a single domain state can often be energetically favourable. Given its volume dependence (see equation 1.2), it is possible for magnetic anisotropy (shape or otherwise) to be overcome in such particles, simply by random thermal fluctuations. Once this happens, each of these nanoparticles can essentially be viewed as a macrospin in a paramagnetic state, giving the bulk material containing the particles zero net magnetic moment. Given the common granular form of EBID deposits, superparamagnetism is a possibility when depositing ferromagnetic materials.

Many of these concepts will become important and be often referenced in later chapters.

1.2.2 Magnetotransport

The investigation of electrical transport through a substance can provide a lot of insight into both its physical and chemical structure and defines an important material characterisation

technique. For this reason, both electrical conduction in ferromagnetic material and selected important magnetoresistive effects will be discussed in this subsection.

Electrical Conduction in Ferromagnets

A schematic representation of the density of states (DOS) of a ferromagnetic material is shown in figure 1.4a. The valence band of (3d) ferromagnets consists of a superposition of an (energetically) narrow 3d band and a wide 4s band. Electron transport in these elements can be modelled reasonably well by Mott s-d scattering theory.[7,8] Here it is assumed that conduction is carried primarily by the more mobile s-electrons and that scattering events are spin conserving. These assumptions effectively divide the current into two spin dependent parts, as illustrated in figure 1.4b. Resistance is caused by transitions between s-states, either directly (ss, R_{ss}) or via a localised d-state (sds, R_{sds}), for both spin currents ($\uparrow, \downarrow$) independently. Above the Curie temperature or in non-magnetic transition metals these two resistance paths are equal. In ferromagnetic metals however, with more spin-down than spin-up d-states available at the Fermi level (E_F) (figure 1.4a), sds scattering and hence resistance is larger for spin-down electrons than it is for spin-up electrons ($R^{\downarrow}_{sds} > R^{\uparrow}_{sds}$). This increases the resistance of the entire spin-down channel, leading to a larger spin-up current governed primarily by ss scattering. In general, it is this large density of d-states and related scattering which causes the resistance in 3d-transition metals to be higher than that of ordinary sp-electron metals. Although conceptually useful, the idea of scattering that conserves electron spin is not always realistic. The spin-orbit interaction (SOI) is a process able to cause the spin of an electron to flip upon scattering, as is explained below.

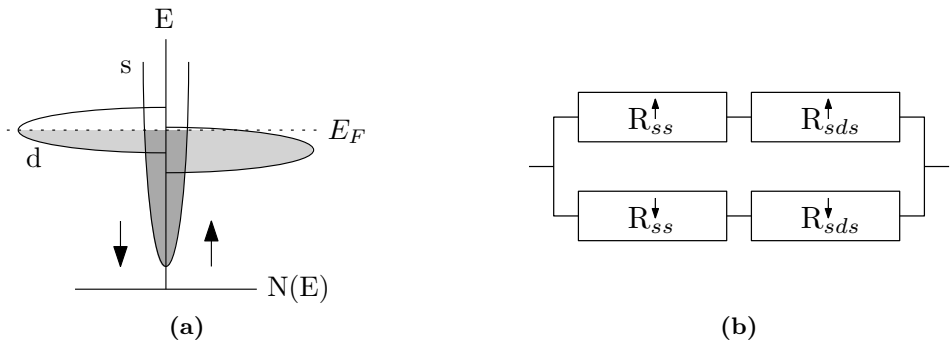

Figure 1.4: **(a)** A schematic representation of the density of states (DOS) of a ferromagnet. **(b)** The two spin current model describing conductance in a ferromagnetic metal. Discussed in the text.

In a stationary frame of reference and electron orbiting a nucleus experiences a static electric field. In the frame of the electron itself however, due to the now apparent orbital motion of the charged nucleus, this electric field varies in time thereby producing a magnetic field at the electron. It is the interaction between this orbital field and the spin magnetic moment of the electron which defines the SOI. This can effectively be seen as an internal Zeeman effect with the magnetic field now supplied by the orbital motion of the electron. The SOI is responsible for a number of important phenomenon, including hyperfine spectral splitting. By providing both the required magnetic torque and the means to conserve angular momentum[9] the SOI also enables mixing of the previously independent spin channels described above. As a direct consequence, the numerous spin-down d-states become accessible to the large spin-up current, leading to an increase in resistance. As will be discussed later, this process can be influenced by external magnetic fields, giving rise to magnetoresistive effects.

As was briefly mentioned earlier, EBID is not a particularly clean process. Deposits often contain a substantial degree of contaminates, usually non-metallic.[10] This commonly leads to non-metallic behaviour with conductivity increasing with temperature. In this work, a parameter is used to characterise such behaviour. The TCR or temperature coefficient of resistivity, describes how the resistance of a material varies with temperature and thereby gives an indication of the nature of the mechanism(s) of conduction. It is defined as

$$TCR = \frac{R(T) - R_{298}}{R_{298}(T - 298)} \tag{1.3}$$

where R_{298} defines the resistivity at room temperature (298 K) and T is typically taken at liquid helium temperature, 4.2 K. Due to the nature of the materials investigated in this work, it has been useful to express this parameter in the units parts-per-million-per-kelvin, ppm/K (equation 1.3 times one million). Qualitatively, this parameter is really only meaningful for materials showing a linear temperature dependent behaviour, i.e. metals. Qualitatively though, it can also be used to at least given an impression of the nature of the conduction taking place in other materials. Metals typically have a large positive TCR of several thousand of ppm/K while the TCR of semiconductors can vary from almost zero to very large negative values.

Further related to deposit impurities, a common microstructure encountered in EBID material is that of a granular metal, consisting of small metallic grains in an amorphous non-metallic matrix. Conduction in such materials has been well studied[11] and tends to take place via so called *variable range hopping* (VRH). Electrons move through the disordered insulating material between grains via unoccupied localised states. Such conduction is readily identifiable by temperature dependent behaviour of the form

$$\rho \propto \exp(T^{-x}) \tag{1.4}$$

where x is a constant, typically 0.5.[11]

A second characterising parameter, similar to the TCR used in this work is the residual resistivity ratio or RRR. Applicable only to metals, this is a measure of purity. Metallic resistivity generally has two contributions, that from defects and impurities and that from phonons. At low temperatures, phonon excitations are minimal leaving just the former, the intrinsic material resistivity. The magnitude of this intrinsic resistivity, and hence the purity of the metal can be characterised by the RRR, defined as[12]

$$\text{RRR} = \rho(298\text{ K})/\rho_0(4.2\text{ K}). \tag{1.5}$$

The value of the RRR depends on the metal, but for very pure iron it can reach values in the thousands.

Magnetoresistance

Magnetoresistance (MR) describes the phenomenon by which the electrical resistivity of a material changes when it is subjected to an external magnetic field. Here, a few such phenomena pertinent to the work in this thesis are described.

The simplest magnetoresistive phenomenon is known as *ordinary magnetoresistance* (OMR) and is a result of the Lorentz force. In the presence of an external magnetic field, this force causes conduction electrons to follow spiral trajectories. This in turn, reduces the mean free

path (MFP) and ultimately leads to a small, isotropic increase in the resistance as a function of applied field. OMR arises in all metals.

As discussed previously, electrical conduction in ferromagnetic materials can be described in terms of two spin polarised current channels. Due to the large asymmetry in the d-state electron DOS (figure 1.4a), the resistance of one spin channel tends to be lower, leading to a spin polarised current. By increasing the DOS asymmetry, an external magnetic field can induce a negative MR in a ferromagnetic material (shown in figure 1.5b, superimposed on AMR). This describes *normal magnetoresistance*. A similar reduction in resistance is also observed with temperature via an equivalent thermal influence on the spin order.

Another MR effect of particular relevance for this work is *anisotropic magnetoresistance* or AMR. Occurring in ferromagnetic materials, as the name suggests, it is a directional dependent phenomenon. The anisotropy is related to the angle between the probing current and the magnetisation (ϕ). When parallel, resistance is high and when perpendicular it is low. The basic cause of this effect has already been introduced previously and relates to a spin mixing induced by the SOI. A magnetoresistive effect arises due to the fact that this SOI can be regulated by an external field. The details of this process[8] will not be presented here but essentially, the probability for the spin of an electron to flip during a scattering event depends on the relative alignment of the electrons (and hence magnetisation) and the scattering centre. In the ideal case of coherent rotation of the magnetisation, this effect can be described by

$$\rho(\phi) \propto \cos^2(\phi). \tag{1.6}$$

There is in fact a very simple heuristic way to envision AMR, as is depicted in figure 1.5a. The anisotropy of the scattering can be thought to be a result of the changing orientation of the electron cloud surrounding each nucleus as the magnetisation is rotated.

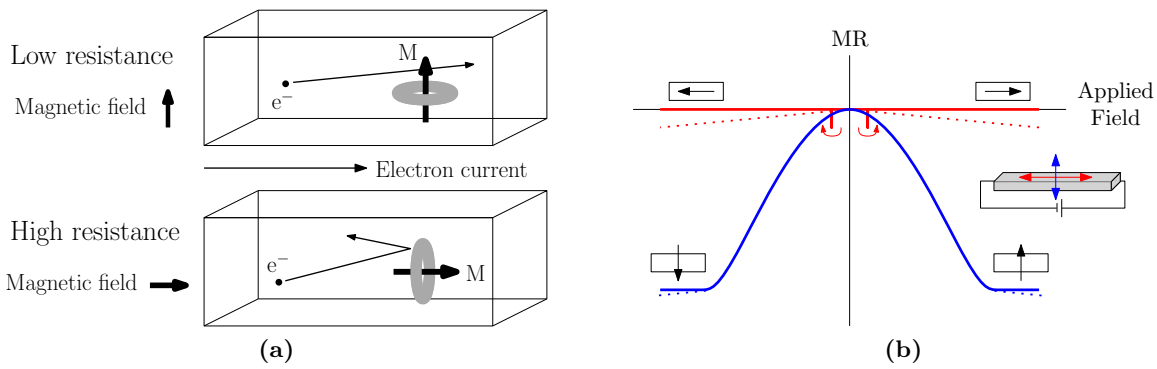

Figure 1.5: **(a)** An intuitive and semi-classical way to understand AMR. **(b)** The AMR behaviour expected from a simple rectangular magnetic body for fields applied along the easy axis (red) and a hard axis (blue). The superimposed influence of normal magnetoresistance is also indicated with a dotted line.

From equation 1.6 and previous discussion in this chapter, it is possible to qualitatively determine the appearance of AMR. This is shown in figure 1.5b for the case of a simple rectangular magnetic body, where the resistance is measured along its easy axis. When a field is applied along the easy axis of the structure, little AMR is observed since the magnetisation already lies in this direction. As the field is swept through zero however, brief increases in the resistance might be detected as the magnetisation switches. In contrast, fields applied perpendicular to the easy axis will rotate the magnetisation away from alignment with the current and the resistance will decrease, following equation 1.6. As previously discussed, beyond the ideal case of coherent rotation of the magnetisation, these results can again be expected to deviate slightly.

For an applied field H, the magnitude of the AMR is defined as:

$$\mathrm{AMR}(\%) = \frac{\rho(H) - \rho(H=0)}{\rho(H=0)} \times 100. \tag{1.7}$$

A more thorough treatment of the theory of AMR can be found in references 7,8,13,14.

There are many additional MR phenomena, which will not be describe here. One addition effect relevant to this work, grain-boundary magnetoresistance (GBMR), is considered as it arises, in chapter 4.

1.2.3 Iron Oxides

Here, a brief overview of the properties of some iron oxides is presented. When attempting to deposit iron from $Fe_2(CO)_9$ via EBID, the incorporation of some oxygen is generally unavoidable, due not only to its presence in both the vacuum but also in the ligands of the precursor itself. Oxides are of particular interest in the work discussed in chapter 4, where the influence of water vapour on the deposition process is investigated.

There are three main species of iron oxide, FeO, Fe_2O_3 and Fe_3O_4. With significantly lower enthalpies of formation, only the latter two are of interest here. Fe_2O_3 can be further divided into a number of phases, but only the alpha and gamma phases will be discussed.

Of all the oxides of iron, Fe_3O_4 is the most energetically favourable. It is readily found in nature as magnetite, being the most magnetic of all naturally occurring minerals. It is structurally rather unusual in that the Fe^{2+} and Fe^{3+} ions making it up exist in a charged ordered state (see figure 1.6). This charge ordering is responsible for a number of distinct properties, including its ferrimagnetic character (T_C=858 K). Electron transport between these ions gives Fe_3O_4 a rather low resistivity for an oxide, being of the order of 10^3 µΩ·cm.[15] Not completely understood, but also expected to be a result of this ionic structure is the Verwey transition. Occurring at a temperature of around 120 K, at this critical point the structure as well as the electrical and magnetic properties of the material change. Perhaps the most interesting property of this oxide (in terms of its use) is that it is 100 % spin polarised, or half-metallic.

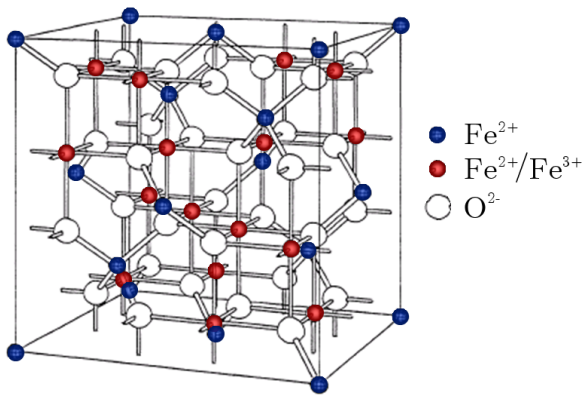

Figure 1.6: The cubic inverse spinel crystal structure of magnetite. As indicated, blue atoms are tetrahedrally coordinated Fe^{2+}; red atoms are octahedrally coordinated, 50/50 Fe^{2+}/Fe^{3+}; white atoms are oxygen.

α-Fe_2O_3 is the most common form of the Fe_2O_3 oxide. It, too, is commonly found in nature as the mineral hematite. As with Fe_3O_4, this oxide is magnetically quite complex. It is technically

an antiferromagnet ($T_{Néel}$=948 K), but above 260 K, due to a spin-orbit induced canting of certain moments, it gains a very small magnetic moment. γ-Fe_2O_3 has a very similar structure to Fe_3O_4 (cubic inverse spinel) and is consequently also ferrimagnetic. It forms naturally as the mineral maghemite. Both phases of Fe_2O_3 are electric insulators, with typical resistivities of the order of 10^7 µΩ·cm.[16,17]

In the next section, before ultimately detailing the work presented in this thesis, the state of the art of EBID of magnetic material is reviewed.

1.3 This and Previous Work

First in this section, a general review of selected notable and relevant works in the field of EBID of magnetic materials or 'magnetic EBID' is presented. Then, after first summarising the work of two predecessors, the motivations, goals and further details of the work of this thesis are presented.

Although providing some background on the subject, these reviews are not essential to the understanding of the results presented in this report.

1.3.1 A Short Review of Magnetic EBID

Nearly all EBID precursors originate from the world of chemical vapour deposition (CVD) and this is reflected in their popularity in EBID. For iron this means $Fe(CO)_5$ and cobalt $Co_2(CO)_8$. Nickel has been less popular, possibly due to the extreme toxicity of the popular CVD precursor $Ni(CO)_4$.[18]

Although the deposition of magnetic metals with EBID was successfully achieved in the 1980s,[19,20] investigations into the ferromagnetic character of such material were not attempted until the beginning of this century. In 2002, Lau et al.[21] performed what was effectively the first in depth magnetic study of magnetic materials produced by EBID (cobalt via $Co_2(CO)_8$). A metallic purity of 50 at.% and corresponding resistivity 25 times that of pure Co was achieved. The magnetic nature of the deposits was tested indirectly via the production and successful application of EBID MFM tips (magnetic force microscopy, see subsection 2.2.2). Deposits were also successfully used to seed carbon nanotube growth.

More recently, two groups have been particularly active in cobalt deposition (again $Co_2(CO)_8$). In Zaragoza, deposits with very high purities have been achieved, containing as much as 95 at.% Co and displaying metallic conduction properties.[22] Spintronic applications of this very pure magnetic material were also explored in the form of domain wall motion experiments.[23] A second group, from EMPA in Switzerland, have carried out a number of fundamental investigations. The influence of beam current on the composition and structure of deposited tips was thoroughly investigated with near 100 % pure cobalt deposited at high currents. Thermal effects arising at high currents were suggested to be at least partially responsible for the very efficient precursor dissociation.[24] Beyond metallic Co, applications of granular superparamagnetic cobalt material was also investigated in the form of hall-effect sensors.[25]

The EBID of iron ($Fe(CO)_5$) has been extensively investigated by a Japanese group. Numerous investigations into the production and (magnetic) characterisation (via electron holography)[26] of iron nanostructures have been published. From amorphous structures, typically 70 at.% pure, crystalline α-Fe was achieved via annealing.[27] Applications of such structures were also considered, including an iron 'nanomagnet' deposited on the end of a piezo-driven tip.[28] As will be further discussed in chapter 4, the influence of water vapour on deposits and the formation of Fe_3O_4 were also investigated.[29–31] By mixing two molecularly different iron precursors ($Fe(CO)_5$ and $Fe(C_5H_5)_2$) in different proportions, it was found to be possible to control the iron-carbon ratio in deposits (30 to 70 at.% Fe) and thereby tune the magnetisation.

By depositing in ultra high vacuum (UHV) conditions, high purity iron depositions (95 at.% Fe using $Fe(CO)_5$) have also been achieved.[32] A particular interesting and relevant experiment (see chapter 5) involving EBID Fe is that performed by Müller et al.[33] in 2008. Via a magnetic coupling, an array of iron nanopillars was found to be able to influence the resistance of an

underlying permalloy strip. Such an experiment gives a good indication of the potential of magnetic EBID for spintronic applications.

Although many interesting works on the subject of magnetic EBID have been published, the most relevant, is that of the two predecessors of this project. This is discussed in the next section.

1.3.2 A New Iron Precursor: A Collaboration with FEI

The M.Sc. work described in this thesis as well as that of two previous students (see below) was all made possible by the ongoing cooperation between the group FNA, physics of nanostructures, at the TU/e, and FEI Company, a developer of electron microscopy tools. FEI had been trying to develop precursors capable of yielding ferromagnetic deposits, and after FNA gained access to a FEI Nova 600i Nanolab electron microscope (the *dualbeam*, described in the following chapter), a collaborative opportunity naturally presented itself.

A similar such partnership had been developed by FEI with the University of Zaragoza in Spain, specifically to investigate precursors containing cobalt. Consequently, and due to its higher magnetic moment, the decision was made to focus on iron based precursors at FNA. As is apparent from the literature reviewed above, $Fe(CO)_5$ is the most popular iron precursor used for magnetic EBID. For this collaboration however, it was decided to investigate some of the lesser known iron compounds.

M. Beljaars: Electron Beam Induced Deposition of Iron (2008)[4]

Michael Beljaars[4], the first M.Sc. student involved in the FEI-FNA collaboration, investigated two iron precursors almost unmentioned in literature, $Fe_2(CO)_9$ and $Fe_3(CO)_{12}$.

The precursors were characterised both in terms of the yield and composition of resulting deposits as a function of the energy and current of the electron beam. The $Fe_3(CO)_{12}$ precursor was found to be unresponsive to changing beam properties and maintained a low yield and iron compositions no higher than 50 at.%. The $Fe_2(CO)_9$ precursor in contrast, with a higher average yield, responded positively to increasing beam current (as often observed in literature),[10] with iron content increasing from 25 at.% to 60 at.%. Preliminary magnetic characterisation of deposits made with both precursors revealed signs of magnetic behaviour (see figure 1.7).

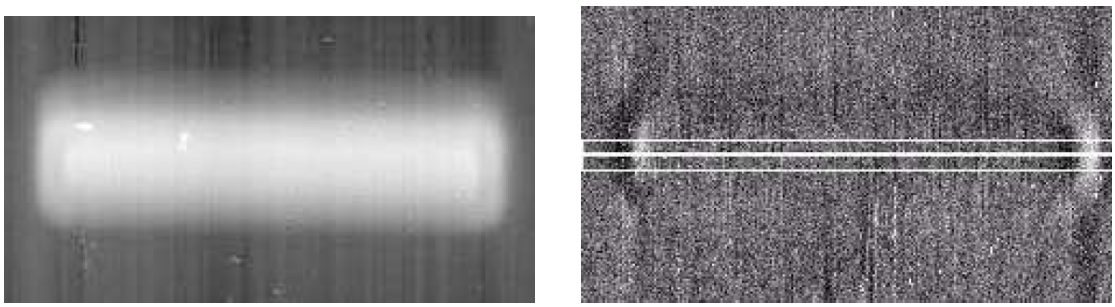

(a) **(b)**

Figure 1.7: **(a)** Atomic and **(b)** Magnetic Force Microscopy (MFM) images of an EBID microwire deposit (5 x 1 µm) produced from $Fe_3(CO)_{12}$ in a longitudinal applied field (340 mT). Peaks in the MFM signal at either end of the deposit indicated the presence of magnetic stray fields. Figures from Beljaars[4]. 300 mT

Beyond characterisation, a significant portion of this work was also dedicated to the investigation of the surface processes of EBID, particularly the influence of precursor adsorption, diffusion

and desorption on the shape of deposits. The stimulus for this work was the appearance of unusual edge features on deposits made using the $Fe_3(CO)_{12}$ precursor, which was shipped in a volatile methanol solution. The influence of factors such as substrate temperature, waiting time between deposition passes, and the presence of volatile species such as methanol, on the form of deposits were studied and explained. A physical model and accompanying computer simulation were developed that could successfully, though qualitatively, explain many of the unusual deposit features.

Additionally, a small part of this work covered the investigation and calibration of the EDX system of the dualbeam. By comparing quantification results with that from well known test samples, eventually a measurement uncertainty of just a few percent was achieved.

F.J. Schoenaker: Exploring the fabrication of ferromagnetic nanostructures by Electron Beam Induced Deposition (2010)[34]

Following on from the work of Beljaars, the second M.Sc. work of this collaboration, that of Frank Schoenaker, focused on further characterising the seemingly more promising $Fe_2(CO)_9$ precursor. The goals of this research were twofold: to optimise the deposition strategy and to further investigate the ferromagnetic properties of the EBID iron. As already mentioned, the university of Zaragoza was involved with FEI in similar projects but with cobalt based precursors. For the work of Schoenaker, this connection was utilised in the form of a cooperation with the research group Departamento de Física de la Materia Condensada. Although deposits were produced in Eindhoven, a number of measurements, particularly those requiring high magnetic fields (up to 9 T), were carried out in Zaragoza.

Both high electron beam currents and low energies were found to be essential to produce high purity deposits. High currents were explained to be responsible for enhanced precursor dissociation and possibly local heating. The influence of electron energy was explained in terms of penetration depth; a low energy electron deposits its energy nearer the surface, where deposition takes place. Vacuum conditions, particularly partial water pressure, were also found to play a key role in deposit purity, as illustrated in figure 1.8a. Ultimately, using very high currents (20 nA), low energies (2 keV) and optimal vacuum conditions, deposits containing as much as 78 at.% iron were reliably produced.

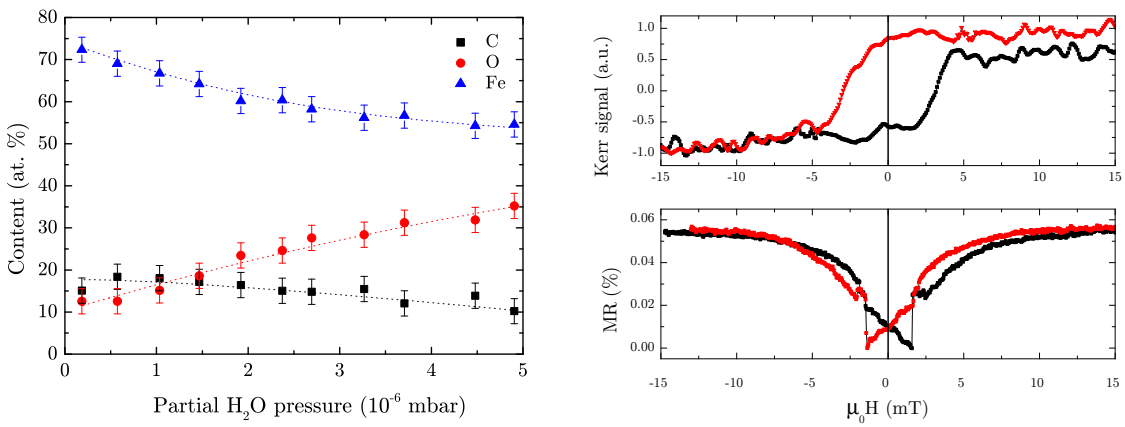

(a) (b)

Figure 1.8: **(a)** The influence of the partial water pressure of the dualbeam vacuum on the composition of EBID iron deposits. **(b)** MOKE and AMR measurements from an EBID iron microwire deposit. The observed hysteretic switching is indicative of ferromagnetism. Black indicates increasing, red decreasing fields respectively. Figures from Schoenaker[34].

The influence of substrate temperature on depositions was also briefly studied; no definitive influence was found, although results were not conclusive. Further temperature investigations were performed involving the temperature of the precursor itself. Heating it to 45 °C instead of the usual 28 °C lead to higher flux, but at the expense of the lifetime of the precursor.

Wire deposits, approximately 12 µm long, were fabricated on electrical contacts for electrical and magnetic characterisation. Utilising optical (MOKE) and electrical (AMR, Hall Effect) techniques (discussed in the next chapter), characteristic ferromagnetic phenomena: hysteresis, magnetoresistance and anomalous Hall effects, were observed in all deposits studied (containing between 61 and 73 at.% Fe). An example measurement is reproduced in figure 1.8b. From the rounded appearance of the hysteresis loops and sudden resistance jumps during magnetoresistance measurements, the deposits were predicted to consist of many magnetic domains. Hall effect measurements suggested that saturation magnetisation was approximately proportional to iron content.

The resistance of deposits was low, 10-100 times that of pure iron, but consistently increased with decreasing temperature, indicating semiconducting behaviour. The almost flat temperature response of the most iron-rich deposits was taken to suggest that they existed in a metal-insulator transition (MIT) regime. Temperature dependent AMR measurements showed an increased magnetoresistance with decreasing temperature.

The work presented in this thesis is a continuation of the FNA-FEI collaboration and as such, maintains its general goals. In the next section however, some more specific aims and goals of this work are outlined.

1.3.3 This Work

The M.Sc. project described in this thesis was undertaken with two primary goals in mind. Firstly, to continue and expand the characterisation work performed by Schoenaker[34] using the $Fe_2(CO)_9$ precursor and secondly, to begin investigating deposits suitable for preliminary magnetic applications. The positioning of this work in work relative to previous studies is illustrate in figure 1.9.

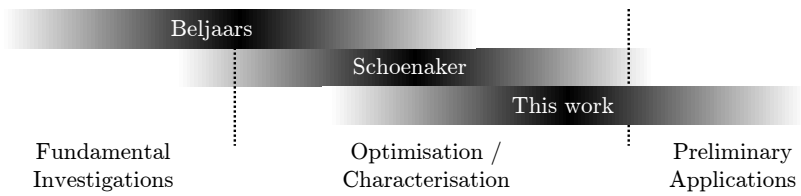

Figure 1.9: The state of the FEI-FNA collaboration. The work of this thesis focuses further on characterisation as well as some initial applications of the magnetic deposits.

Given the two separate goals, results have been divided up accordingly. Chapters 3 and 4 describe the characterisation of simple micron-sized wires. Microstructural, electric as well as all important magnetic characterisation has been carried out. First, in chapter 3, overlapping somewhat with the work of Schoenaker[34], deposits produced under optimal conditions and hence containing approximately 75 at.% iron are investigated. In the following chapter however, by modifying the vacuum conditions via the injection of water vapour, deposits with iron-oxygen contents down to 1:1 (∼50 at.% Fe) have been produced and investigated. Combined, the two chapters describe the systematic investigation of the influence of oxygen content on deposit properties. As mentioned earlier in this chapter, EBID of iron in the presence of excess water

vapour has been explored before. With oxygen representing a primary vacuum as well as deposit contaminate, a better understanding of its influence is of fundamental importance. The combination of iron and water is also of interest on its own, especially for spintronic applications given the 100 % spin-polarised nature of Fe_3O_4.

The connection with the university of Zaragoza begun with the work of Schoenaker [34] was continued for this project. Although all deposited locally, a number of these microwire depositions were investigated in Zaragoza.

In the second half of this thesis, chapter 3, freestanding iron nanopillar deposits have been investigated. With an eye on eventual applications, if magnetic, such geometries can be expected to produce stray fields and thereby be able to influence other nearby magnetic materials. To be able to produce nanostructures with such capabilities, particularly with all the ease and versatility granted by the EBID technique, is a particulary promising prospect. Before reaching the point of application however, such deposits must be better understood. While direct electrical and magnetic characterisation of such pillar deposits is not trivial, both the form and composition have been investigated as a function of changing electron beam properties. With the help of computer simulations, an investigation into the influence of beam induced heating at high electron currents has also been performed. This chapter ultimately leads up to the results of a pilot experiment where the influence of iron nanopillars on domain wall motion in perpendicularly magnetised wires has been investigated.

Before these results are presented, the next chapter details some relevant experimental techniques and equipment, including the FEI *dualbeam*.

Chapter 2

Experimental Equipment & Techniques

In this chapter a number of important experimental apparatus and the techniques by which they are utilised are discussed. Both deposit production and characterisation is covered. Due to its importance in this work, the dualbeam and all its numerous capabilities, both depositional and analytical, are first discussed. Then in the second half of this chapter the details of some additional characterisation tools are presented.

2.1 The Dualbeam

The key device used in this work is the FEI *Nova 600i Nanolab*. With both scanning electron microscope (SEM) and focused ion beam (FIB) facilities, it is commonly known as a *dualbeam*. A schematic representation and interior photo of the device are shown in figure 2.1.

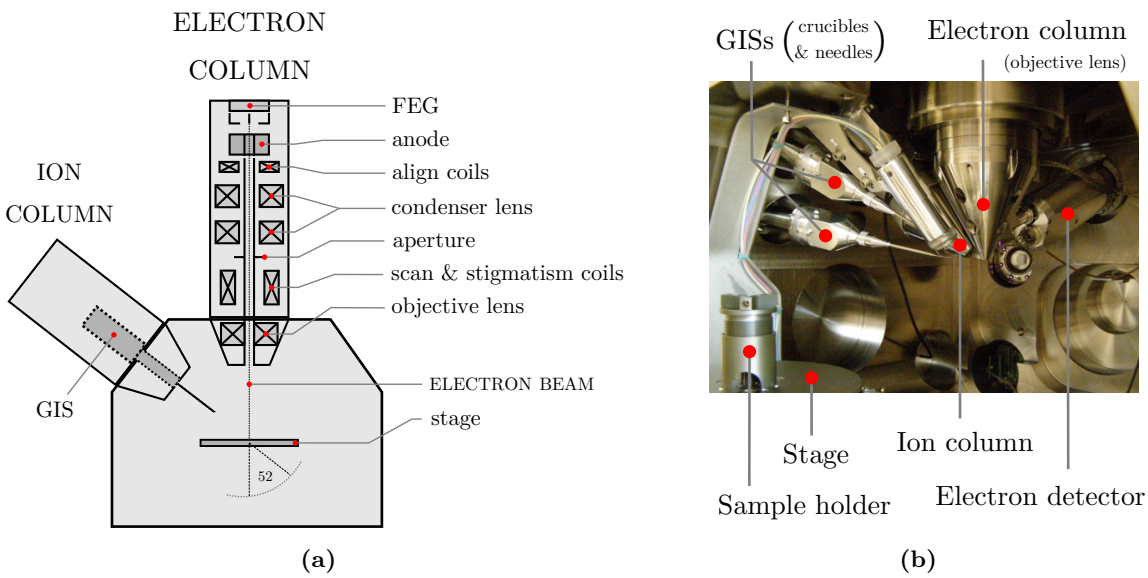

Figure 2.1: **(a)** A schematic illustration of the dualbeam showing the electron and ion beam columns, the sample stage and (behind and in front of the ion column), the GISs. The details of the electron column are discussed in the text. **(b)** An internal view of the dualbeam, inside the vacuum chamber.

The ion beam is orientated at a 52° angle with respect to the vertical electron beam. This allows simultaneous and coincidental operation of both. Samples are mounted on a motorised 5-axes stage, able to undergo full rotation and tilt over 52° relative to the electron beam. The dualbeam is a high vacuum (HV) device, capable of pressures of the order of 10^{-5} to 10^{-6} mbar. The vacuum pressure can be roughly measured by an internal cold-cathode (Penning) gauge and more specifically characterised by an RGA (residual gas analyzer) which is also attached.

As detailed in figure 2.1a, the electron column is based upon a field emission gun (FEG) electron source. After extraction and acceleration by the anode, the beam is aligned and columnated by a number of electromagnetic lenses and apertures. The scanning of the electron beam and further astigmatic corrections are achieved with an additional lens before the electrons are focused onto the sample by a final objective lens. As will be discussed later, this final lens can be operated in a number of modes depending on the required application. Due to its limited use and relevancy, the FIB, based on a liquid metal ion (LMI) source of Gallium, will not be further detailed here.

The SEM of the dualbeam is capable of acceleration voltages of a few hundred volts to 30 kV. Similarly, electron currents from pA to ∼20 nA are possible. With the sample stage connected to a nanoampmeter, specimen currents can be measured *in situ*, even during deposition.

2.1.1 Detectors & Imaging

A primary function of the dualbeam is SEM. Operating in much the same way as an optical microscope but with electrons replacing light as the probing medium, electron microscopy allows very high magnifications (as high as x 1.5 million in the dualbeam) to be achieved due to the very short (de Broglie) wavelength of the particles. As discussed in the previous chapter, when a focused beam of electrons is incident on a solid surface, a number of scattering processes can take place. To produce an image with SEM, the electron beam is scanned over a sample and the electrons produced in these scattering processes are detected to form an image. Both SEs and BSEs can be used for image formation. Low energy superficial SEs can be used to form an image of the surface. While higher energy BSEs can give an image both atomic-number (Z) and depth contrast.

The dual beam has a number of different detectors, including those for SEs and BSEs. As will be discussed below, an internal *through-the-lens* detector is also available for high-resolution imaging.

Imaging Modes

As was mentioned, the objective lens of the dualbeam can be operated in a number of different modes. Three different lens settings are available corresponding to three different imaging modes: regular high-resolution mode (HR), ultra-high resolution mode (UHR) and Energy Dispersive X-ray (EDX) mode. The differences in the objective lens in these modes are indicated in figure 2.2, which shows a schematic cross section. Made of a soft ferromagnetic material, the lens contains two electromagnetic coils which can switched on and off independently. In HR mode (figure 2.2a) the inner coil is used to create an internal magnetic field and consequently, an internal lensing action (shown in green) with a rather long focal length. In this mode, the regular external electron detector is used, as indicated in the figure. In UHR or immersion mode (figure 2.2b) the larger outer coil is used, producing a magnetic field which now extends axially into the vacuum chamber, immersing the specimen being imaged, as indicated in the figure. In addition to a much shorter focal length and thus reduced optical abberations, the external field

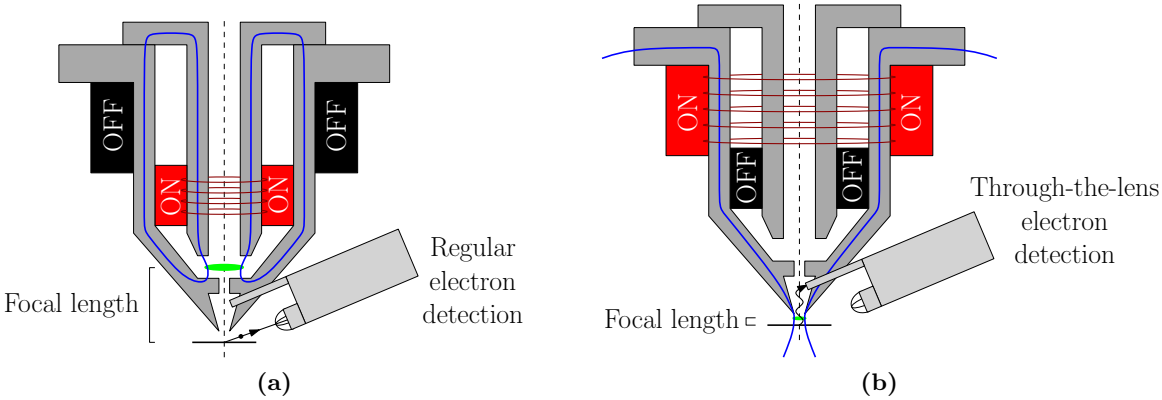

Figure 2.2: The **(a)** regular (high-resolution, HR) and **(b)** immersion (ultra-high resolution, UHR) lens modes of the dualbeam SEM. Each mode utilises a different set of electromagnetic coils for lensing. Current through the different coils and resulting magnetic flux paths are conceptually indicated as the dark red rings and blue lines respectively. The focusing action of each mode is indicated in green. In addition to a different lens mode, for UHR (b), electrons are detected internally via a through-the-lens (TTL) detector. The lens and electron detector can also be seen in figure 2.1b.

produced in this mode is also very effective at capturing electrons and directing them upwards to an internal, through-the-lens (TTL) electron detector. Combined, the immersion lens and TTL detector allow significantly higher resolutions to be achieved. EDX mode is similar to the immersion mode, just with a lower field strength and is optimised for EDX analysis (see below).

Energy Dispersive X-ray Detector

In addition to electron detectors, the dualbeam also has the capability to detect X-rays emitted from a sample. Analysis of these characteristic X-rays can then be performed to determine the composition of the sample.

Energy Dispersive X-ray (EDX) spectroscopy is an analytical technique which can be used to investigate the elemental composition of a material. The technique involves bombarding a sample with charged particles and analysing the X-rays emitted as a result. Since each element possess a unique atomic structure, and hence characteristic X-ray emission spectrum, by analysing the frequency and relative intensities of the emitted radiation, the atomic composition of the material can be determined.

The dualbeam is equipped with an LN_2 cooled EDAX X-ray detection system, allowing for *in situ* compositional characterisation. The electron beam is used to induce X-ray emission. As mentioned above, a special lens mode is used, optimised for X-ray analysis. Following Schoenaker[34] and Beljaars[4], 2 keV electrons were used for all EDX measurements. The shallow penetration depth of such electrons is most ideal for the investigation of surface deposits and not the substrate. 2 kV represents the lowest electron energy still able to reliably excite primary X-ray emissions from the three important atomic species of the iron deposits: iron (Lα: 705 eV), oxygen and carbon (Kα: 525 & 277 eV, respectively).[35]

Utilising the calibrations of Beljaars[4], all EDX measurements in this work are taken to have an uncertainty of approximately 3 at.% (atomic percent).

2.1.2 Depositing

In addition to imaging, the dualbeam is also intended to be used for deposition, and is equipped accordingly. This section reviews the important aspects of performing EBID with the dualbeam, including the gas injection system and patterning strategies.

Gas Injection System

For the purpose of EBID, a gaseous precursor must be introduced to a substrate. In the dualbeam, this is achieved with a gas-injection-system or GIS. Mounted either side of the ion column (see figure 2.1a) with components both inside and outside the vacuum chamber, a GIS consists of a thin needle (ø 600 µm) attached to a small crucible (visible in figure 2.1b) which is in turn mounted to a pneumatic injection system. With precursors either liquid or solid under standard conditions, heat must be applied to vaporise them. The $Fe_2(CO)_9$ precursor was heated to 27 °C and when injected, was positioned approximately 150 µm from the deposition location, both laterally and vertically.

In addition to $Fe_2(CO)_9$ for iron deposition, the dualbeam at FNA is equipped with four additional GISs containing precursors suitable for the deposition of platinum, tungsten, carbon and silicon oxide.

Patterning

When designing a structure to be deposited with EBID, in addition to its shape, there are a number of important patterning parameters which must be considered. These mostly relate to how each individual point making up the design is addressed. For a given beam diameter, the *overlap* determines the resolution of a design by defining how much two adjacent points should overlap. Similarly, the *dwell time* determines the length of time the beam spends at each individual point. Finally, and more globally, is the number of *passes*, which, by defining how many times a pattern will be overwritten, determines the total deposition time. Each pass can be carried out either line-by-line in a raster fashion or in one continuous run (serpentine). Between passes, or when the beam must pass a region not meant to be patterned, it is blanked (deflected from the substrate with a magnetic field).

Small changes in these parameters can have a substantial effect on resulting depositions. For a specific electron beam current and precursor flux the dwell time will determine how efficiently the deposition process occurs. If too long, then the irradiated region may run out of precursor, if too short then decomposition may not be complete. These two possibilities define the precursor and electron limited regimes, respectively.

Although the dualbeam software is capable of producing and implementing patterns itself, greater control is granted by so-called stream files, text files in which a pattern is precisely defined numerically. The wire deposits discussed in the following two chapters were patterned using such files. As is further discussed in chapter 5, it is also possible to deposit using *spot-mode*, where the electron beam is focused at a single spot for an extended period, leading to the deposition of freestanding structures.

2.2 Additional Characterisation Tools

Beyond the dualbeam, some additional characterisation tools were also utilised for this project. Here, an overview of these is presented.

2.2.1 Transmission Electron Microscopy & Electron Diffraction

Beyond surface-sensitive electron microscopy techniques such as SEM, for thin samples there also exists the possibly to form an image from the electrons being transmitted. Transmission electron microscopy or TEM involves precisely this. High energy electrons (10s-100s keV) are focused onto a very thin sample (10s nm) and detected on the other side. Due to the high energies involved, sub-nanometre resolution is readily achievable.

The two primary imaging modes of TEM are bright-field (BF) and dark-field (DF). In BF-TEM, the bright undiffracted central spot of the electron beam emerging from the specimen is used to form an image. Contrast in a BF-TEM image comes from differing degrees of electron occlusion and absorption by the sample. In DF-TEM, apertures are used to limit electron detection to a region off axis with respect to the incident beam. Subsequently, only electrons which scatter (diffract) from the sample in a particular direction (towards the aperture) are used for imaging.

An additional characterisation technique possible with TEM is electron diffraction. Analogous to optical diffraction, by studying the diffraction pattern produced when a thin sample is illuminated with the electron beam, the crystallographic nature of the material can be determined.

Both TEM and electron diffraction are used in this report to investigate the microstructure of deposits. In the case of the microwire deposits, due to their size, they first had to be prepared to allow for such analysis. This entailed first coating the deposits with EBID and then IBID platinum for support, and then using a FIB to mill-out and thin cross-sectional lamellas. Although lamella preparation was performed in the dualbeam, actual TEM was performed externally in conjunction with Philips MiPlaza.

2.2.2 Atomic Force Microscopy

An atomic force microscope (AFM) is a scanning probe device capable of measuring surface features with nanometre resolution. Topology is determined by monitoring the forces (Coulomb, van der Waals, etc. or in the case of magnetic force microscopy, MFM, dipole-dipole) on a sharp tip as it is scanned across a surface. This tip is mounted at the end of a cantilever such that these forces can be quantified by monitoring cantilever deflection. Typically, this deflection is measured optically, by observing the motion of a laser spot reflected off the top of the cantilever. Using a feedback system, cantilever deflection is kept constant by adjusting the tip-surface distance. Not only does this prevent potentially damaging collisions between the tip and the surface, it also provides the required force-dependent height contrast necessary to form a topological map of a surface.

An AFM can operate in a number of different modes, the three most common of which are briefly described. The simplest and most straightforward is contact mode. Here the tip is effectively dragged across the surface, it is the repulsive coulomb force which provides topological contrast. In non-contact mode, the tip is scanned a small distance above the surface while the cantilever is oscillated near resonance. Attractive forces (such as van der Waals) influence the oscillation and by adjusting the tip-surface distance to compensate, topological contrast is obtained. Finally

there is semi-contact or tapping mode. This approach combines the best features of the previous two modes, being less destructive than full-contact mode but more sensitive than non-contact mode. Here, the cantilever and tip are again oscillated, however now the tip is made to contact the surface at the limit of the oscillation ('tap'). As with non-contact mode, surface forces influence this oscillation and by adjusting tip-sample separation to compensate, a picture of the surface can be constructed.

As discussed below, in this work, AFM was used for resistivity calculation. Semi-contact mode was used exclusively.

2.2.3 Electrical Methods

Electrical characterisation was carried out in a home-built multipurpose setup consisting of numerous source- and multi-meters, a cryostat system capable of temperatures from 4 to 400 K and an 800 mT magnet.

As is discussed at the beginning of the following chapter, for the purpose of electrical characterisation, wire deposits were produced on top of pre-patterned electrical contacts. As illustrated in figure 2.3, each wire is deposited on four contacts in a so called four-point probe layout. The outer two contacts are used to apply a current (source) and the inner two to measure the resulting voltage drop (sense). Due to the high input impedance of the voltage probes, minimal current flows and essentially, only the voltage drop caused by the deposit itself is measured, not that due to contact resistance or wiring. Both room temperature and temperature dependent resistance measurements have been performed in this way.

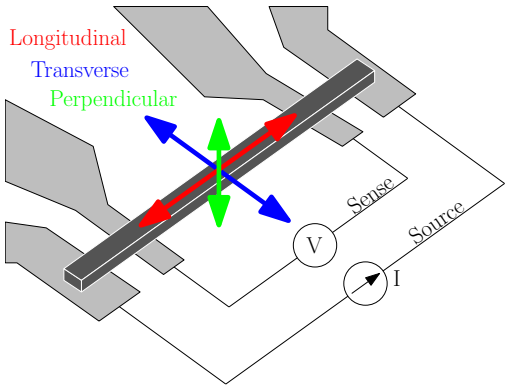

Figure 2.3: An illustration of the four-point probe resistance measuring technique. A wire (dark) is shown on four electrical contacts (light). The concept is described in the text. Also shown in this figure, indicated by the arrows, are the three principle directions along which fields are applied for MR measurements.

In addition to simple resistance measurements, magnetoresistance was also measured in this setup. The changing resistance behaviour was typically analysed for three different field directions. These are shown in figure 2.3. Using AFM to determine the cross-sectional area (A) and length (l) of deposits, measured DC resistances (R) were converted into resistivities using the equation: $\rho = RA/l$.

2.2.4 Kerr Microscopy

A final characterisation technique utilised for this project is Kerr Microscopy. When a beam of polarised light reflects off a magnetised surface, its polarisation can rotate slightly as a result

of the Magneto-optical Kerr effect (MOKE).[34,36]

For this work, MOKE measurements have been carried out using a wide-field Kerr microscope, essentially just a regular optical microscope modified to operate with polarised light. With light passing through a polariser both before and after illumination of the sample (cross-polarisation), magnetisation changes appear as variations in intensity. The microscope is connected to a camera and computer, allowing these changes to be recorded digitally. In order to improve magnetic contrast, both averaging and background subtraction are implemented. An example of a Kerr microscopy image is shown in figure 2.4.

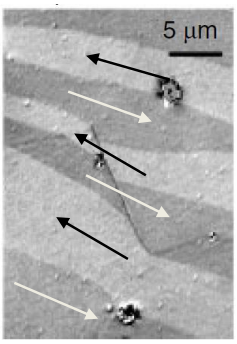

Figure 2.4: A typical image from a Kerr microscope, showing the contrasting (in-plane) magnetisation directions. Taken from reference 36.

The magnetic information depth of the Kerr effect is about 20 nm in metals,[36] making it primarily a surface sensitive effect. Even so, hysteresis loops can be obtained by monitoring the light intensity of a region of interest while sweeping an applied magnetic field. Although signal intensity is difficult to correlate to absolute magnetisation values, the shape of such loops as well as parameters like the coercive field are still meaningful.

The light source of the microscope is incandescent in nature, making the intensity of illumination and hence signal-to-noise ratio lower than that of more commonly used laser-based MOKE setups.[34] The use of optical light also limits lateral resolution to a few hundred nanometres. However, the speed and ease with which a measurement can be made is much greater.

Chapter 3

Exploring Iron Microwires

In this chapter, an investigation of the structural, electric and magnetic characteristics of EBID microwires containing a high percentage of iron (> 70 at.%) is presented. This is an extension of previous work carried out by Schoenaker[34]. In addition to its fundamental value, such an investigation also sets a baseline for the systematic characterisation work presented in the following chapter. The influence of deposit thickness has also been investigated, with thicker deposits found to exhibit some unusual characteristics.

Before results are presented, in the following section, some technical details about the microwire deposits and their production are discussed.

3.1 Deposit Fabrication

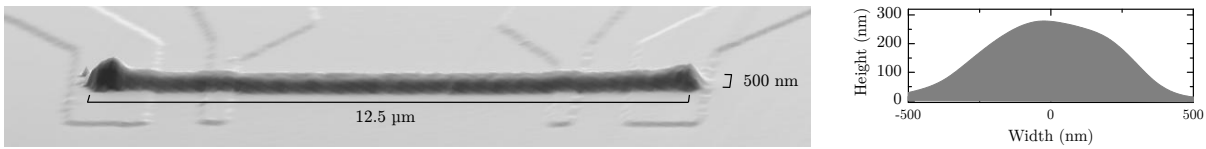

(a) **(b)**

Figure 3.1: **(a)** An AFM scan of a typical EBID iron wire deposition on four-point electrical contacts. The deformities at either end of the deposit are patterning errors where the beam changes direction. **(b)** A cross-sectional profile view of the same deposit.

For this study, deposits with simple rectangular, wire-like geometries were utilised. These wires were patterned with nominal dimensions of 12.5 µm x 500 nm (length x width). Due to its dependence on both the deposition time and precursor pressure, deposit thickness varies, though is typically of the order of a few hundred nanometres thick. As well as being easy to produce, such wire deposits are well suited to electrical measurements and furthermore, exhibit intrinsic shape anisotropy, useful for magnetic characterisation. Wider rectangle geometries were chosen over simpler lines to make eventual optical probing easier. An AFM scan of a typical microwire deposit is shown in figure 3.1.

Wires were deposited on silicon substrates. To enable electrical measurement, these substrates have a 100 nm surface layer of insulating silicon oxide (SiO_2) and are patterned with four-point electrical contacts, as shown in figure 3.2.

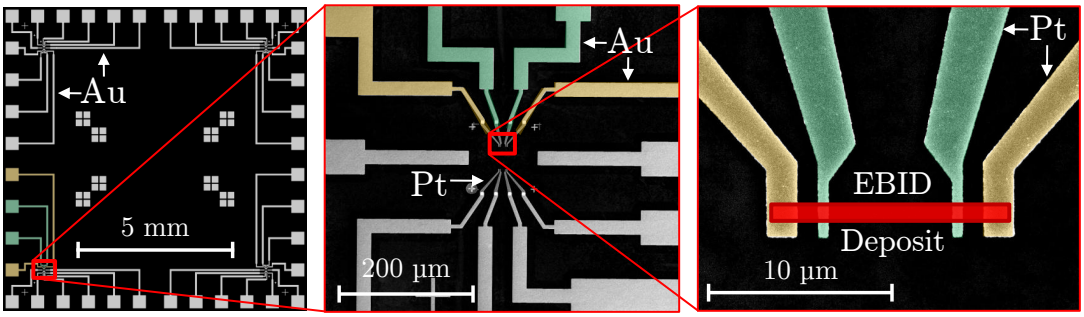

Figure 3.2: SEM images of the electrically patterned silicon substrates on which wire depositions were produced. Three different magnifications are shown. The four-point electrical contacts consisted primarily of sputtered Au (∼100 nm thick, UV lithography) with Pt (∼50 nm thick, Electron Beam Lithography, EBL) defining the finer details. The electrical pathways of one four-point contact are highlighted in yellow (source leads) and green (sense leads) with the position of the deposit shown in red. Each substrate could accommodate up to 8 wire deposits.

Drawing on the conclusions of the optimisation work of Schoenaker[34], by depositing under optimal vacuum conditions (allowing the system to pump for a minimum of 48 hours) and using an electron beam with a low energy (5 kV) and high current (∼ 20 nA) wires with an iron content of ∼ 75 at.% could be readily produced. 5 keV rather than slightly more effective 2 keV electrons were used in order to increase resolution slightly.

As mentioned in section 2.1.2, wires were patterned using a stream file. With beam diameter (FWHM) under the above conditions estimated to be around 200 nm, and given the use of 50% overlap, each point in the pattern was separated by 100 nm. Each wire consequently consisted of four rows of approximately 125 points. These points were addressed in a serpentine manner (along the four rows) with a dwell time of 1 µs. The number of passes depended on the patterning time but for a typical 15 minute deposit was of the order of 2 million.

As is further discussed in appendix A, deposits were found to be very stable. Over periods as long as months, oxidation was found to have a minimal influence.

3.2 Microstructure

Using both SEM and TEM analysis techniques, two notably different forms of microstructure were identified in the iron-rich microwires.

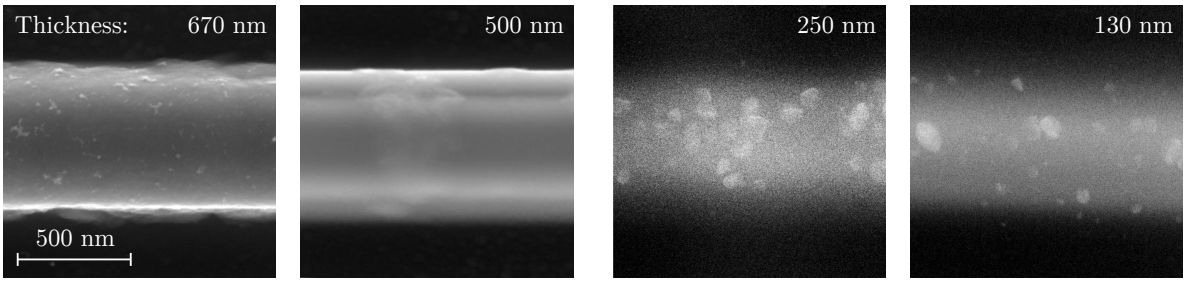

(a) **(b)** **(c)** **(d)**

Figure 3.3: High-magnification SEM micrographs (10 kV, ≤1 nA, immersion lens mode) of four EBID iron wires with similar compositions (∼75 at.% Fe) but different thicknesses, as indicated. All images are at equal magnification as indicated by the scale in (a).

Although primarily surface sensitive, a SEM is granted a degree of depth sensitivity by BSEs (see section 1.1). Consequently, initial microstructural investigations involved simple and non-invasive SEM imaging. It was revealed that dependent on thickness, deposits took on one of two different characteristic forms. Thick deposits (> 200 nm), as shown in Figures 3.3a and 3.3b, appeared opaque and generally quite homogeneous. Thinner deposits however, as seen in Figures 3.3c and 3.3d, as well as looking transparent, displayed cluster like features. The escape depth of BSEs produced by a 10 keV beam in an iron based composite material such can be as high as 200 nm (ref. 37). Imaging at this energy can thus be expected to yield a depth sensitivity of the same order of magnitude, explaining the opaque appearance of the thinner deposits. An explanation of the cluster features apparent in thinner deposits required more advance imaging techniques.

To better explore the microstructure of the wire deposits, including the apparent height dependency, a thick microwire was investigated with TEM. Figure 3.4a shows a dark-field TEM image of a lamella made from a 670 nm thick microwire (the same deposit as shown in figure 3.3a). As described in subsection 2.2.1, DF-TEM utilises scattered electrons for image formation such that similar (bright) contrast defines scattering from a crystalline material with uniform structure and orientation.

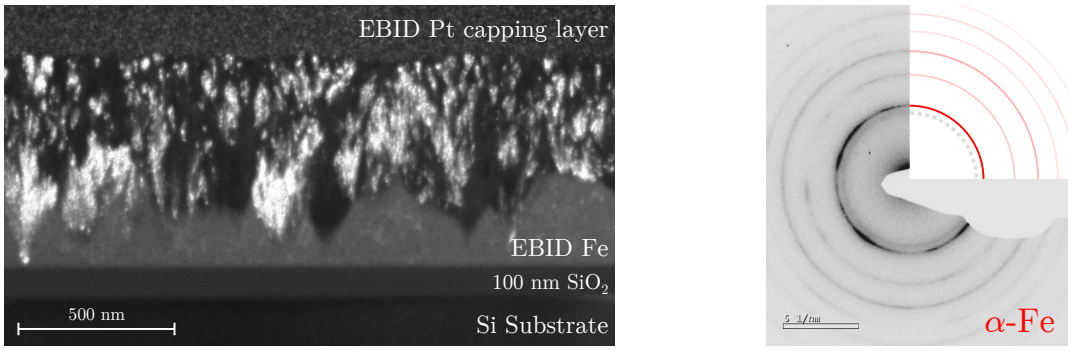

(a) **(b)**

Figure 3.4: **(a)** A DF-TEM image of a cross-sectional lamella prepared from a 670 nm thick iron microwire (78-9-13 at.%, Fe-O-C). Polycrystalline growth can be seen to extend from a nearly amorphous lower layer. **(b)** An (inverted) electron diffraction pattern of the same deposit (both growth regions). Numerous lattice spacings consistent with α-iron can be seen (in red), with an additional diffuse ring (dashed) suggesting the possible presence of some nanocrystalline iron carbide (Fe_3C). Ring transparencies are proportional to expected intensity. Lattice spacings taken from reference 38.

A very rich microstructure was revealed, in stark contrast to what was observed with SEM. In between the silicon substrate and Pt capping layer the EBID deposit, consisting of two very different growth phases, can be seen. The intermediate contrast of the lower layer of growth is characteristic of a near-amorphous material, with some intermittent white speckles suggesting a nanocrystalline structure. Also apparent in the EBID platinum capping layer, such disordered growth is common to EBID. Of more interest though, is the subsequent growth. The black/white regions seen nucleating from the lower layer and making up the majority of the wire define individual crystal grains; the wire is predominantly (poly)crystalline. The expected growth evolution is illustrated schematically in figure 3.5. It is very rare to observe such a degree of crystallisation in an as-deposited EBID material, let alone in a 'flat' deposit produced under HV conditions.[10] Furthermore, interpreted in terms of such two-phase growth, the SEM results now also make sense. Considering the first phase of growth illustrated in figure 3.5, the cluster-like features seen in thinner deposits were likely the beginnings of the

crystallisation process. In thicker deposits, the structural contrast previously granted by the amorphous/crystalline multiphase is lost as the crystalline material interconnects, leading to a homogeneous appearance.

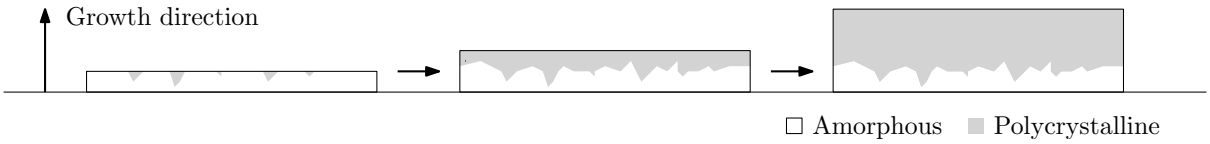

Figure 3.5: A schematic representation of the observed microstructural evolution with microwire thickness. Initial near-amorphous material eventually gives rise to polycrystalline structure.

Electron diffraction and EDX were used to further characterise the crystalline material. As shown in figure 3.4b, the deposit produced a diffraction pattern consistent with polycrystalline α-Fe (bcc), the bulk equilibrium phase of elemental iron. More curiously though, EDX revealed that although structurally dissimilar, the composition of both growth phases was the same; net iron content ($\sim$78 at.%) did not increase in the crystalline material. This is an unfortunate result, and does diminish the real value of such structure. At the same time though, it is quite informative. Firstly, it might explain why the quality of the crystalline material appears to deteriorate with thickness; why the largest crystals stem directly from the amorphous material. It is possible that during the deposition process, initial crystals are able to displace impurities into the surrounding nanocrystalline material. Those in the upper region of the deposit however, isolated from this 'impurity accepting' material, are forced to grow around contaminate species and are thus smaller. This result also suggests that the deposition process, both in manner and efficiency, did not change significantly between layers. As will now be discussed, this implies that some additional mechanism was responsible for the microstructural evolution.

For EBID and material deposition in general, composition plays an important role in determining what microstructure will develop, crystalline or otherwise. Via the use of both UHV setups and carbon-free precursors, the achievement of very pure ($>$ 95 at.% metallic), completely crystalline deposits with EBID has been detailed in literature.[10] Although these iron microwires have a lower purity, nanocrystalline features were already seen to develop in the highly disordered lower layer growth. These spontaneously nucleating nanocrystals are thought to act as seeds for subsequent polycrystalline growth. Such a probabilistic process is consistent with the fact that a significant portion of the deposit remains non-crystalline, and that such structural evolution is not universally observed in such deposits.[34,39] Another way to consider the situation is that such crystalline structure is in fact the preferred structure for material of this composition. The development from initially nanocrystalline to finally polycrystalline structure might be the result of structural or compositional disorder near the substrate. This conclusion still does not rule out the possibility that additional mechanisms also played some role in the crystallisation process however, as is discussed below.

Heat in particular is a particularly effective crystallising agent. In addition to using standard post-deposition heat treatments (annealing), crystalline deposits have been achieved with EBID both via the use of heated substrates and by exploiting beam induced heating effects[10] (further discussed in chapter 5). Although high beam currents, conducive to such heating were used to produce the wire deposits, crystallisation appears to begin very near to the substrate where heat buildup would be minimal. While not ruling it out completely, this result does suggest that heat played only a minor role, if any. Another possibility is autocatalysis. Iron is a a well known catalyst,[40] and its presence was found to greatly enhance the (thermal) decomposition of $Fe(CO)_5$.[20,41] A process of this nature could have locally enhanced the iron content at positions where (crystalline) iron was already present. However, as was already mentioned, with

composition equal in both growth phases, any additional decomposition mechanism could only be active to a limited degree.

This investigation, the first of its kind involving the $Fe_2(CO)_9$ precursor, has provided a great deal of insight into the microstructure and growth processes present in such EBID materials. Although only a limited number of samples have been investigated with TEM, SEM imaging suggests the observed microstructural evolution occurred frequently. Furthermore, provided deposition parameters are held constant, there is no reason why such growth should not persist in similar (2-D) geometries. It must be emphasised though, that while an unusual and thus fundamentally interesting result, with iron content unchanged, the practical implications of such crystallisation are less significant.

In the following section the electrical character of the microwires is investigated.

3.3 Conductivity

The electrical conductivity of a number of microwires, both thin and thick, was investigated using the standard four-point probe measurement technique outlined in subsection 2.2.3. In addition to the magnitude of the resistance, the temperature dependent behaviour of selected samples was also investigated to give insight into the mechanisms of conduction.

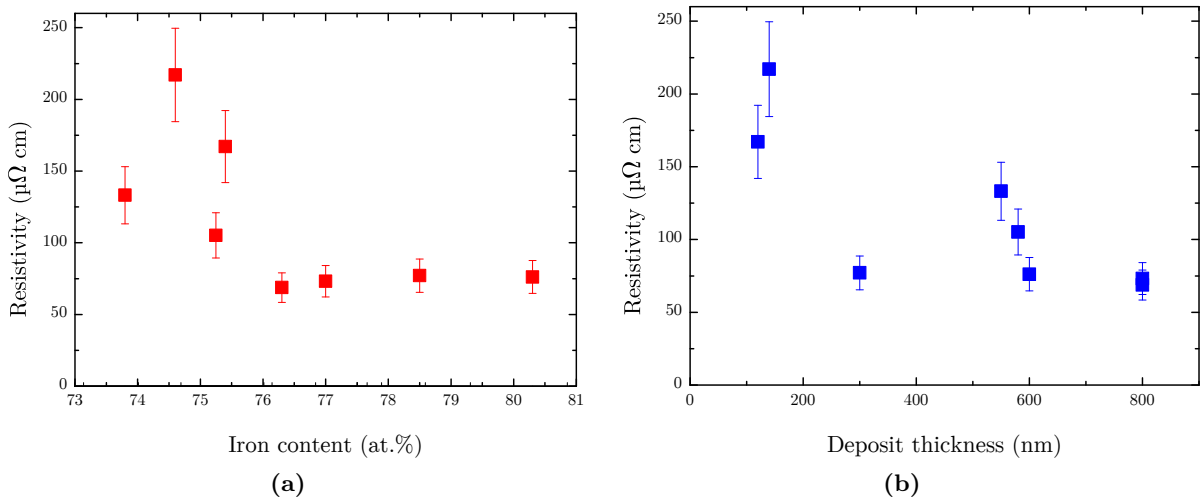

Figure 3.6: EBID microwire resistivity plotted as a function of **(a)** iron content and **(b)** height. The uncertainty in the resistivity is determined from the variance in AFM measurements (15 %). Compositional (EDX) uncertainty is taken to be ±3 at.% but is not shown due to the small compositional range plotted. For this same reason, the significance of these results should not be overstated.

Figure 3.6a shows a plot of resistivity versus iron content for eight different microwires with slightly different compositions and thicknesses. Although no clear relation between thickness and composition was found, as is to be expected, deposit resistivity decreases slightly with iron content. Average resistivity was ∼100 μΩ·cm, just one order of magnitude above that of pure iron (9.6 μΩ·cm)[42] and among the lowest resistivity achieved in as-deposited EBID material.[10] Given the high iron content of the deposits, this is not unexpected. Within an order of magnitude, these values are also consistent with the findings of Schoenaker[34]. Given the microstructural evolution revealed in the previous section, in figure 3.6b, resistivity is also presented as a function of deposit thickness. The data suggests that in spite of similar com-

positions, thinner, nanocrystalline wires, have a slightly higher resistivity than thicker, mostly polycrystalline wires. Overall, the fact that the resistivity is in general quite low for nano and polycrystalline deposits alike, implies that in all these EBID microwires, conduction takes place predominately via metallic pathways.

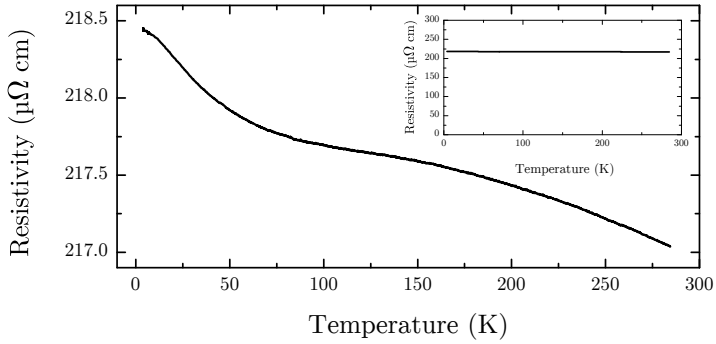

Figure 3.7: The resistivity of a 130 nm thick microwire (shown in figure 3.3d) as a function of temperature. (Inset) The same data plot over a larger resistivity range, highlighting how little the resistivity varied.

To further explore this suggestion of metallic conduction, temperature dependent measurements were performed. Figure 3.7 shows the changing resistance of a 130 nm thick microwire as a function of temperature. A very minor semiconductor-like (negative) behaviour is apparent. Over almost 300 K, the resistivity of the deposit changed by less than 1.3 μΩ·cm or 0.7 %. This corresponds to a temperature coefficient of resistance (TCR, eq. 1.3) of just -23 ppm/K, comparable to that of a resistor. Similar temperature stability was observed by Schoenaker [34] and here, as there, it is concluded to be the result of mixed conduction through both metallic and semiconducting material. With the TCR of intrinsic semiconductors is typically much larger in magnitude than that of pure metals and given the low resistivity of the deposit, the majority of conduction can be assumed to be metallic. This conclusion is consistent both with the composition and the expected microstructure of such deposits. The high iron content should allow a significant degree of conduction to take place through iron. The disordered form of this iron can be expected to be at least partially responsible for the observed order of magnitude higher resistance of the deposits. Given the significant impurity concentration however, (∼25 at.%) complete metallic percolation is unlikely. An additional factor responsible both for increased resistance and most specifically the negative TCR is conduction in, or through non-conducting materials. Electrical conduction in these EBID iron microwires is expected to be somewhat similar to conduction in the metal-insulator transition regime of standard granular metals. [11,34]

The primary impurity species present in these deposits are carbon and oxygen, typically 15 at.% each. The microstructural investigations have suggested that carbon takes on a predominately amorphous structure. Conversely, the oxygen is expected to react with the iron, forming oxides. The resistivity of both amorphous carbon and iron oxide is significantly higher than that of metallic iron. Conduction through this contaminate material can be expected to occur via thermally induced hopping or tunnelling mechanisms where electrons tunnel either directly or via localised states through the semiconducting or insulating barriers. A $\rho \propto \exp(T^{-0.5})$ behaviour (equation 1.4), characteristic of conduction through isolated granular metals is not apparent. The unusual shape of the temperature dependence data suggests that the way in which the metallic and non-metallic conduction mechanisms combine is not trivial.

In addition to a specific temperature dependence, hopping conduction of this nature often reveals itself as a non-ohmic current-voltage (IV) behaviour. [21] This was briefly investigated at

room temperature using low bias voltages (mV), but behaviour remained linear. Rather than ruling out such conduction however, this result is thought to suggest that the tunnel barriers involved are rather large, or that the extent of these semiconducting processes is too minor to detect easily. Although no measurements were performed on thicker polycrystalline deposits, given their comparable composition, complete metallic percolation remains unlikely. A slightly lower resistivity does suggest increased metallic conduction, but whether or not this increase is sufficient to change the sign of the TCR, remains to be seen.

Ultimately, only a minor dependency of the conductivity on the microstructure was revealed. Beyond this though, in spite of a negative TCR, the resistivity of deposits was found to be very low, a promising characteristic for eventual electrical applications. In the following section, perhaps the most interesting characterisation results are presented, those magnetic in nature.

3.4 Magnetism

The primary motivation behind the investigations of the $Fe_2(CO)_9$ iron precursor is the promise of ferromagnetic deposits. Magnetic characterisation is thus of particular importance. As explained in chapter 2, two different experimental techniques are used to probe the magnetic character of the EBID microwires, one electrical (magnetoresistance) and one optical (MOKE). In this section both such measurements are presented and discussed.

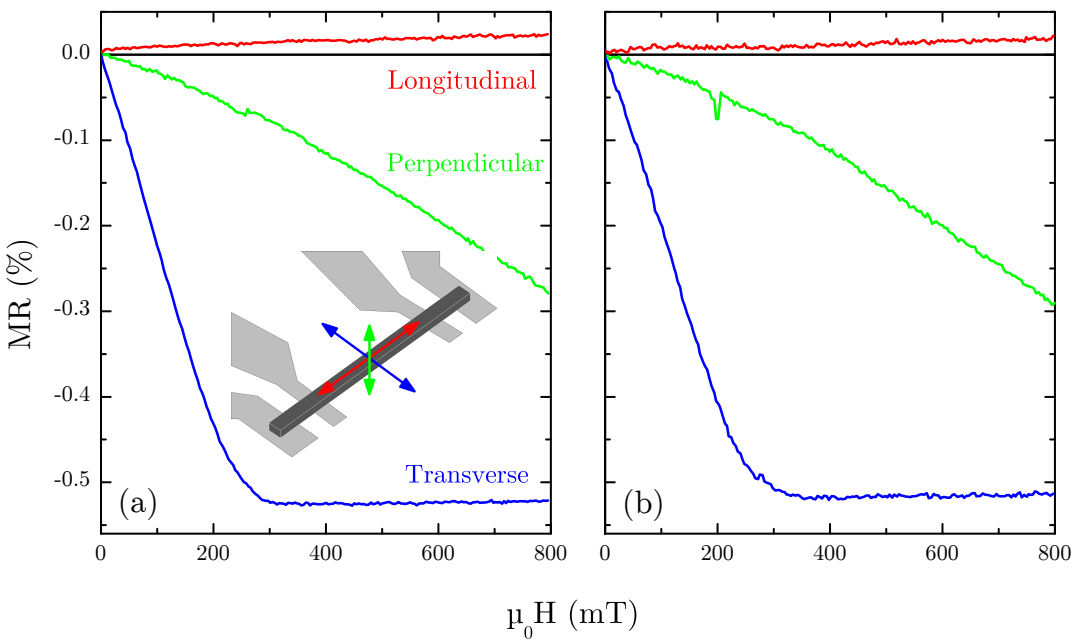

Figure 3.8: The AMR of two thin (130 nm) iron-rich microwire deposits (both 75-12-13 at.% Fe-O-C) for fields applied in three different directions (as indicated schematically). Field sweeps began and ended at -800 mT, increasing to 800 mT in between, but due to symmetry, only the MR from 0-800 mT is presented.

In figure 3.8, the MR of two thin (∼130 nm), iron-rich microwire deposits is presented. As discussed in subsection 2.2.3, MR behaviour is investigated for three different field directions. These directions, relative to the microwire, are indicated schematically in the figure. For both deposits, a very similar anisotropic behaviour is apparent. Although the application of a longitudinal field has a minimal influence on the resistance, both perpendicular and transverse fields cause the resistance to decrease. This behaviour is consistent with anisotropic magnetore-

sistance (AMR, see section 1.2.2) reaffirming[34] the ferromagnetic nature of iron-rich deposits produced from $Fe_2(CO)_9$. The limited influence of longitudinally applied fields suggests, unsurprisingly, that the easy axis of the microwires is defined by their shape and lies along the longest dimension. More specifically, this result implies that at remanence, the magnetisation is already parallel with the applied current. Correspondingly, fields perpendicular to this easy axis reduce the resistance by pulling the magnetisation perpendicular to the current. While in the transverse direction, saturation is apparent (after ∼300 mT), the 800 mT field limit of the setup was not sufficient to orientate the magnetisation in the perpendicular direction, along the hard axis. Considering shape anisotropy, this result ($H_{sat,long} \ll H_{sat,trans} < H_{sat,perp}$) is in agreement with the geometry of the microwire (length $\gg$ width $>$ thickness).

For both deposits, neither the transverse nor the perpendicular AMR curves follow the quadratic cosine behaviour expected in the case of completely coherent rotation of the magnetisation (section 1.2.2). With these thin deposits expected to have a disordered nanocrystalline or amorphous structure, and thus consist of multiple magnetic domains, this result is not surprising. A multi-domain structure is further suggested by the presence of sudden jumps in the resistance, best illustrated in figure 3.8b, in the perpendicular MR, near 200 mT. Often observed and reproducible, these jumps correspond to the abrupt reorientation of specific (groups of) magnetic domains.

In addition to AMR, a minor secondary MR is also apparent in both samples. Most visible for longitudinal applied fields but also apparent in the transverse direction after the AMR saturates (>300 mT), this MR is characterised by a very small and almost linear increase in the resistance. Being similar in both longitudinal and transverse directions, this effect seems to be isotropic and could thus be caused by ordinary magnetoresistance (OMR) (section 1.2.2). However, in OMR, resistance is increased by a reduction of the electron MFP caused by the Lorentz force. For such a mechanism to be effective the MFP must be reasonably long to begin with, which is not expected to be the case in the near-amorphous microstructure of these deposits. The exact cause is thus not clear.

Perhaps the most unusual characteristic displayed by these thinner deposits is the magnitude of the AMR. At -0.53 %, the transverse AMR of both deposits is significantly larger than that typically observed in bulk iron (0.2 %). In crystalline iron, crystalline anisotropy can enhance the AMR in certain crystallographic directions, leading to magnitudes of this order.[43] In the nanocrystalline structure of the microwires though, such an enhancement is implausible. Similarly large AMR was also observed the deposits investigated by Schoenaker[34]. Although the exact cause of this is still not known, it is expected to be a result either of the composition or of the microstructure of the deposits (or both).

As shown in figure 3.9a, transverse magnetoresistance measurements were also repeated at low temperatures. When going from 300 to 5 K, the magnitude of the MR almost doubled. As is explained in chapter 1, AMR is spintronic in nature, with resistance changes caused by increased or decreased spin mixing. All spin-polarised processes generally have some temperature dependence. In metals this is often via the MFP. Decreased lattice vibration (phonons) at low temperatures allow electrons to travel further without being scattered. In AMR, it is not scattering which is the issue specifically, but rather the kind of scattering. While impurity atoms ideally define spherical scattering potentials (Coulomb), phonons tend to have non-spherical potentials, leading to an unfavourable distortion of the SOI anisotropy and subsequently, a decreased AMR magnitude.[8,44] An increase in AMR at low temperatures, where phonon densities are decreased is thus as expected. In addition to a change in magnitude, it is also apparent that the magnetisation becomes more difficult to saturate at low temperatures. At room tempera-

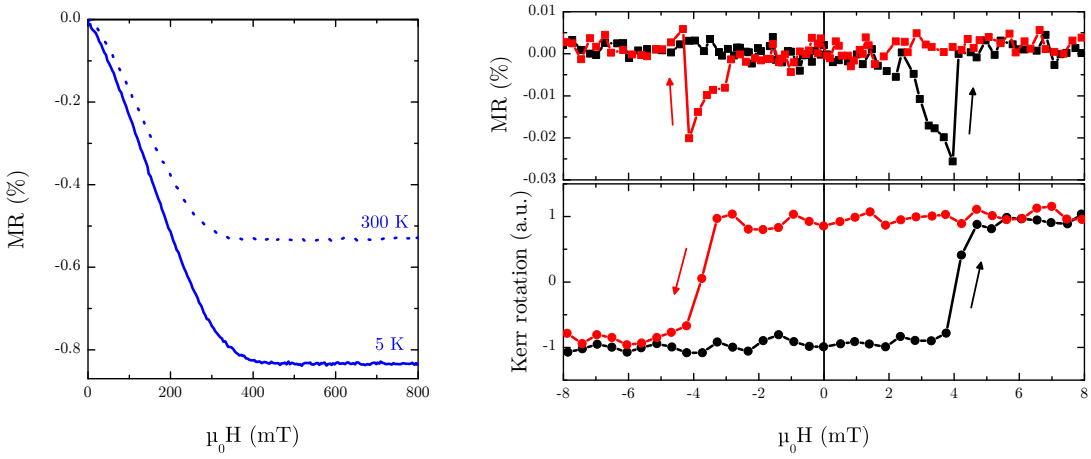

Figure 3.9: Magnetic measurements on a 130 nm thick microwire with a composition 75-12-13 at.%, Fe-O-C. **(a)** Low temperature (5 K) transverse AMR. The equivalent room temperature measure is also included for comparison. **(b)** Low-field longitudinal AMR and MOKE, illustrating ferromagnetic hysteretic switching. Black and red correspond to increasing and decreasing fields respectively.

ture the AMR and hence the magnetisation saturates at around 300 mT, while at 5 K this is closer to 400 mT. As is discussed in chapter 1 (see figure 1.3b), this is caused by the increase in saturation magnetisation at lower temperatures.

In addition to AMR, MOKE measurements were also performed on thin microwire deposits. One such measurement is presented in figure 3.9b, together with a corresponding low-field AMR measurement, for a longitudinally field. By sweeping this field from negative to positive (black lines) and back again (red lines), the switching behaviour of the wire is observed. Both the MOKE and the AMR reveal clear hysteresis, with a coercive field of approximately 4 mT. Given the different magnetic sensitivities of the two techniques, MOKE being surface and AMR bulk sensitive, by comparing measurements, additional details of the switching process can be uncovered. The switching process takes place over approximately 1 mT in both measurements, suggesting that both the bulk and surface magnetisation switch similarly.

Finally, the influence of deposit thickness on magnetic character was also investigated. In figure 3.10 the MR behaviour of three microwire deposits of increasing thickness is presented. To the bottom right of the figure, AFM profiles of these three thicker deposits and one thinner one from figure 3.10 are also shown. To give an indication of the expected microstructure of various deposits the TEM image from figure 3.4 is also reproduced to scale here.

It is clear that deposit thickness greatly influences the magnetoresistance, particularly when these results are compared to those in figure 3.8. Although remaining anisotropic, as thickness increases, AMR magnitude appears to decrease while saturation fields increase. In the two thickest deposits the MR behaviour becomes particularly erratic below 400 mT. While much of this behaviour cannot be explained exactly, is thought to be the result of the variation of two things: shape anisotropy and microstructure. As shown in the AFM profiles, as thickness increases, deposit width stays roughly the same. Consequently, a realignment of the hard axis, from in the perpendicular direction to the transverse direction can be expected as deposits get thicker. This is directly observed in the AMR results. In the thinnest deposits (figure 3.8 and figure 3.10(i)) the resistance decreases fastest for transverse fields, suggesting that the magnetisation is easier to rotate in this direction than in the perpendicular direction. In thicker deposits though, this

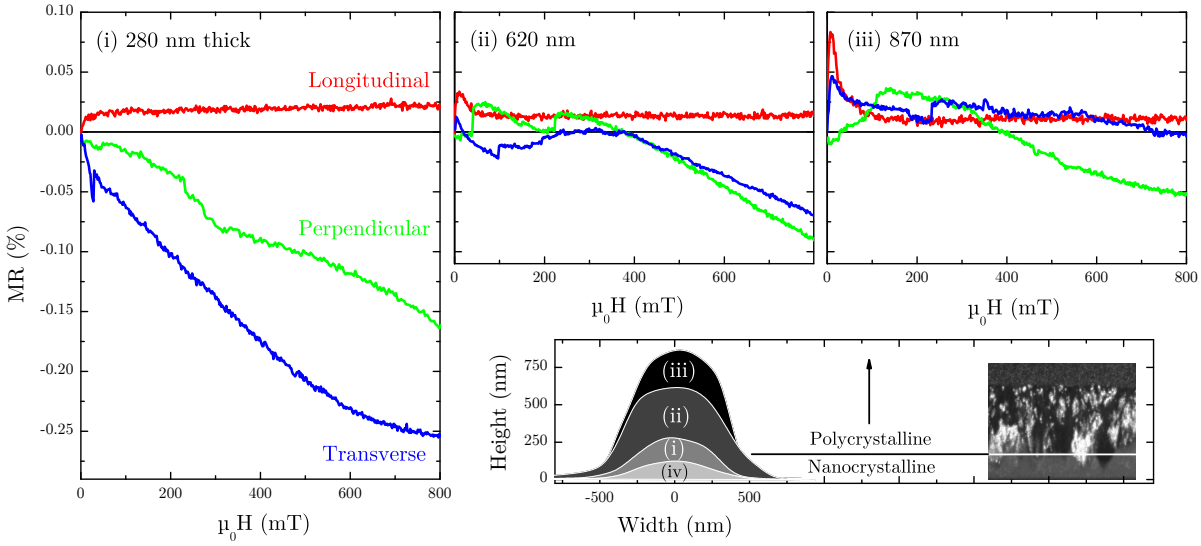

Figure 3.10: The AMR of deposits of increasing thickness but similar iron content (∼75 at.%). AFM profiles illustrating their differing thicknesses are shown bottom right together with the TEM image from figure 3.4, indicating the expected microstructure (a profile of the deposits from figure 3.8 is also included (iv)).

difference first decreases (figure 3.10(ii)) and finally reverses (figure 3.10(iii)). A related effect is also visible in the longitudinal MR. In the thinnest deposits (figure 3.8) a longitudinal field has little effect at low fields (<100 mT), suggesting that the magnetisation already lies in this direction as a result of strong shape anisotropy. In these thicker deposits however, this is not the case, and such a field does induce a small positive increase in the resistance as it aligns the magnetisation along the wire. The exact cause of much of the more complex MR behaviour in the two thickest wires is not known. It is reasonable to assume though, that this might relate to a changing microstructure since both are expected to consist primarily of polycrystalline iron. MOKE measurements were also attempted on thicker deposits (not presented here) but resulting behaviour was incomprehensible.

Ultimately, as demonstrated by figure 3.8, provided a microwire deposit has a well defined easy axis (length $\gg$ width $>$ thickness) and consists of a single and simple structural phase, very straightforward magnetic behaviour reproducibly results. Both AMR and MOKE results clearly indicated ferromagnetic behaviour. But there is still a great amount to be understood, particularly in thicker deposits. Ideally, the two suspected primary causes, shape anisotropy and microstructure, should be investigated separately. This could be achieved by characterising deposits with similar structure but with different geometry.

In the last section of this chapter the effect of annealing such microwire deposits is briefly explored.

3.5 Annealing

As is evident from the results presented throughout this chapter, even as-deposited, iron microwires produced by EBID of $Fe_2(CO)_9$ display a number of promising characteristics, electrical and magnetic alike. However, as a final and ultimate indication of the potential of EBID with the $Fe_2(CO)_9$ precursor, post deposition heat treatment has been investigated. Although focusing on just a single iron-rich microwire, this pilot investigation is the first of its kind successfully carried out a deposits made with this new iron precursor. One of the thin (130 nm) iron microwires investigated in the previous section was annealed at 300 K in an argon environment (∼1 atm) for 30 minutes. A longitudinal magnetic field of 250 mT was applied during annealing to help define the easy axis.

An issue commonly encountered when annealing nanostructures is geometric distortion caused by the transport or removal of contaminates.[10] For this microwire, containing 75 at.% iron, 92 % by volume, such distortion is of little concern and indeed, post-annealing AFM revealed minimal geometric variation. After annealing, the (room temperature) resistivity of the deposit decreased from 170 to 90 µΩ·cm. The temperature dependence of the resistivity was also reinvestigated, as can be seen in figure 3.11a. A definitively metallic behaviour was revealed; from room temperature to 5 K the resistivity almost halved corresponding to a TCR of 1900 ppm/K (TCR_{Fe}=5000 ppm/K).[42] As expected for metallic conduction, the resistivity begins to plateau at low temperatures (< 30 K) as thermally induced phonon-scattering ceases, leaving just intrinsic defect and impurity scattering. As discussed in section 1.2.2, this intrinsic resistivity can be used to indicate the purity of the material (carrying the conduction) in the form of the residual resistivity ratio or RRR. An RRR of 1.9 was determined for the annealed microwire, far from that of high purity iron (> 300),[42] but comparable to that of thin films (20 nm) produced by MBE (3.3).[45]

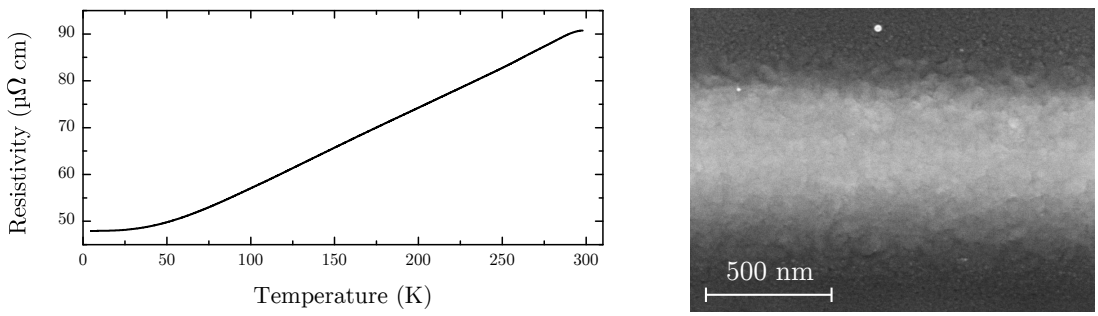

(a) **(b)**

Figure 3.11: **(a)** The resistive temperature dependence and **(b)** SEM image of an annealed microwire (130 nm thick) with an original composition of 75-12-13 at.% Fe-O-C.

Figure 3.11b shows a SEM image of the annealed deposit. When compared to its as-deposited appearance (figure 3.3d), significantly more structure is apparent. Grain-like features can be seen, and given the electrical results, these are expected to be consist of metallic iron. EDX spectroscopy could only be performed a few days after the annealing and electrical measurements took place. Measurements suggested that post annealing, composition worsened significantly, to 46-47-7 (Fe-O-C at.%). Such a composition is clearly incompatible with the electrical characterisation results. Oxidation is expected to be the cause. Although, as discussed in appendix A, oxidation was general not an issue with as-deposited iron samples, likely due to their inherent oxygen content, the purification induced by the annealing could have eliminated

this stability.

The magnetoresistance of the annealed deposit was also reevaluated and is shown in figure 3.12. Although AMR is still clearly the primary magnetoresistive mechanism, a number of changes are apparent compared to the MR before annealing (figure 3.8). The magnitude of the MR has reduced significantly, to something closer to that of pure iron. This further implies that the enhanced AMR seen in as-deposited thin samples is either due to their composition or microstructure. The shape of the AMR has also changed, with both the transverse and in particularly the perpendicular MR became more quadratic in nature. Although still expected to be multi-domain (especially given the granular appearance), this result suggests a more coherent magnetic rotation due to increased magnetic interaction between domains, likely caused by the removal of non-magnetic contaminate species. As is apparent from the low field longitudinal MR in figure 3.12b, the coercivity of the deposit also increased, almost doubling to 7 mT. This is further consistent with the idea that the magnetic interaction between grains has increased. A slight increase in resistance for small longitudinal fields (<100 mT) suggests that the remanent magnetisation is not completely aligned along the axis of the wire. The 250 mT field applied during annealing should have been sufficient to achieve alignment in the longitudinal direction. This could suggest the development of an additional anisotropic mechanism, such as crystalline anisotropy. With deposit geometry unchanged, saturation fields are again in expected proportion ($H_{sat,long} \ll H_{sat,w} < H_{sat,t}$).

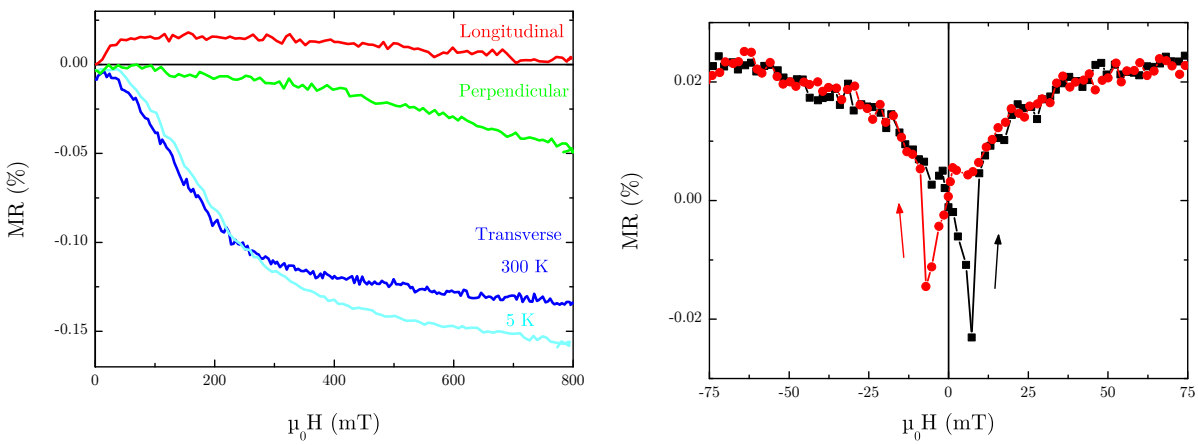

Figure 3.12: The AMR of an annealed microwire deposit at **(a)** high fields (including at low temperature) and **(b)** longitudinal low fields.

Just as before annealing (figure 3.8), in addition to AMR, a secondary isotropic linear MR effect is also apparent. While positive before annealing, as can be seen in figure 3.12a for longitudinal fields of above 100 mT and transverse fields above 300 mT, here it is negative. This is thought to be caused by *normal magnetoresistance* (section 1.2.2).

Low temperature AMR (5 K) measurements were also repeated, again for a transverse field. As shown in figure 3.12, annealing all but eliminated the previously significant temperature dependence of the AMR. As was previously discussed, the temperature dependence of AMR is thought to be the result of the different scattering potentials of phonons and impurities. In this annealed sample, a transition from phonon dominated to impurity/defect scattering at low temperatures is clearly apparent (figure 3.11a). Subsequently, this result cannot be explained. In contrast, the high field MR does display a temperature dependence, increasing slightly. This is consistent with the assumption that it is caused by normal magnetoresistance.

These preliminary results are quite promising. For the first time, magnetic conduction has been achieved in a deposit produced from the $Fe_2(CO)_9$ precursor. Although no detailed investigation was carried out, the microstructure appears to crystallise. One major issue appears to be oxidation. EDX suggested that after a few days in air, oxygen content increased to 50 at.%. Unfortunately the sample was destroyed before additional electrical measurements could be performed to confirm this. This was just a pilot experiment, and a lot more could still be learnt. By investigating the conductance as a function of annealing conditions (time, temperature) it might be possible to observe the transition from semiconducting to conducting behaviour more systematically. By then also investigating how the microstructure evolves, a great deal of insight could be gained.

3.6 Conclusions

In this chapter, iron-rich (∼75 at.%) microwire deposits produced by EBID of $Fe_2(CO)_9$ have been broadly characterised. Microstructural investigations revealed a rather unusual growth process. Although the microwires begin nearly amorphous, after reaching thicknesses of around >200 nm, a crystallisation takes place (bcc iron). Electrically, the microwires are highly conductive (100 µΩ·cm), but due to a small degree of non-magnetic conduction, display negative temperature dependent behaviour. Both AMR and MOKE measurements revealed ferromagnetic behaviour. However in thick deposits, at least in part due to the changing microstructure, this behaviour could not be well explained. For the first time, the influence of annealing was also investigated. While metallic conduction was induced, the deposit also oxidised rather quickly.

With the $Fe_2(CO)_9$ precursor it is thus possible to reliably deposit magnetic, conductive material. But a number of things are still not clear and should be further investigated. Of particular value would be a better understanding of the crystallisation process and most specifically, why iron content does not increase as a result. The annealing process should also be further explored. By optimising annealing conditions, the observed rapid oxidation might be able to be avoided.

As mentioned in the introduction, the results of this section on optimal deposits effectively set a benchmark for what can be achieved. In the next chapter, these results are contrasted against microwire deposits produced in below-optimal conditions, specifically, at high water vapour pressures.

Chapter 4

Tuning Iron Content

Up till now, investigations into the $Fe_2(CO)_9$ precursor have focused largely on optimisation; maximising the iron content of deposits.[4,34] From an application stand point this is not unusual, but it has left the rest of the compositional spectrum, including the other extreme of low iron content, relatively unexplored. Although deposits of this nature maybe of little interest individually, a systematic study highlighting how their character – structural, electric and magnetic – changes with composition could prove insightful. This chapter details such an investigation.

Given its significance both in EBID and in iron chemistry in general, this study focuses on the influence of oxygen, or specifically, how deposit properties change as their iron-oxygen ratio is artificially modified. Composition control has been achieved by artificially altering (worsening) vacuum conditions via the injection of water vapour. With oxygen defining a primary contaminate species in EBID iron material, a better understanding of its influence might eventually allow even higher iron purities to be achieved. The EBID of iron oxide itself is also of interest, particularly Fe_3O_4 given its half metallic nature and thus potential for spintronic application.[29]

Using the optimal electron beam and patterning settings described in the previous chapter, a number of microwire deposits (see section 3.1) with varying iron-oxygen ratios were produced for this investigation by purposely increasing the partial water pressure. Combined with the iron-rich deposits investigated in the previous chapter, depositions over a broad compositional range have been studied. Due to the unusual thickness-dependent behaviour encountered in the previous chapter, the investigations of this chapter focus on microwires with a thickness below $\sim$250 nm.

In the following sections, after further detailing the experimental technique, first the microstructural and then the electric and magnetic properties of these microwire deposits are presented. Results are summarised and discussed at the end of the chapter where conclusions are also presented.

4.1 Production Details

Controlled water injection was achieved using the same technique previously employed by Schoenaker[34]. With a reservoir containing magnesium sulfate heptahydrate ($MgSO_4(H_2O)_7$) as a source, water vapour was introduced to the vacuum chamber through a second GIS needle and regulated by a needle valve. The water released by the vacuum dehydration of this salt is more commonly used in conjunction with TEOS (Tetraethyl orthosilicate, $Si(OC_2H_5)_4$) for the EBID of SiO_2.

Under optimal conditions (considered in the previous chapter), the water vapour partial pressure in the vacuum chamber is typically below 2×10^{-7} mbar leading to deposits containing around 75 at.% iron and no more than 15 at.% oxygen. Using the above technique however, water pressures upwards of 1×10^{-5} mbar have been readily achieved. Initially, the composition of deposits made at higher water pressures was inconsistent; often two deposits produced under the same partial water pressure at different times had compositions deviating by more than 10 at.%. It was found that when a second gas is injected into the vacuum chamber with a pressure of the same order of magnitude as the precursor itself, pressure stability becomes very important. This is illustrated in figure 4.1a. Ordinarily, when depositing without additional water vapour (left of the figure) the pressure of the $Fe_2(CO)_9$ precursor has little to no influence on the content of deposits. With water however, as indicated in the right of the figure, producing deposits of constant composition is only possible after the precursor pressure is stable.

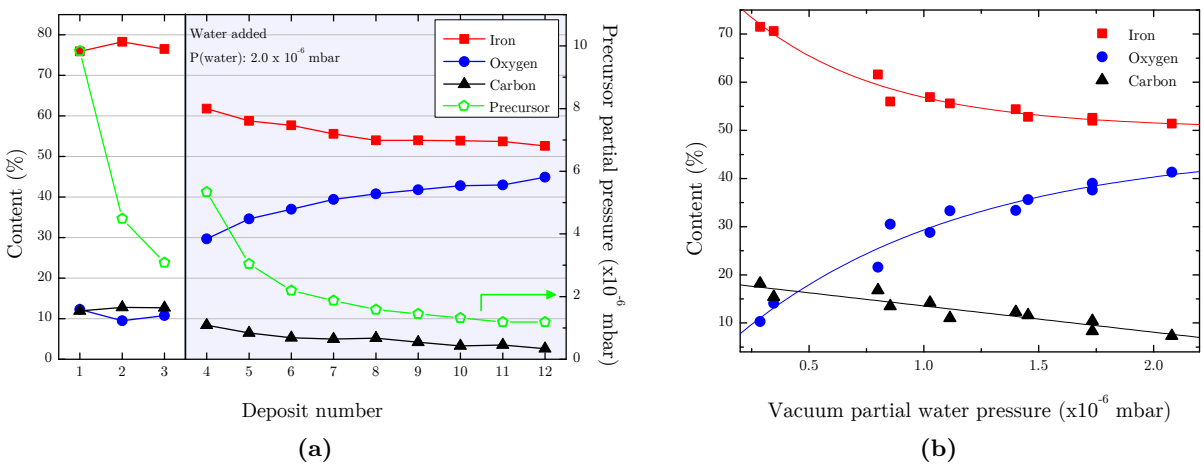

Figure 4.1: **(a)** The composition of 12 deposits (1 µm x 1 µm, 75 s each) produced at different precursor pressures. 1-3 were produced under optimal conditions while for deposits 4-12 additional water vapour was introduced into the vacuum chamber. Composition was only reproducible at stable precursor pressures. **(b)** Deposit composition as a function of water vapour partial pressure illustrating the control granted. The plot shows the composition of a total of 11 deposits (500 nm x 500 nm, 75 s each), half of which were produced as the water pressure was gradually increased and half as it was decreased. The first and last deposits were produced with the water flow off. For all depositions the GIS needle introducing the water was position approximately 1 mm from the deposition location. Partial water pressure measured with the RGA.

As shown in figure 4.1b, with this requirement realised, the influence of the injected water vapour on deposit composition could be reliably calibrated. As suggested by the plot, oxygen content saturated at around 45 at.%. Neither very high water pressure ($> 5\times10^{-6}$ mbar) nor very low precursor pressure (Fe GIS retracted: an order of magnitude below normal) lead to significantly higher values suggesting the limitation was intrinsic. Shimojo et al.[29] found a similar limitation when depositing $Fe(CO)_5$ and attributed it to the preferential formation of

a particular oxide (in their case Fe_3O_4, 43:57, Fe:O). The results from a second publication by Shimojo et al.[30] also justify why water vapour instead of pure oxygen should be used. Oxygen was found to have a significantly diminished compositional influence. Water vapour, in addition to increasing the oxygen content of deposits, also specifically decreased carbon content. It is suggested that the cause of this is the occurrence of the so called *water gas shift reaction* (CO (gas) + H_2O (vapour) $\rightarrow$ CO_2 (gas) + H_2 (gas)), a reaction enhanced by the presence of an iron oxide catalyst.[31]

4.2 Microstructure

As in the previous chapter, both SEM and TEM techniques were utilised to investigate deposit microstructure. Beginning again with the simpler of the two, figure 4.2 shows SEM images of three microwire deposits with differing iron:oxygen ratios.

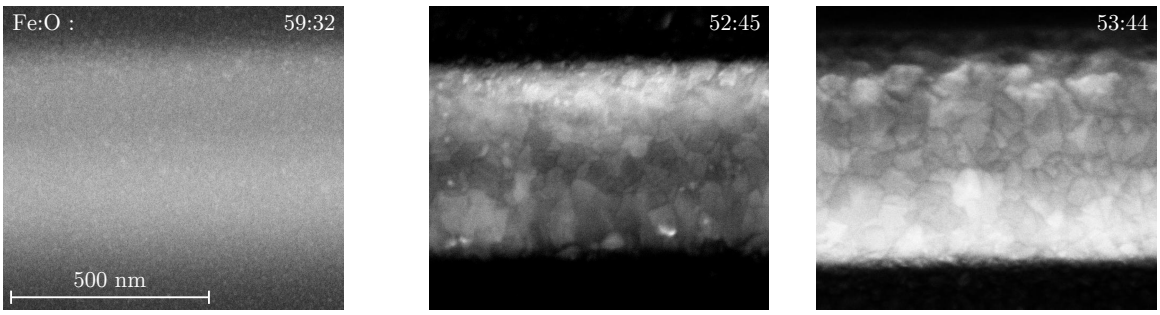

(a) **(b)** **(c)**

Figure 4.2: High-magnification SEM micrographs (10 kV, ≤1 nA, immersion lens, TTL detector) of three EBID iron microwires all approximately 200 nm thick with compositions (Fe-O-C at.%) **(a)** 59-32-9 **(b)** 52-45-3 **(c)** 53-44-3. Images are at equal magnification, as indicated in **(a)**.

As water vapour pressure was increased, deposits initially maintained their mostly featureless SEM appearance (figure 3.3). Once the iron-oxygen ratio approached 60:30 however, as illustrated by figure 4.2a, a granular structure arose. Given the increasing oxygen content, these grains are expected to consist of iron oxide. As oxygen content was further increased a more remarkable microstructural developed. Shown in Figures 4.2b and 4.2c, below approximately 55 at.% iron (Fe:O∼55:43) towards the lower limit of achievable iron content, a very clear crystalline growth became apparent, consisting of clearly distinguishable grains tens of nanometres across. This microstructure was further investigated with TEM and electron diffraction.

Figure 4.3a shows a DF-TEM image of a lamella made from a microwire with a Fe:O ratio of 52:45 (the deposit from figure 4.2b). A remarkable columnar crystal growth was revealed, with some grains extending almost the entire thickness of the deposit, some 200 nm. Structurally homogeneous except for a thin interface layer at the substrate, EDX line scans also indicated a mostly uniform composition across the lamella. The crystalline nature of the deposit was further confirmed with HR-TEM, as shown in figure 4.3b, with ordered atomic lattices clearly visible. To better identify the crystalline material, electron diffraction was carried out. A complex diffraction pattern resulted, as can be seen in figure 4.3c, consisting both of diffuse rings (nanocrystalline) and specific bright points (single crystals). The pattern was compared and fit to literature values.[38] No crystalline iron was detected, instead, the material was identified as iron oxide. α-Fe_2O_3 was conclusively matched as illustrated by the red rings in the figure. Additional spots were also observed, consistent with either Fe_3O_4 or γ-Fe_2O_3 which are structurally

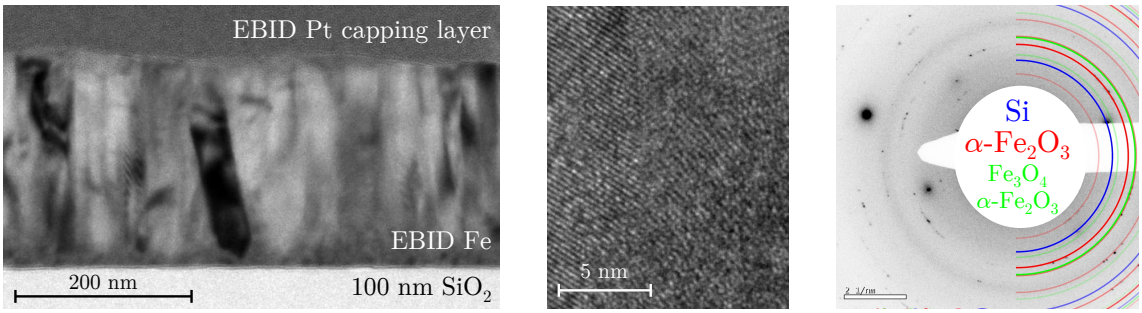

(a) **(b)** **(c)**

Figure 4.3: **(a)** Dark-field and **(b)** high-resolution TEM images of a lamella prepared from the microwire deposit shown in figure 4.2b. **(c)** The electron diffraction pattern (inverted) produced by the lamella. Iron oxide was identified as α-Fe_2O_3 (red) and Fe_3O_4 and/or γ-Fe_2O_3 (green). Bright spots from the silicon substrate can also be seen (blue). Ring opacity is scaled relative to the expected intensity. Lattice spacings are taken from ref. 38.

very similar.

Given increasing oxygen levels, eventual oxidation of the iron was never in doubt. What is surprising, however, is the fact that this oxide took the form of large (on the scale of the deposit) crystals. As is discussed in the previous section, in addition to increasing the oxygen content, the deposition of iron in the presence of water vapour also tends to reduce the carbon content. Indeed, the microwires with maximal oxygen content (∼50 at.%) had a carbon content of only a few percent. It may be this high Fe-O purity which allowed such crystallisation to occur. Furthermore, the onset of crystallisation very near the minimum of achievable iron content does suggest that this limitation is a result of the preferential formation of an iron-oxide. So far, however, results are not conclusive enough to accurately determine the exact origin or phase.

These results and their implications will be further discussed at the end of the chapter together with subsequent electrical and magnetic characterisation results which will be presented in the coming sections.

4.3 Conductivity

The influence of composition (Fe:O) on resistivity was investigated for a number of microwire deposits. As in the previous chapter, in addition to simple room temperature measurements, the resistance of selected samples was also measured as a function of temperature. As usual, measurements were carried out using a four-point probe technique and resistivity was calculated using the AFM-determined cross-section of deposits. A number of deposits were also investigated in Zaragoza.

In figure 4.4 the room temperature resistivity of numerous microwire deposits is plotted as a function of iron content (and inset as a function of the iron-oxygen ratio).

Deposit resistivity increased significantly as iron content decreased. Between the purest deposits and those with a near equal ratio of iron and oxygen, the resistivity increased more than three orders of magnitude. As highlighted by the two lines in the main figure, two unique trends are apparent in the data. The majority of deposits had resistivities following an exponential trend extending all the way down to pure iron. Below approximately 52 at.%, however, deposit resistivity increases more sharply. As the inset shows, when plot as a function of the iron-

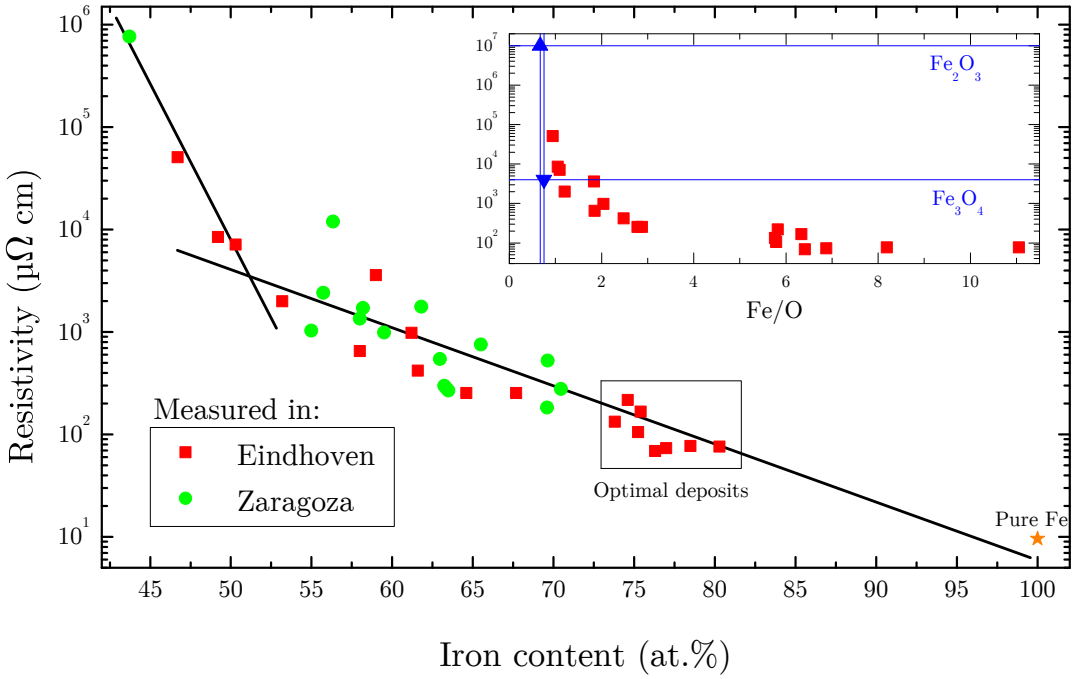

Figure 4.4: The resistivity of numerous microwires as a function of iron content. Measurements performed both in Eindhoven and in Zaragoza are shown. The theoretically resistivity of iron [42] and the measurements from the previous chapter are also shown for comparison. Inset: the Eindhoven data re-plotted as a function of iron content divided by oxygen content. Selected iron oxide resistivities (bulk) are also included. [15–17]

oxygen ratio, a similar though more gradual trend is observed. From the asymptotic increase in resistivity it is also clear here that iron oxide forms. Considering the microstructural results, this critical composition (52 at.%) corresponds nicely to the value below which columnar iron oxide crystal growth was observed. It is assumed that when possible, conduction will take place through the disordered intergranular material rather than the developing oxide grains. Consequently, this correlation seems to imply that at this point, conduction begins to be forced through the resistive oxide grains which now dominate the microwire structure. Effectively this is where percolation of the amorphous, conducting intergrain material ceases.

To continue electrical characterisation and among other things, test the above assumption, the mechanisms of electrical conduction have been investigated with temperature dependent measurements. Two deposits, one with a medium iron content (59:32) and the other with minimal iron content (49:47) were characterised. The results are shown in figure 4.5.

Both deposits exhibited semiconductive behaviour, with resistivity increasing mostly linearly as temperature decreased. From a room temperature resistivity of ∼3500 μΩ·cm, the resistivity of the deposit containing 59 at.% iron increased to almost 5500 μΩ·cm at 5 K, corresponding to a TCR of around -1900 ppm/K. The deposit containing just 49 at.% iron exhibited an even stronger temperature dependence, with a TCR approaching -5800 ppm/K. Although significantly more temperature sensitive than deposits with very high iron concentrations (figure 3.7, -23 ppm/K), this behaviour is still minimal when compared to that of pure iron oxides. Although the TCR parameter (equation 1.3) does not accurately describe the highly non-linear temperature behaviour of insulators, it can be used to give an impression of the comparatively extreme temperature dependence of pure iron oxides. When assumed linear, both Fe_3O_4 and Fe_2O_3 yield a TCR of the order of 1×10^6 ppm/K [15,16] or greater. [46] This is a clear indication that even in these microwire deposits, a significant degree of conduction still takes place through

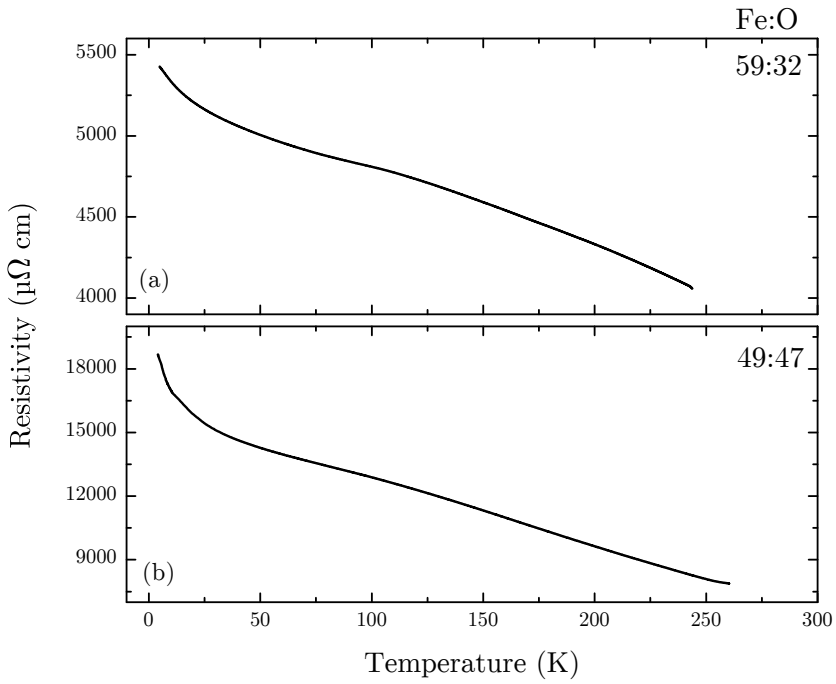

Figure 4.5: The resistivity of two microwire deposits, compositions (Fe-O-C at.%) **(a)** 59-32-9 and **(b)** 49-47-4, as a function of temperature.

conductive material.

Crossing the previously critical composition of ∼55 at.% iron appears to have no significant influence on the temperature dependent behaviour. The most notable difference between measurements, apart from the increase in resistance, is a larger upturn of the resistivity at very low temperatures (<20 K) in the deposit displaying a columnar oxide structure. Although less notable than the variation seen both in the microstructure and in the conductivity, a progression towards such asymptotic low temperature behaviour is consistent with increased conduction through iron oxide.

In the next section, the influence of all these compositional variations on the magnetism of the microwire is finally discussed.

4.4 Magnetism

The last parameter characterised as a function of deposit composition is the magnetic behaviour. Most iron oxides exhibit some form of magnetism but as was discussed in subsection 1.2.3, it is often more complex than the simple ferromagnetism of pure iron. With Fe_3O_4 ferrimagnetic and α-Fe_2O_3 very weakly ferromagnetic at room temperature, a notable change in magnetic behaviour is expected to be visible as the composition is varied.

In figure 4.6 three MR measurements from microwire deposits containing 75, 59 and 49 at.% iron are presented ((a-c) respectively, (a) reproduced from the previous chapter). A MOKE measurement from the deposit containing 59 at.% iron is also included in (d).

Considering the MR of the two deposits with increased oxygen content (figure 4.6b and 4.6c), both display two independent MR phenomena for low (<100 mT) and high (>100 mT) applied

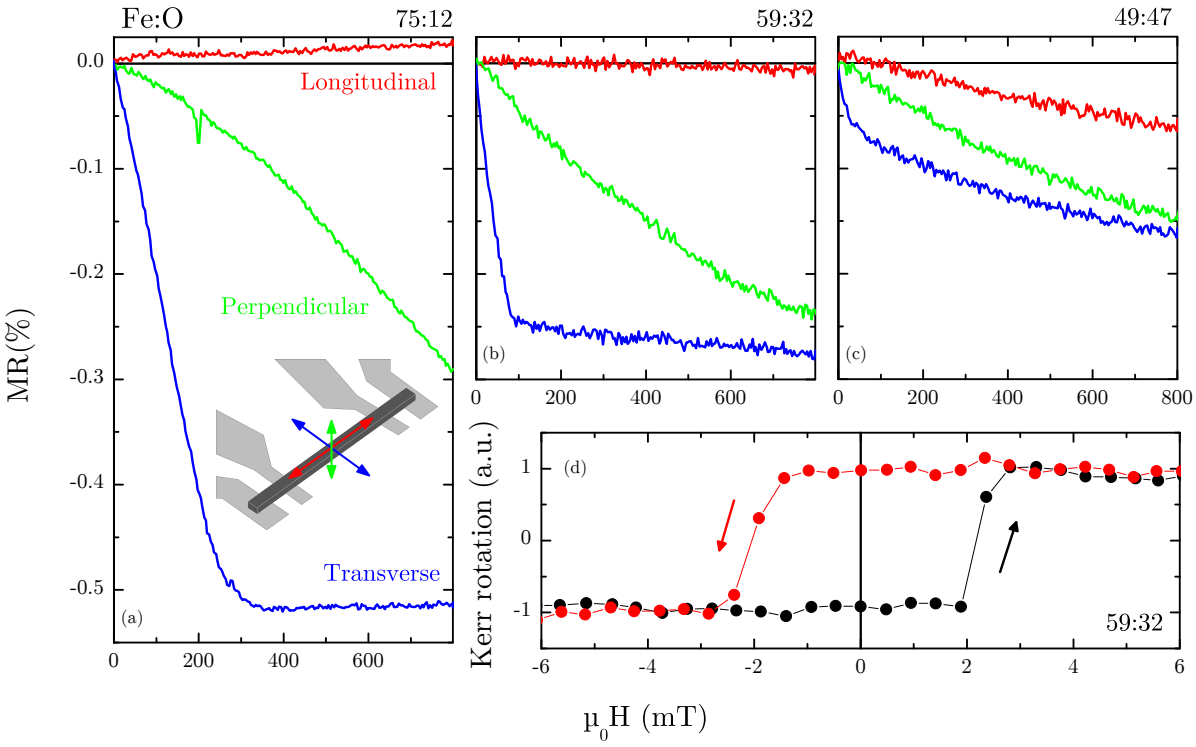

Figure 4.6: **(a-c)** Magnetoresistance measurements of three different microwire deposits with different compositions. **(a)** 75-12-13 (Fe-O-C at.%), reproduced from chapter 3, **(b)** 59-32-9, and **(c)** 49-47-4. Only positive field MR is shown (made by sweeping from -800 mT to +800 mT) due to symmetry. The three field directions are again schematically indicated in (a). **(d)** A MOKE measurement of the sample containing 59 at.% iron.

fields. At low fields a directionally dependent effect characteristic of AMR is apparent. The applied field induces minimal resistive variation in the longitudinal direction but a notable decrease in the transverse and perpendicular directions. At higher fields however, after saturation of the AMR, a second smaller MR is apparent. Unlike the AMR, this effect appears to be isotropic, having an almost equal negative effect on the resistance for all field directions. Furthermore, it was found to be very difficult to saturate; similar samples measured in Zaragoza showed no signs of saturating even at 9 T.

This high-field effect is characteristic of an extrinsic (structurally induced) MR observed in a number of magnetic oxides,[47] including the half-metal Fe_3O_4. Observed in polycrystalline samples, it is thought to be the result of spin-dependent electron transport between magnetic grains and is consequently known as Grain Boundary Magnetoresistance (GBMR). The finer details of the process are still debated, but the basic concept is illustrated in figure 4.7. Conduction takes place primarily via crystalline Fe_3O_4 (and is thus spin polarised), but between grains, electrons must travel through an intergranular material via the magnetically disordered boundary of the grains. The nature of this transport depends on the conductive properties of the intergranular material, but in any case, transport of the spin polarised current through the grain boundary magnetisation ensures a magnetoresistive effect. As an external field aligns this surface magnetisation with the spin of the grains and electrons, resistance decreases. For conductive intergranular material a GMR-like spin-dependent scattering can take place.[48,49] If sufficiently insulating however, tunnelling behaviour, essentially TMR, is also possible.[50–52 53,54] The position of the magnetisation on the surface of the grains, as well as the possibility for structural and compositional disorder can lead to a very strong and complex anisotropic behaviour making

it very difficult to saturate. Fields as high as 42 T have been applied to Fe_3O_4 samples of this nature without achieving saturation.[55]

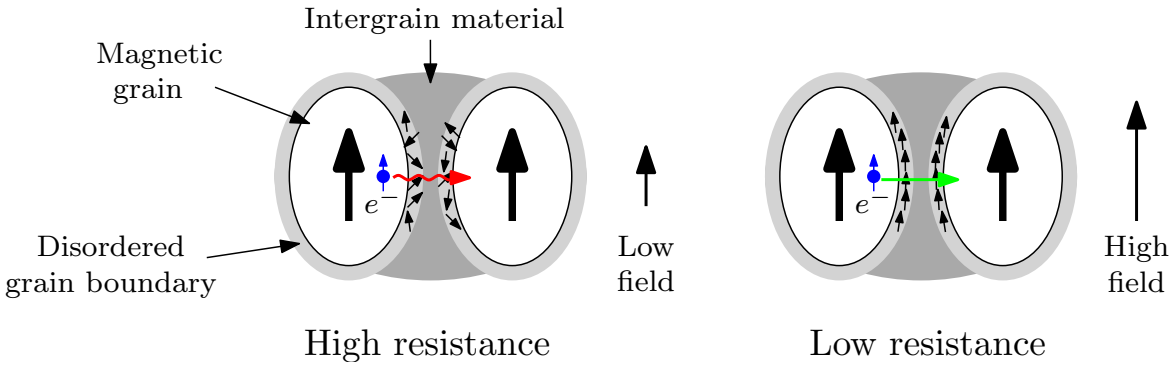

Figure 4.7: A schematic illustration of grain boundary magnetoresistance (GBMR). Explained in the text.

Given the similarities of the MR, and the fact that Fe_3O_4 was identified in the crystalline microwire deposit (figure 4.3c), such a mechanism is thought to be responsible for this high field effect. Questions remain however. The biggest uncertainty relates to the nature of the intergranular material and whether this spin polarised transport is based on scattering or tunnelling.[56] Although some results published by Ziese et al.[48] suggest that a high field MR of this nature can arise in Fe_3O_4 films independent of their Fe_2O_3 content, ultimately Fe_3O_4 must be responsible for producing a spin polarised current. Often the more resistive Fe_2O_3 is suggested to form around Fe_3O_4 grains as they oxidise thereby defining an intergrain tunnelling barrier. With Fe_2O_3 detected in deposits such an idea seems reasonable, at least in those deposits exhibiting columnar crystal growth. As was discussed in the previous section, in deposits containing intermediate iron percentages (∼60 at.%), conduction is expected to be carried primarily by the percolating intergranular material rather than the oxide grains. In these microwire deposits, which also display a small degree of GBMR, such a concept becomes more difficult to apply. With the size of this GBMR an order magnitude below that typically found,[48–52,55] it is possible that the degree of spin polarised transport in the EBID microwires is simply very small. In any case, an all encompassing explanation of this high field effect remains to be developed.

As shown in figure 4.6d, MOKE measurements were also performed. Measurements on deposits containing a low percentage of iron (∼50 at.%) were unsuccessful. It is possible that the surface of such deposits is not suitable for Kerr microscopy, being insufficiently magnetic or reflecting, possibly due to excess oxidisation. At 59 at.% however (59:32), strong signal was measured as presented in the figure. As also found with the iron-rich microwires, rather square hysteretic behaviour was measured, consistent with coherent rotation of the magnetisation. This further suggests that conduction takes place via the intergranular material rather than the sparse and thus weakly interacting grains themselves.

In subsection 1.2.1 it was mentioned that superparamagnetism can often arise in magnetic granular materials. It is clear from these results that this is not the case here. For deposits with minimal iron content (∼50 at.%), the significant size of the crystal grains (∼10 x 200 nm) makes superparamagnetism unlikely and the MR behaviour of the deposits confirms this suspicion. As seen in figure 4.6c, when a longitudinal field is applied to the deposit no sudden change in the resistance is observed (due to AMR); the magnetisation does not change direction. This suggests that at zero field, the magnetisation already points in the longitudinal direction, following shape anisotropy. Such a remanent magnetisation would not occur in a paramagnetic material. It could be more reasonable to expect such a superparamagnetic effect in those deposits with an

intermediate iron content (∼60 at.%), containing smaller grains. However, with these grains thought to consist of iron oxide and representing only a secondary source of magnetism after the iron-containing intergranular material, this is also not expected here. In addition to the AMR, the magnetic hysteresis observed with MOKE also confirms coherent magnetic behaviour. Superparamagnetism is not expected to arise at any of the compositions achievable with the water injection method detailed in this chapter.

In the following final section all the characterisation results presented in this chapter will be summarised and discussed together. Combined with the results of the previous chapter, an overview of how the various material characteristics of the EBID iron microwires evolve with changing iron and oxygen content is presented.

4.5 Concluding Discussion

The influence of oxygen content on the various characteristics of deposits produced from the $Fe_2(CO)_9$ precursor is becoming clear.

As was concluded in the previous chapter, provided deposits are not made too thick, under optimal vacuum conditions, material with a typical composition of 75-13-12 at.% (Fe-O-C) can be readily deposited. Such deposits take on a mostly amorphous or nanocrystalline appearance. A large proportion of iron makes metallic percolation significant but not complete. Consequently, conduction in this material is high but still slightly semiconducting in nature, with the TCR small but negative. Magnetically, these deposits display a rather large AMR behaviour, also due to the significant conduction through iron.

Much of this behaviour remains unchanged as the water vapour pressure and hence oxygen content is gradually increased. The excess oxygen incorporated into deposited material mixes into the amorphous composite leading to a very similar microstructure, but higher resistances. At a certain point however, near an oxygen content of approximately 30 at.% (60 at.% iron), small grains of iron oxide begin to form. With conduction still carried primarily by the intergranular amorphous material, the resistance increases, but not significantly. Magnetically, given the possibility for intergranular transport, a second MR effect arises (GBMR) in addition to AMR. As oxygen content increases further the grains enlarge and ultimately, at a critical composition of ∼55 at.% iron, come into contact with one another. The microstructure in deposits with such a composition is thought to consist primarily of columnar Fe_3O_4 crystals surrounded by Fe_2O_3, though further microstructural characterisation should be performed to confirm this. With conduction now forced through the oxide grains themselves, this structural development is also seen electrically as a significant increase in the resistance, and magnetically as a change of primary MR from AMR to GBMR. Due to the preferential formation of iron-oxide, as deposit stoichiometry approaches 1:1, towards that of Fe_3O_4 or Fe_2O_3, additional water vapour has no further effect.

A number of conclusions can be drawn from these results. Perhaps most interesting is the minimal influence of additional oxygen content in deposits containing a high percentage of iron. Although the substitution of metallic and magnetic iron for oxygen undoubtedly has an effect on both the resistivity and magnetisation of deposits, this influence was quite small for oxygen contents as high as 30 at.%. Even beyond this, although oxide formation induced a microstructural transformation, ferromagnetic behaviour remained simple and significant (figure 4.6d).

Towards the other compositional extreme, results were also very interesting. In agreement with the finding of Shimojo et al.[30] discussed in the beginning of this chapter, at rather high water

pressures very little carbon remained in deposits. Deposits produced under such conditions readily developed columnar crystalline iron oxide structures. With carbon also a significant contaminate in iron-rich deposits, further investigation of this process could prove advantageous. Furthermore, the suggestion of the presence of Fe_3O_4 is particularly exciting in regards to spintronic applications given the half metallic nature of this material. The addition of water vapour in this way could allow for the direct deposition of high purity crystalline Fe_3O_4 in all the ways and forms granted by the EBID technique.

Ultimately, in addition to these more fundamental conclusions, this systematic investigation has also further highlighted the significant flexibility of the EBID technique and particularly the $Fe_2(CO)_9$ precursor. With deposit microstructure ranging from polycrystalline iron to granular iron oxide, resistivities spanning more than three orders of magnitude and two forms of magnetoresistance arising, deposit properties can be tuned significantly simply via the addition of water vapour.

Chapter 5

Functional Magnetic Nanopillars

In this chapter an investigation of the growth and subsequent magnetic influence of nanoscale iron pillars produced by EBID is described. Unlike the wire deposits of the previous chapters, freestanding pillars make full use of the out-of-plane patterning ability of the EBID technique and being the simplest structure to do so, are ideal for an initial investigation. Furthermore, again in contrast to the more fundamental microwire characterisation, the work of this chapter is focused ultimately towards a magnetic application of such pillars.

A column of magnetic material effectively describes a bar magnet. Consequently, an iron pillar can be expected to possess north and south poles and thus emit magnetic stray fields. The influence of such stray fields on nearby magnetically sensitive materials represents a very simple and direct magnetic application of such pillars. It can be easily controlled by adjusting the position or size and shape of a deposit. One such application is the use of these pillars to influence domain wall motion in perpendicularly magnetised wires, and at the end of this chapter, preliminary experiments of this nature are presented as proof of this principle.

By their nature, pillars produced by EBID take a form determined predominantly by the character of the electron beam. For nano-magnetic applications, small but well shaped pillars with high iron content are required. Subsequently, in the first part of this chapter the influence of both the current and energy of the electron beam on pillar growth is discussed. In addition, a significant portion of this chapter explores beam induced heating phenomena in pillars, an effect found to have a major influence on both the content and shape of deposits.

In appendix A, the stability of such deposits is briefly reviewed.

5.1 Growth Dependencies

Achieving vertical growth with EBID is in itself trivial. The selective nature of the technique is such that in principle, the longer the electron beam irradiates a position, the more material is deposited at that position and thus the taller a deposit becomes. Such deposition is also simplified by the fact that many ordinarily important parameters relating to patterning (beam overlap, dwell time, see section 2.1.2) are in the case of pillars, generally* redundant. This leaves just the electron beam itself (and as always, the precursor) to determine the properties of deposits.

*In the case of non-continuous pillar deposition, dwell time remains important.

Naturally, the most straightforward variable on which pillar size can depend is the beam spot-size. It is known that in a SEM, due to the Gaussian form of the source emission, beam diameter tends to have a square root dependence on electron current.[57,58] Similarly, due to reduced electron-optical aberrations, spot size tends to decrease with increasing electron energy. Beyond such simple considerations though, due to the rather unusual nature of pillar deposition where growth extends significantly in the direction of the electron beam, certain aspects of the fundamental principles governing EBID (chapter 1) can change, particularly those relating to electron scattering processes.

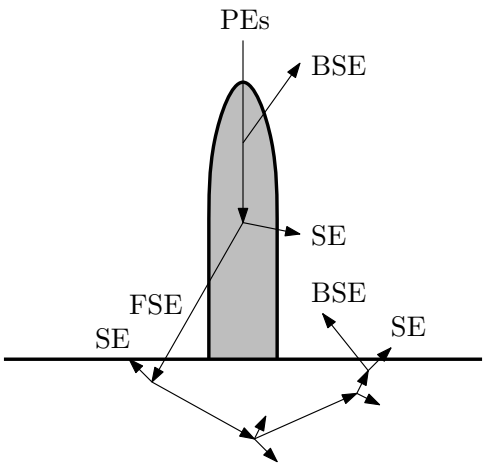

Figure 5.1: Electron scattering in a pillar. Due to the narrow geometry, electrons can readily leave the deposit, sometimes crossing the matter-vacuum interface numerous times. In tips longer than the BSE range scattering is confined to the pillar itself, however in shorter deposits, electrons can scatter forward (forward scattered electrons, FSE) into the substrate.

Compared to scattering in a flat substrate (or deposit) (figure 1.1a), electron scattering in a pillar is more complex, as depicted in figure 5.1. Electrons now impact a much smaller and isolated volume, and thus scatter through the deposit-vacuum interface much more readily. Depending on the length of the deposit (and energy of the electron beam), scattering can be entirely confined to the deposit or as illustrated in the figure, continue through into the substrate.

With this more complex scattering also comes more complex growth behaviour. Although for regular flat depositions, secondary electrons (SE) are thought to be primarily responsible for precursor dissociation, for pillar deposition, both primary (PE) and secondary electrons each seem to play an important role. Vertical growth is thought to be induced in large part by the electron beam directly (PEs), however, with pillar deposits consistently found to be broader than the beam used to create them,[59] side-scattered SEs are thought to be responsible for an additional radial growth process.[60] Such reasoning is found to agree with observations, and has in fact already been experimentally applied to deposit extremely small features. By stopping irradiation before pillars have a chance to form sidewalls and thus expand laterally, nanodots as small as 1 nm (the diameter of the electron beam used) have been successfully produced in this way.[61] Also, by growing pillars sideways from an edge (lateral deposition) and thereby minimising PE interaction and SE creation, deposit diameters have been successfully reduced by an order of magnitude, from 50 to 5 nm.[62]

As a pillar increases in length and the electron interaction volume becomes increasingly separated from the substrate, some unique effects can arise. Both charge[63] and heat[64] buildup can occur, each able to significantly influence growth. This concept of beam induced heating was

discussed by Schoenaker[34], and is thought to partially explain the positive dependence of iron content on beam current. A local temperature increase induced by a high power electron beam can aid precursor dissociation and thus deposition. Such effects can be considerably enhanced in thermally isolated pillar structures and subsequently, commonly represents an additional source of radial growth.

With the above in mind, in the following two subsections the current and energy dependencies of pillars deposited using the $Fe_2(CO)_9$ precursor are discussed. The goal of these investigations is to optimise deposition parameters to eventually allow the deposition of nanoscale magnetic deposits. In order to truly reach the nanoscale, dimensions need to be below 100 nm. Also, although it is not completely clear when ferromagnetic behaviour will cease, from the work of Schoenaker[34] and of the previous chapter, it appears safe to assume that a deposit containing at least 60 at.% iron will be magnetic.

5.1.1 Beam Current

As just discussed, while increasing the electron beam current can lead to larger deposit diameters, it can also help increase the purity of deposits.[34] The goal here is thus to explore this relation, and ultimately determine how these parameters can best be balanced in order to maximise iron content while keeping deposits as small as possible.

To help minimise deposit size, the ultra high resolution (UHR) immersion lens mode of the dualbeam (described in section 2.1.1) was primarily utilised for pillar deposition. The strong axial magnetic field used in this mode is expected to influence scattering, particularly that of the low energy SEs, confining them near the axis and thereby influencing the deposition process. Furthermore, with pillars of magnetic iron being deposited, this field is also hoped to help magnetise pillars along their axis.

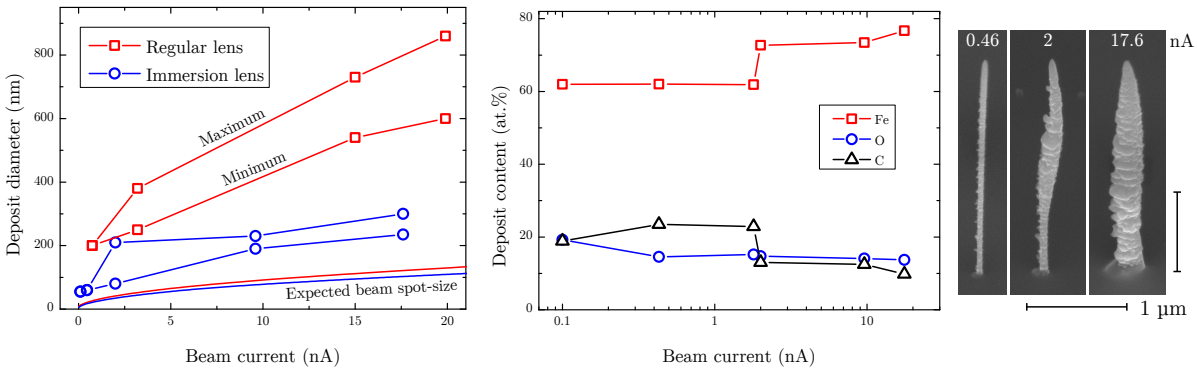

(a) (b) (c)

Figure 5.2: The influence of electron beam current on pillar size and composition (all deposits made with a beam energy of 5 keV). **(a)** Pillar diameter as a function of beam current in both regular (red) and immersion (blue) modes. For non-uniform deposits, both the minimum and maximum diameters are presented as indicated. Theoretical beam spot-sizes are also included for comparison. **(b)** Pillar composition as a function of beam current for immersion mode deposits. **(c)** SEM images of three pillars produced at different currents in immersion mode (viewed 52° from the normal, hence the different horizontal and vertical scales).

Using 5 keV beam energy as a starting point, a number of pillars were deposited with various beam currents using the immersion lens. The results are shown in figure 5.2.

Figure figure 5.2a shows the diameter of pillar deposits as a function of electron beam current.

To illustrate the resolution gained by using the immersion lens, deposits produced with the regular lens are also included. It is clear that pillars get wider as beam current is increased. More interestingly though, as indicated by the diverging lines showing minimum and maximum diameters, above a current of a few nanoamperes, pillars take on an irregular form (see figure 5.2c). Figure figure 5.2b shows how pillar composition changes as a function of current. The transition to non-constant diameters at currents above approximately 2 nA is also very clear in the composition. There appear to exist two separate compositional regimes for low and high currents. At high beam currents, high (>70 at.%) and relatively stable iron content is found. Below a critical current of a few nanoamperes however, iron content drops off to a (second) compositional plateau at around 60 at.%.

These results are consistent with a thermally assisted radial growth process. At currents above around 2 nA, energy deposition by the electron beam is sufficient to increase the temperature of the pillar deposit and thereby aid precursor dissociation, leading not only to increased iron content but also to broader pillars. (This high current thermal phenomenon is investigated in detail in section 5.2).

From these results, it is clear that to truly reach the nanoscale (pillar diameter, ø < 100 nm), this thermal effect needs to be avoided and a beam current of below 2 nA (and the immersion lens) must be used. Although deposits with currents below 100 pA were not produced or investigated, any possible gains in resolution in this current range are expected to be minimal, and eventually iron content will drop off. In conclusion, beam currents around 0.1 to 0.5 nA producing pillars with an acceptable iron content of around 62 at.% and respective diameters of approximately 55 and 70 nm, are most suitable for nanomagnetic applications.

5.1.2 Beam Energy

For flat deposits, beam energy has a rather straightforward influence on deposition efficiency. Due to increasing penetration depths and decreasing SE yield,[4] deposit purity decreases with increasing energy.[34] Also, as was mentioned earlier, decreased optical aberrations decrease beam spot size with increasing electron energy. It is the aim here to see how these and possibly other effects translate to the size and content of pillar deposits.

To investigate this relationship, a number of pillars were deposited with a constant beam current of 0.1 nA (in light of previous findings), and acceleration voltages of 2, 5, 10 and 18 kV in the immersion lens mode. The results are displayed in figure 5.3.

As can be seen in figure 5.3b, both the diameter and the iron content of pillars decreases with increasing beam energy. The dualbeam software suggests that the spot size of the electron beam will decrease exponentially with increasing energies. Displaying a similar trend, the observed decrease in pillar diameter is expected to be a result of this theoretical constraint. The cause of the reduction in iron content is less clear. A number of deposits were investigated at each energy in order to avoid small variations caused by a badly focused or astigmatic beam. Even so, given the expected 3 at.% accuracy of EDX, this very slight decrease in composition must be considered with caution. One possible explanation is suggested by the volume of material deposited. In spite of generally taller pillars, deposited volume was found to decrease with increasing energy (not shown). This suggests that precursor dissociation efficiency, which is often associated with deposit purity, also decreased with energy. Although always significant in the tall and narrow geometries of pillar depositions (figure 5.1), it is reasonable to expected that at higher energies, a larger number of PEs will scatter out of the pillar before depositing all their energy. Though not universal, a decrease in growth rate with increasing electron energy

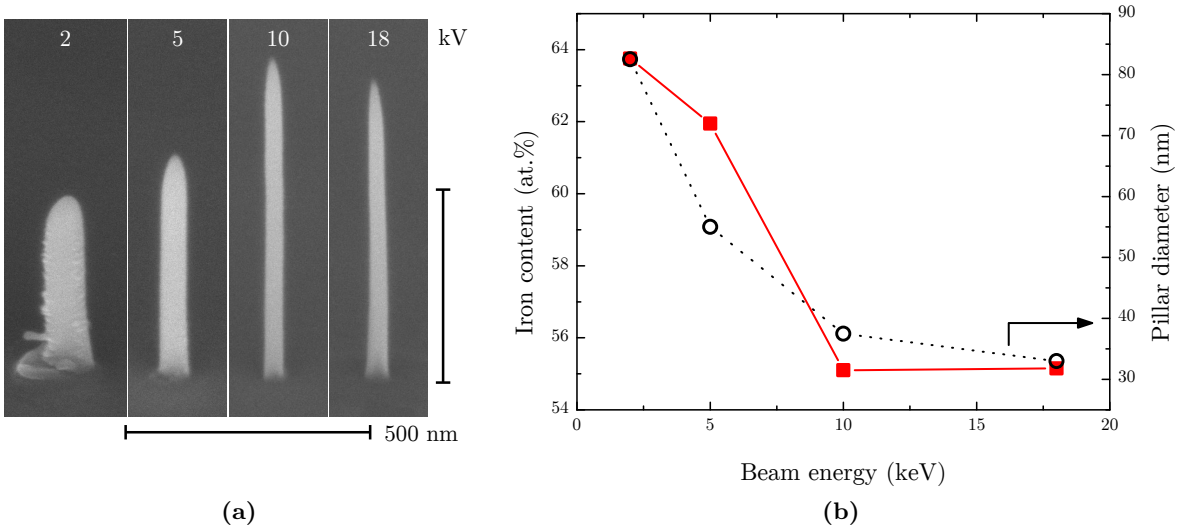

Figure 5.3: **(a)** SEM images of four pillars produced at a constant beam current of 100 pA but various energies (indicated) in immersion mode (viewed 52° from the normal). **(b)** Pillar diameter (circles) and iron content (squares) as a function of beam energy. EDX determined composition has an absolute uncertainty of ∼3 at.%, not shown.

is frequently reported in literature.[58,59]

In conclusion, although smaller pillar dimensions are made possible with higher beam energies, this comes at the expense of iron content. In this regard, an energy of 5 kV provides a reasonable compromise, producing pillars with diameters approaching just 50 nm while maintaining iron content above 60 at.%. Although far from an exhaustive study, for EBID of iron pillars from $Fe_2(CO)_9$ at the nanoscale, both low currents (100s pA) and rather low acceleration voltages (5 keV) have been determined to be most optimal.

Before putting these conclusions into practise (section 5.3), in the next section the beam induced heating effects that were observed when depositing at high beam currents are further investigated via a computational model.

5.2 Beam Induced Heating

As has already been discussed, lateral pillar growth can be caused by two different processes: electron-induced precursor dissociation at the pillar walls by side-scattering and thermally assisted precursor dissociation resulting from beam induced heating. In this section, stimulated by the appearance of some very unusual pillar growth, shown in figure 5.4, and the results of subsection 5.1.1, this thermal effect is investigated further. First qualitatively discussed, later in this section a computer simulation is developed to enable a more quantitative analysis of this phenomenon.

Pyrolytic deposition processes (such as CVD) are capable of producing very pure material. Consequently, in addition to the fundamental motive to explain observations, a better understanding of this effect may also yield practical advantages.

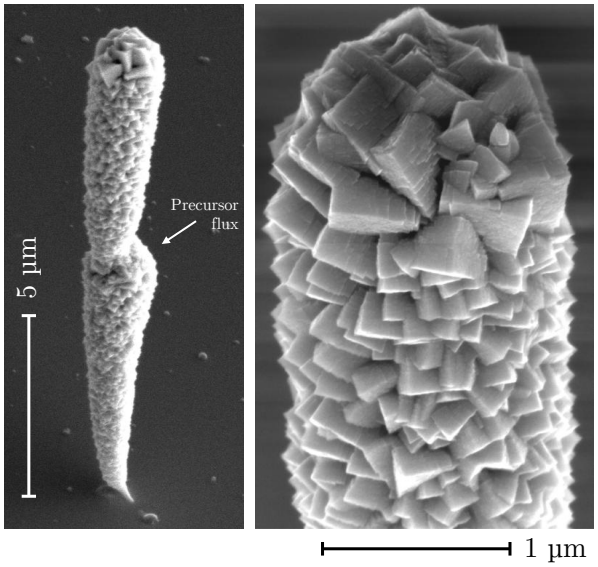

Figure 5.4: A large pillar exhibiting unusual crystalline growth. Deposited over three minutes using a 5 keV, 17.7 nA electron beam in immersion mode.

When depositing pillars in the immersion lens mode at very high electron beam currents (∼20 nA) for extended periods, very unusual growth was observed as shown in figure 5.4. In addition to crystalline growth biased towards the precursor flow, these large deposits possessed an apparent double structure situated on a very small base. Remarkably similar growth was observed by Hochleitner et al.[65] using $Fe(CO)_5$. In addition, this general character, a segmented radial growth, has also been observed in cobalt[21,66] and tungsten[67] EBID pillars. As will be explained, such growth can be attributed to beam induced heating.

Although crystallographic analysis could not be performed on the above deposit itself, there are indications that the crystalline growth may represent bcc iron. The feasibility of obtaining crystalline iron as a result of beam induced heating was successfully confirmed by considering an extreme case. The centre of a very thin and thus thermally insulating membrane film (a TEM membrane, 20 nm thick) was irradiated with a high current electron beam. As well as bearing a remarkable resemblance to the pillar surface, the resulting deposition was confirmed with electron diffraction to consist primarily of bcc iron (see appendix B). Secondly, and perhaps more convincingly, electron diffraction was also performed by Hochleitner et al.[65]. Although measurements on the most comparable deposits were not presented, bcc iron was identified in the dendritic radial growth of not-dissimilar pillars. Although crystalline, surprisingly, EDX

spectroscopy revealed a rather ordinary iron content of 75 at.%. Although this will be a bulk average of the entire pillar, a higher-than-normal content is still to be expected given the presence of at least some bcc iron. This is similar to what was found for the polycrystalline microwire deposits discussed in chapter 3.

In an attempt to better understand the observed growth process, the evolution of such a pillar with time has been studied. Using the same high current electron beam, a number of pillars were produced for different deposition times. As figure 5.5 shows, a very particular growth behaviour occurs. As the pillars extend vertically, an apparently cyclic radial expansion takes place. A pillar initially just grows in length (0-20 s) but subsequently also broadens radially to a certain size (30-60 s), then continues just to lengthen (120 s) before again also broadening (180 s).

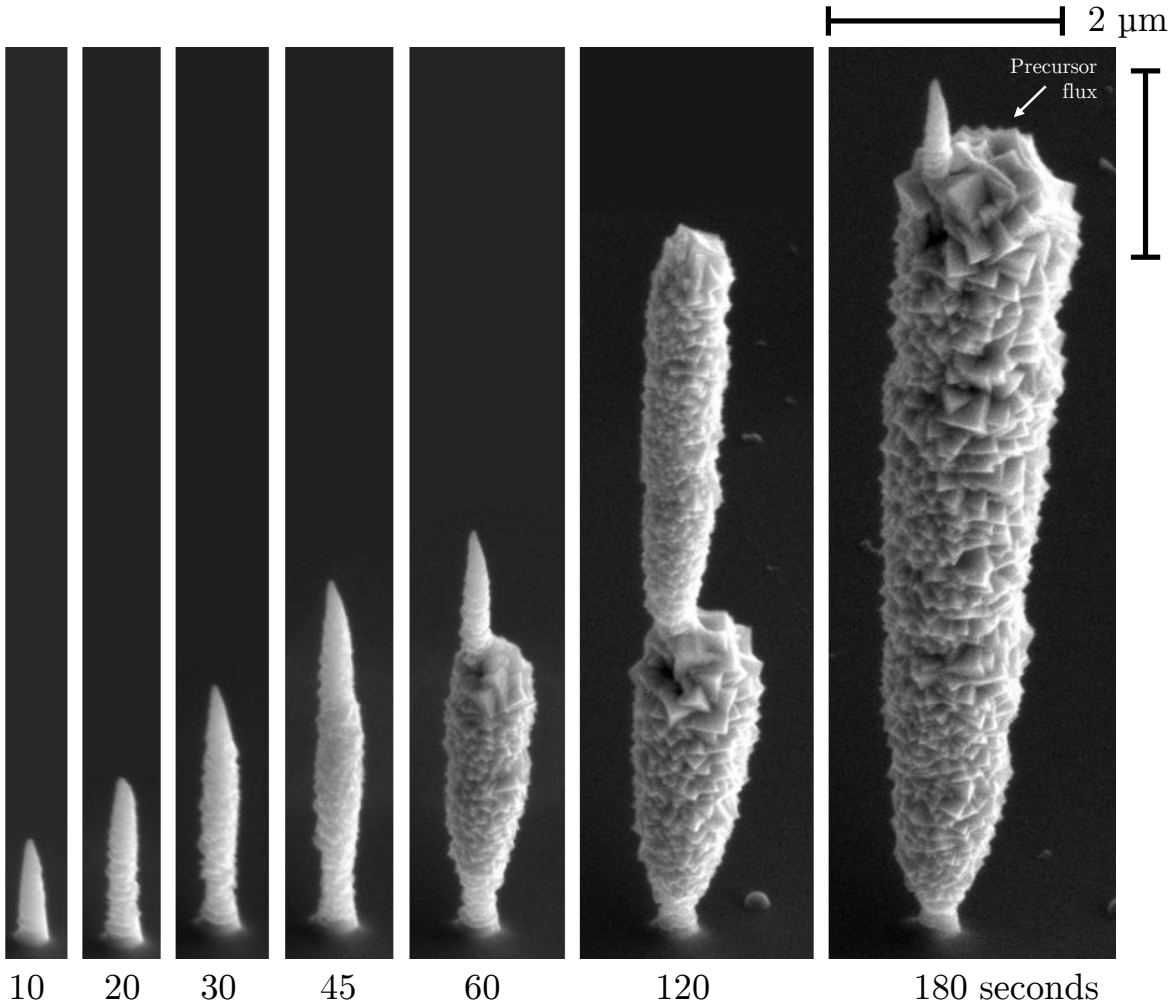

Figure 5.5: SEM images of a number of pillars deposited over different times. (viewed 52° from the normal). The pillars were deposited using a 5 keV, 18 nA beam in the immersion lens mode. The position of the GIS needle and hence precursor flux is indicated. All images at the same scale.

This unusual growth was directly observable in variation in the specimen current, the current measured flowing through the substrate due to incident electrons. Pillar growth (vertically) was readily identifiable as a gradual decrease in this electron current caused by increased scattering away from the substrate, off, and out of the sharp tip. In contrast, radial growth was characterised by a increase in this current as fewer electrons escaped the sides of the now wider

deposit.

As with the deposit depicted in figure 5.4, here again the radial growth of the larger pillars is seen to be biased towards the precursor flux (indicated with an arrow in the figure). This is not surprising given the large diameter of these deposits (ø > 1 µm) and is likely a shadowing effect.[66] The large volume of some of these deposits also means precursor pressure will play a very important role. With an estimated volume of 30 µm^3, the largest of these deposits (180 s) was produced an order of magnitude faster than typically achieved for in-plane depositions. Such pillars could only be produced when the precursor pressure was high ($> 5\times10^{-6}$ mbar).

As will be discussed in the following subsection, this behaviour is thought to be the combined result of a catalytic effect of iron[40] and beam induced heating.

5.2.1 A Qualitative Description

Before attempting to explain this growth, some simple assumptions are made relating to heat conduction in such pillars. Firstly, heat flow is assumed to follow Fourier's Law of thermal conduction which states that heat flux through a surface (ϕ) is proportional to the (negative) temperature gradient across that surface, i.e.

$$\phi \propto -\nabla T. \tag{5.1}$$

Secondly, it is assumed that the substrate on which a pillar is deposited acts as a heat sink, preventing the pillar base from heating up to any significant degree. With this in mind and with the help of figure 5.6, the unusual growth portrayed in figure 5.5 can be explained in terms of two distinct growth phases.

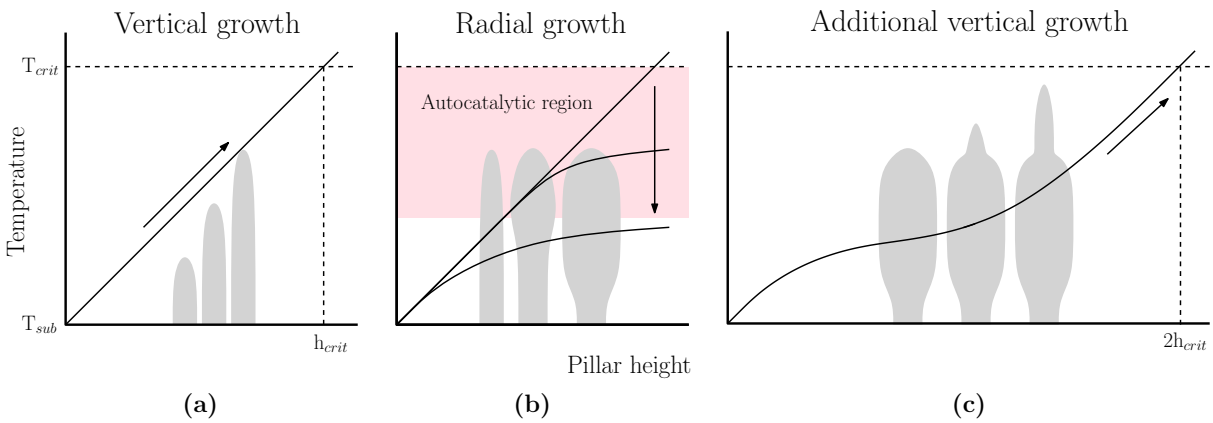

Figure 5.6: Expected temperature profiles for pillar deposits in the different growth phases. Lines represent the varying temperature along the length of a pillar and arrows, pillar growth. Silhouettes of the type of pillar growth described in each graph are shown in the background. The overall process is discussed in the text.

Regular vertical growth: Growth begins as normal. Electrons alone are responsible for precursor dissociation and growth is primarily vertical. As illustrated in figure 5.6a, with both the cross sectional area of the pillar and the incident heat flux provided by the electron beam constant, this causes the temperature of the tip of the pillar to increase. In figure 5.5, this first phase of growth can be seen at deposition times of 10 to just before 45 s. Eventually, at some characteristic height h_{crit} (around 3 µm in this case), the tip reaches a temperature, T_{crit}, sufficient to induce thermally assisted precursor decomposition. This marks the beginning of the second phase of growth.

Thermally induced autocatalytic radial growth: Upon reaching T_{crit} a second deposition mechanism arises. Due to the increased thermal energy, the precursor can now dissociate much easier, possibly even spontaneously. The increased temperature combined with the sudden increase in precursor decomposition leads to crystalline growth all around the hot tip. The previous vertical growth becomes suppressed slightly, likely due to the sudden decrease in precursor availability. As shown in figure 5.6b, the broadening of the tip cause the heat flux through it to also decrease, ultimately lowering the temperature. However, in what is thought to be an autocatalytic effect[10,20,21,65] the presence of the crystalline iron allows further thermally assisted crystalline growth to progress towards the bottom of the pillar where temperatures are sub-critical ($< T_{crit}$) (indicated by the shaded region in figure 5.6b). The additional broadening induced by this autocatalytic growth further reduces the temperature gradient and ultimately, ends the radial growth phase. This second phase of growth is first apparent at a deposition time of 60 s in figure 5.5. It is clear that further down the pillar this radial growth is less efficient, yielding less material and smaller crystals.

As seen at 120 s in figure 5.5 and indicated by figure 5.6c, once the autocatalytic growth ceases, ordinary vertical growth can continue as usual. Eventually the whole process can repeat itself.

5.2.2 Semi-Quantitative Simulations

To give some quantitative weight to the previous mostly qualitative explantation of the growth process observed in figure 5.5, a simple semi-quantitative computational model has been developed.

There have been numerous attempts to model beam induced heating phenomenon. Both simple analytical considerations[3,24,66,68] and more comprehensive computational simulations[64,69,70] have been applied. In both cases, two things need to be determined. Firstly, given the possibility of electron scattering, the proportion of the beam energy that is actually deposited into a pillar must be determined. Secondly, given such energy deposition, heat flow and resulting temperature gradients must be deduced. While this first point is generally achievable, either from stopping distance calculations or scattering simulations, modelling the heat flow through the deposit can be more difficult, due primarily to a lack of knowledge of the thermal conductivity.

Estimates of the thermal conductivity (κ) of carbon/metal nanocomposites, of which depositions commonly consist, can range from polymers (0.01 W/Km for PMMA) to pure metals (395 W/Km for copper).[3] As a result, modelled beam induced temperature increases under otherwise identical conditions can range from tens[24,64] to just fractions of a degree.[69] There is still some disagreement as to the significance of beam induced heating in EBID, and this uncertainty of κ is thought to be largely the reason why. The aim here is to work backwards. By modelling two situations, one in which thermally assisted growth is clearly apparent and the other in which it is not, a value of κ can be predicted. Based on how realistic this prediction is, a thermal influence can either be confirmed or disproved.

Following a similar approach to Randolph et al.[64], simulations have been carried out in two phases. First, using Monte Carlo methods, numerous electron scattering trajectories are simulated to determine how much of (and where) the energy of the beam is deposited in the pillar. Next, using this energy distribution as a source term, the heat transport equation is solved using finite element methods (FEM), enabling temperature gradients to be determined. Details can be found in appendix C.

The two pillar geometries produced at deposition times of 45 and 60 seconds in figure 5.5

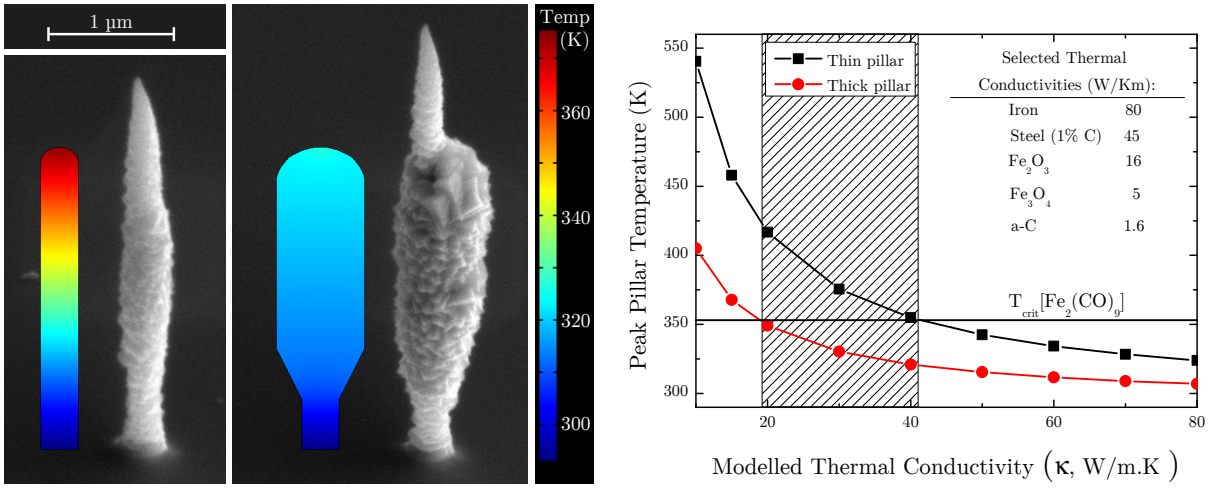

(a) **(b)**

Figure 5.7: Results from the electron scattering (5 keV, 18 nA) and heat flow simulations in two pillar geometries. **(a)** SEM images (52° from the normal) and corresponding modelled volumes of the pillars used for the simulations. The model pillars are coloured corresponding to the temperature gradient predicted when simulating a thermal conductivity of 30 W/m·K. **(b)** Simulated maximum pillar temperature as a function of κ for both pillar geometries. The thermal decomposition temperature of $Fe_2(CO)_9$ (80 °C) is indicated. The shaded region subsequently describes values of κ which agree with a thermally induced growth theory. For comparison, κ values for a number of other relevant materials are also listed.[42,71]

have been modelled, as can be seen in figure 5.7a. These two cases respectively represent the beginning and end of the radial growth phase and were modelled as hemispherically-capped cylindrical-like volumes approximately 3 µm high and 300 and 700 nm wide (maximum). From EDX measurements on the deposits (73-14-13 at.%, Fe-O-C), the atomic number (Z) and atomic weight (A) of the pillars were estimated by taking simple averages. Total density, ρ, was also estimated by averaging, using the densities of crystalline iron (7.874 g/cm^3), amorphous carbon (2 g/cm^3), and averaging the oxygen density as it exists in Fe_2O_3 and Fe_3O_4 ($(3.33 + 2)/2 = 2.67$ g/cm^3) (values from reference 42). Electron scattering simulations were carried out with 12,500 5 keV electrons, coming from a Gaussian beam with a 100 nm FWHM diameter (predicted by the dualbeam software). The energy distribution produced by this scattering was converted into a power distribution assuming a 18 nA beam current. The same simulations were carried out for both pillar models. Thermal modelling was carried out as a function of the thermal conductivity. κ was varied from 10, near that of thermally insulating crystalline iron oxide,[71] to 80, that of metallic iron.[42] The final results are shown in figure 5.7.

The temperature profiles calculated for the case of $\kappa = 30$ are shown in figure 5.7a. It is clear that there is a significant difference in temperature between thin and thick pillars. More significantly though, in figure 5.7b the peak temperatures of both pillar geometries as a function of κ is shown. To help interpretation, the expected decomposition temperature of the $Fe_2(CO)_9$ precursor is indicated as the solid horizontal line. Although the $Fe_2(CO)_9$ molecule is not well explored in literature a small number of publications do suggest that it will thermally decompose at temperatures as low as 80 °C.[18,72] This was also confirmed by Schoenaker[34]. Considering the previously described growth process, for heat induced decomposition to be confirmed, the maximum temperature of the thin pillar must be above 80 °C. Then after the pillar has expanded radially, this temperature must drop below this line. As indicated by the shaded region in the figure, this scenario is indeed possible for thermal conductivities of between approximately 20 and 40 W/m·K.

A κ of around 30 W/m·K is neither unbelievably low nor high. To better put this value into perspective the thermal conductivity of a number of relevant material are also listed in figure 5.7b. Microstructure has a major influence on thermal conductivity and thus with pillars expected to be predominately amorphous, a κ anywhere near that of pure iron cannot be expected. At the same time though, deposits do still contain a significant proportion of iron which should similarly prevent a very low value. This result confirms that heat played a part in producing the unusual growth behaviour illustrated in figure 5.5.

5.2.3 Concluding Discussion

It is clear that heating induced by the electron beam does play an important role in the deposition of freestanding structures using the $Fe_2(CO)_9$ precursor. The unusual growth observed when depositing with high beam currents (figure 5.5) can be qualitatively well explained. A degree of quantitative agreement has also been achieved. Although the rather average iron content of these deposits (75 at.%) might suggest otherwise, the development of what appears to be bcc iron and a very high deposit yields do reinforce the idea that this growth is the result of an additional precursor decomposition mechanism, in addition to the electrons. In particular, this crystalline pillar growth is thought to represent the most extreme influence that beam induced heating can have, causing temperature rises sufficient to actually spontaneously decompose the precursor thermally.

In terms of the diameter and iron content increases observed in subsection 5.1.1 (figure 5.2), a less extreme version of this effect is expected to be responsible, specifically heat *assisted* precursor decomposition, for which electron induced dissociation is still required. With changes apparent at currents of just a few nanoamperes it is unlikely that critical temperatures (T_{crit}) will be reached. Unlike the crystalline growth, the appearance of the radial growth observed here is quite different. Best illustrated by the high current deposit presented in figure 5.2c, it appears layered and platelet-like. It is as though conical 'caps' have been constantly re-deposited on top of one another. Such growth is thought to be caused by forward scattering electrons as they pass through the pillar wall.[73] It is possible that increased temperatures allows previously ineffective electrons scattering in this way to subsequently decompose the precursor. Another possibility is that such increased temperatures alter precursor adsorption behaviour, possibly in towards the pillar walls. Autocatalysis could also still play a role.

What is interesting about these previous results is the compositional change. In the deposits exhibiting crystalline growth composition was effectively constant at 75 at.%. The onset of thermal effects at lower currents however clearly had a positive influence on the composition. This could suggests the presence of a fundamental limitation. It is possible that the vacuum or even the precursor itself is not suitable for depositions higher than around 75 at.% iron.

As seen in figure 5.8, similar time dependent experiments were performed using the regular lens mode. Even when using equally high currents, the strange growth of figure 5.5 could not be reproduced. Although the appearance of the just described platelet growth does indicate that temperature had some effect, with deposits much broader, it is likely temperatures simply could not get high enough to thermally dissociate the precursor.

One final observation of note is the appearance of a slight roughening of pillar surfaces (see the 0.46 nA deposit in figure 5.2c). Such roughening is often reported, for EBID[74] as well as IBID,[75,76] and while the exact cause is not completely clear, the rather uniform appearance of the growth along the height of pillar depositions suggests it is not thermally induced. The effect is enhanced at high precursor pressures,[76] however, both the use of insulating substrates[75] and

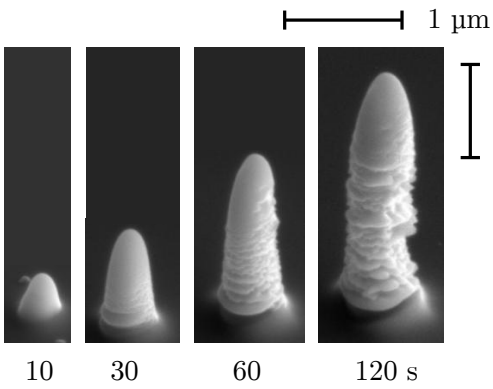

Figure 5.8: SEM images (viewed 52° from the normal) of a number of pillars deposited over different times (as indicated). The pillars were deposited using a 5 keV, 18 nA beam in the regular lens mode.

high (> 5 kV) beam energies[74] reduces the growth. One reasonable explanation suggests that this irregular structure is the result of surface deposition induced by secondary electrons emitted from the pillar sidewalls,[75] an effect somewhat similar to the previously described scattering leading to the platelet growth, but now at low currents. Given its manifestation in small, low current deposits, of the effects discussed here this is perhaps the most important with regards to the rest of the work in this chapter. However, with no definitive cause determined, prevention remains difficult.

A great deal has already been learnt from these investigations, but there is still a lot of potential for further investigations of this nature. One parameter not yet investigated is beam energy, and its influence on these thermal effects. The exact nature of the catalytic growth process is also not yet well understood. The simulation program developed also still has significant potential. Ultimately, it should be possible to use such simulations to predict whether such thermal effects will or will not occur for a given electron beam and deposit geometry. There is also the possibility to use such thermal effects to anneal already deposited samples *in situ*. By irradiating a deposited nanopillar with a high energy beam without applying a precursor, both structure and purities may be able to be increased.

5.3 Preliminary Application: Influencing Domain Wall Motion

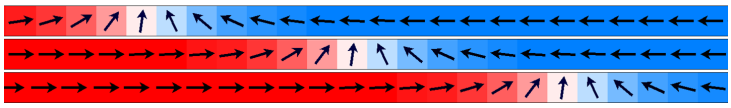

Figure 5.9: A conceptual illustration of domain wall motion. The red and blue regions represent two domains (the arrows the direction of local magnetisation). As one increases and the other decreases in size, the interface between them moves.

Domain wall motion (DWM), the coherent transport of magnetic domains, is currently the subject of substantial scientific research, due in no small part to its potential application to next-generation data storage and processing technologies. Among others, this is one of the fields of research which could benefit greatly from magnetic EBID techniques and it is for this reason that such experiments have been chosen as part of a preliminary study of the magnetic influence of EBID iron nanopillars.

Magnetically, data is always encoded in essentially the same way, as magnetic domains of differing polarity. What does vary however, is the dynamics, the methods by which such magnetic data is transported for access and eventual manipulation. In a hard-disk drive, a modern magnetic storage device, data access involves a lot of mechanical movement. Both the read-write head as well as the disk on which the data sits must move, leading to inherent drawbacks such as long access times and an increase susceptibility to failure. Ideally, data needs to be accessible without the need for such movement, which is where domain wall motion enters; if the magnetic domains describing the data could themselves be coherently moved, the need for moving parts would be eliminated. The key here though, is to achieve such transport without altering or destroying the domains.

Two domain wall transport mechanisms are currently being explored. The first, and most straightforward method to move a domain wall is to use a magnetic field. A second method, more recently discovered and also perhaps more promising, utilises a so called *spin-torque effect* and involves using very large currents to literally push domain walls with electrons. Beyond a fundamental transport mechanism, both approaches also need to make use of additional tricks to ensure data can be appropriately controlled. This is particularly important for field driven DWM, since ordinarily, the application of a magnetic field will simply grow domains of one polarisation at the expense of another, thereby destroying information.

To this end, an almost universal simplification which is applied to grant better control is the restriction of motion to one dimension via the use of (nanoscale) wires. Additional control can be achieved through the manipulation of the energy landscape of the domain walls. Such manipulation has already been successfully achieved using a variety of techniques. These include geometrical alterations (notches and bends),[77] material modifications (Ga^+ radiation),[78] and the deposition of external magnetic structures.[79]

EBID of magnetic materials represents a particularly useful addition to these current possibilities. The one-step, three dimensional, nanoscale nature of the technique makes it ideal for research of this nature. In this section a very simple implementation of this principle is demonstrated: iron pillars are deposited on top of magnetic wires and the influence of their stray fields on DWM is observed. As well as illustrating the practical merits of EBID in such applications, such experiments also provide a straightforward, though indirect, method to qualitatively investigate the ferromagnetic character of such pillar deposits, something which, due both to their small size and orientation, is otherwise not trivially done.

After first considering how best to carry out such an investigation, towards the end of this chapter the results of a pilot experiment are presented.

5.3.1 Experimental Considerations

When a vertical pillar is deposited on a flat substrate, the resulting stray field penetrating the surface will be strongest along the pillar axis. In contrast, a very thin (10s of nm) magnetic nanowire, suitable for domain wall motion experimentation (for example, permalloy) will generally have a magnetisation aligned in-plane, perpendicular to the field of the pillar. Although the magnetisation of a domain wall itself can often be very complex, even partially out of plane, this situation is not ideal. Fortunately however, perpendicularly magnetised materials are also of interest for DWM.

When layered periodically, certain magnetic/non-magnetic material combinations can exhibit unusual magnetic properties, most notably, a very large perpendicular magnetic anisotropy. Thought to be a result of interface effects,[78] these properties tend to be strongest for very thin (sub-nm) layers. The very high anisotropy in these materials tends to produce domain walls that are both simple and narrow, two features beneficial for domain wall dynamics. While simplicity will be key both to the stability and reproducibility of domains in eventual memory devices, smaller domain walls will also ultimately allow for higher data densities.

A popular multilayer system of this nature is Co/Pt,[80] and it is such a system, specifically a trilayer of Pt(4 nm)-Co(0.6 nm)-Pt(2 nm), which is utilised here. By depositing an iron pillar on top of a narrow wire of such a multilayer, its stray field can be made to penetrate the wire. This penetrating stray field essentially couples the magnetisation of a small region of the wire under the pillar to the magnetisation of the pillar itself. Essentially, a pillar acts to increase the perpendicular anisotropy in the wire underneath it. In order for a domain wall to subsequently pass through this region, either the coupling must be overcome or the pillar must also be switched. A practical implementation of this idea is illustrated in figure 5.10. With a pillar grown on top of a wire, **(i)** first the entire construction must be saturated to ensure the pillar and wire are pointing in the same direction. **(ii)** Next a domain wall must be nucleated and by applying a small opposite field, made to approach the pillar. **(iii)** If the pillar is indeed magnetic, and magnetised opposite to the approaching domain, the wall motion should be retarded. **(iv)** To overcome this pinning the applied field will need to be increased to switch the magnetisation of the pillar itself.

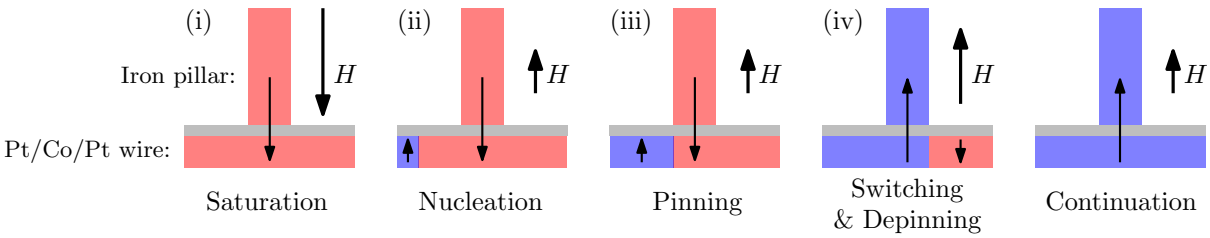

Figure 5.10: A schematic profile view of a magnetic iron pillar on top of a perpendicularly magnetised wire. A magnetic field (H) is used to attempt to move a domain wall in the wire past the stray field of the pillar. Further discussed in the text.

As mentioned earlier, domain walls can be influenced in a number of different ways, from material to geometric variations. For this reason, the observation of pinning alone is insufficient to prove a specific magnetic effect. To better characterise the nature of the pinning, further investigation is required. Essentially, a domain wall can be pinned in one of two ways. As

illustrated by figure 5.11, it can either be blocked by an energy barrier or trapped in an energy well. By reducing the width over which a domain wall can form, a notch in a wire typically represents an energy well.[77] In contrast, a protrusion has been found to represent a barrier surrounded by two smaller wells.[81] The electrostatic influence of the magnetic pillar however, is expected to be intrinsically repulsive. Provided the pillar reverses its magnetisation as the domain wall passes, it should behave just like simple energy barrier. As also illustrated in figure 5.11, experimentally testing whether pinning is due to a well or a barrier (or a combination) is relatively straightforward. If a domain wall can be brought towards and away from a pillar without getting 'stuck', then this is an indication that the pinning is magnetic in nature.

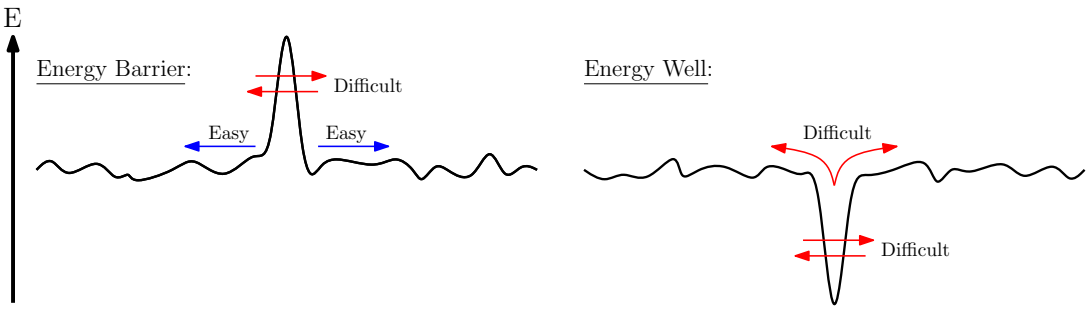

Figure 5.11: The two fundamental energy landscape distortions influencing DWM, a barrier and a well. As indicated, although both represent an obstacle, the trapping effect of a well allows the two to be distinguished experimentally by attempting to approach and retract a domain wall. A general roughness of the landscape is induced by material defects and/or thermal fluctuations.

Pinning Dependencies

One step further than simply achieving a magnetic influence with a magnetic pillar is controlling the influence. There are essentially two ways to achieve such control, by changing the strength or form of the magnetic stray field or by changing the switching behaviour of the pillars. Here, both these parameters are briefly investigated with computational modelling.

A magnetic pillar essentially represents a dipole and thus produces a rather simple stray field. Using the software package COMSOL,[82] the stray field produced by a 1 µm long, 60 nm wide magnetic cylinder of pure iron ($M_s \simeq 1700$ kA/m) has been modelled. The result can be seen in figure 5.12a. The inverse-cubed decrease in field strength with distance, characteristic of a dipole, is evident. It is subsequently clear that with the Pt/Co/Pt multilayers only a few nanometres thick, under ideal circumstances at least, the range of the stray field of a pillar will not be an issue in these experiments. Although the permeability of the Pt/Co/Pt wires will have some influence, controlling the form of the stray field from a simple cylindrical pillar is difficult. The magnitude however, is more feasible. As well as simply depositing a pillar further away from the wire, the magnetisation of the pillar itself will control the strength of this field. In terms of EBID iron pillars, the saturation magnetisation was previously found to scale with iron content.[34] This implies that the strength of the stray field also simply scales linearly with iron content. Although a linear relation is likely an oversimplification, since the influence of on-magnetic material is disregarded completely, this does theoretically at least, provide a rather straightforward way to control the magnetic pinning strength of a pillar.

Although the properties of the stray field do have some influence on the magnetic pinning ability of a pillar, with depinning determined by the field at which the pillar switches its magnetisation, it is ultimately the coercive field which is of most concern. Using the (2-D) macromagnetic simulation software OOMMF,[83] the switching of a magnetic pillar, specifically the dependence

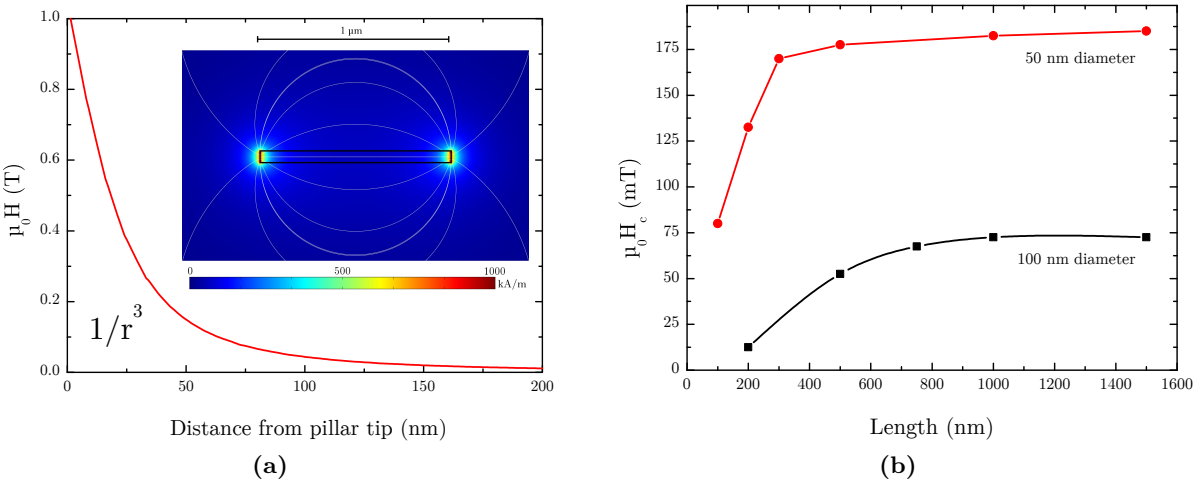

Figure 5.12: **(a)** The simulated stray field emerging from the tip of a pure iron ($M_s \simeq 1700$ kA/m) nanopillar (dipole) 1 µm by 60 nm in size. (inset) A visualisation of the entire stray field of the pillar. **(b)** Simulated coercive fields of different sized nanopillars, for a magnetisation of 1000 kA/m corresponding to 60 at.% iron.

of such switching on geometry, has also been briefly investigated. A simple rectangular geometry was modelled for a magnetisation of 1000 kA/m (corresponding to 60 at.% iron) and considering only shape anisotropy. The field required to longitudinally switch the magnetic body was investigated as a function of its dimensions. Two different widths (diameters) were simulated for various lengths, as shown in figure 5.12b. Provided the aspect ratio of a pillar was sufficiently high (>10), length was found to have a minor influence on H_c. Width, however, had a large effect, with thicker pillars switching much more readily. Although not of interest quantitatively, qualitatively these results are informative: provided pillars are thin, their length is of lesser concern.

In the following subsection, these findings are put into practise in the form of a pilot experiment.

5.3.2 Pilot Experiment

Note: *Towards the end of this project, in the time between the optimisation study of section 5.1 and this preliminary application investigation, the $Fe_2(CO)_9$ precursor ran out and was refilled. For reasons not yet understood, subsequent deposits were found to contain significantly more oxygen and previous results, namely very high iron contents, could not be reproduced. Maximum achievable iron content was reduced from 80 to 60 at.%. Repeating the optimisation investigations was not feasible, however brief measurements of some test pillars deposited at 0.1 nA revealed that iron content had dropped to less than 50 at.%, with the remainder consisting primarily of oxygen (40 at.%) and a small amount of carbon (10 at.%). The form of these pillar deposits was unaffected.*

Finally in this chapter the results of a small pilot experiment are discussed. A small number of EBID iron pillars were deposited onto Pt/Co/Pt wires to explore their influence on DWM.

In line with the conclusions of section 5.1, all pillars were deposited in the immersion lens mode using a 5 keV beam. Two sets of pillars were produced using two different beam currents; the first at 0.41 nA and the second, 0.1 nA. While keeping dimensions in the nanoscale, the use of these two different currents enabled pillar diameter to be varied. Each set consisted of three

deposits of different heights (1, 2 or 3 minute depositions), having both low and high aspect ratios.

The two sets were deposited onto two separate Pt(4 nm)-Co(0.6 nm)-Pt(2 nm) wires. The wires were patterned onto a Si-SiO_2(2 µm) substrate using electron beam lithography (EBL) and sputtering techniques. Usually, due to charging issues, thick oxide layers are avoided for low energy EBID. However, time and availability constraints left no alternative. The wires were all 55 µm long but a number of different widths were available. Ultimately, 1 µm wide wires were chosen due to their well behaved switching and good visibility. In order to allow a domain wall to be easily and reliably nucleated in these wires, local gallium ion irradiation[78] was applied to a small region at the end of each one. As was mentioned, the high anisotropy in these multilayers is thought to be the result of interactions at the Co-Pt interfaces. By destructively modifying this interface with high energy Ga^+, this anisotropy can be reduced, making magnetisation reversal easier (effectively the opposite action of a pillar). For more details both of the fabrication of these wires and the gallium irradiation process, see Franken[78].

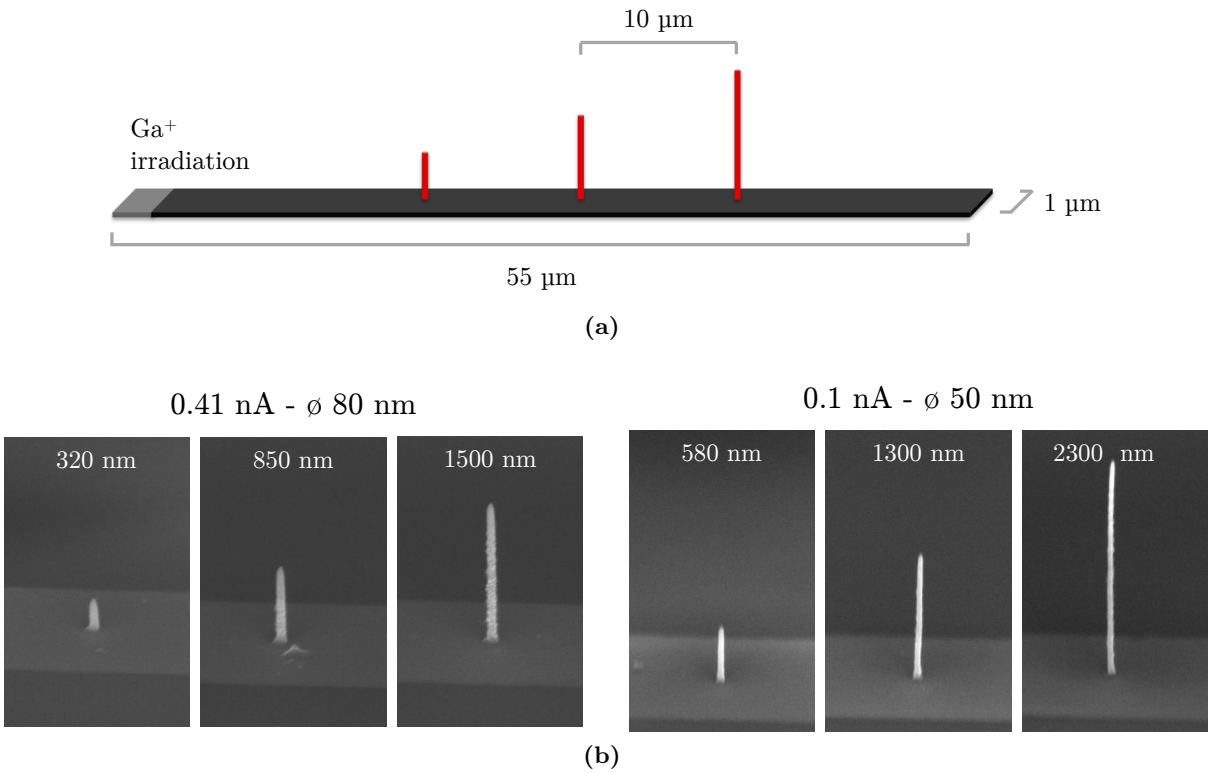

Figure 5.13: **(a)** A schematic representation of the a sample used for the experiment. Two different sets of three iron pillars were investigated, each deposited on a Pt/Co/Pt wire. **(b)** SEM images of these two sets (viewed 52° from the normal). The diameters and heights of the pillars are indicated.

As schematically illustrated in figure 5.13a, the three pillars of each group were deposited onto these wires 10 µm apart with the shortest and thus easiest to reverse, closest to the gallium irradiated area where a domain wall would be nucleated. SEM images of the deposits are shown in figure 5.13b. The pillars produced at 0.41 nA had an average diameter of 80 nm, those at 0.1 nA, 50 nm. Unfortunately, due to substantial drift caused by the charging of the insulating SiO_2 substrate, EDX measurements could not be reliable carried out. However, both sets of pillars were expected to have an iron content of around 50 to 60 at.%. To ease subsequent discussion, each pillar/wire system is referenced by the current used to create them.

Results

Domain wall motion was observed using Kerr microscopy (subsection 2.2.4), with switching achieved by applying a perpendicular magnetic field. To quantitatively record the switching of a wire, its Kerr intensity (contrast) was monitored as a function of applied field. Experiments were carried out following the scheme illustrated in figure 5.10. First a -20 mT field is briefly applied to align the magnetisation of both the wire and the pillar in one direction. Then a 3 mT field is applied in the opposite direction to switch the magnetisation of the gallium irradiated region and thereby nucleate a domain wall. Finally, to de-pin the wall and induce DMW this field is linearly increased.

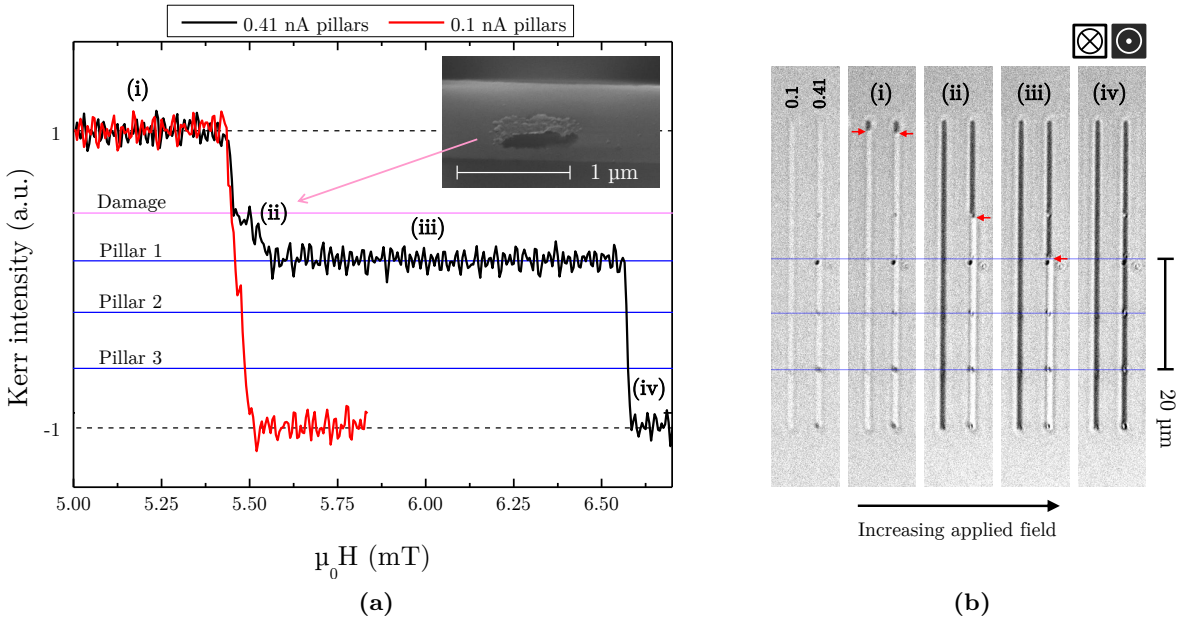

Figure 5.14: DWM of Pt/Co/Pt wires in the presence of iron nanopillars. **(a)** The Kerr intensity of two wires containing 0.41 nA (black) and 0.1 nA (red) iron pillars as a function of applied field. Intensity is normalised such that 1 corresponds to a un-switched wire (bright) and -1 to a switched wire (dark). The field was increased linearly (∼1.5 mT per minute), inducing domain wall motion and a gradual switching (darkening) of the wire. The Kerr intensities corresponding to the positions of the pillars are indicated. Only the influence of the first pillar on the 0.41 nA wire is apparent. A SEM image of a damaged region of the wire is inset. Critical points (i) to (iv) are discussed in the text. Single measurements are presented since averaging was made ineffective by slight variations in switching fields between experiments due to random thermal influences. **(b)** Kerr microscopy images of the same switching process shown in (a). Black/gray contrast describes magnetisation out of and into the page respectively. The locations of the pillars are indicated with horizontal lines, and domain walls with arrows. As a magnetic field (applied out of the page) is increased in strength going from left to right, the nucleation of domain walls and subsequent DWM is apparent from the top to the bottom of each wires.

The results of such a procedure, excluding the saturation and nucleation steps, are presented both quantitatively and qualitatively for both wires in figure 5.14. In figure 5.14a, the Kerr intensity of each wire is plotted as a function of applied field (0.41 nA in black, 0.1 nA in red). This intensity essentially defines the position of the domain wall along the wire and is normalised such that for 1 it is at the very beginning (unswitched) and -1 it is at the very end (switched) of the wire. Intermediate Kerr intensities corresponding to numerous critical points, such as the pillars, are labelled. Figure 5.14b shows a number of Kerr micrographs of the two wires (0.1 nA left, 0.41 nA right). The location of the pillars is again indicated with horizontal

lines, and domain walls are pointed out with arrows. Four key points, (i) to (iv), are labelled in each figure and these will now be described.

(i) As indicated in the Kerr image, the domain walls in both wires are pinned in the gallium irradiated region at the beginning of the wires. Correspondingly the Kerr intensity is high (∼1).

(ii) At an applied field of approximately 5.5 mT, both domain walls de-pin. In the 0.1 nA wire the wall subsequently proceeded all the way to the other side of the wire unimpeded bringing the Kerr intensity to -1. In the 0.41 nA wire however, after initially also travelling quite quickly, the wall velocity was slowed as it crossed a damaged region of the wire (a SEM image of the damage is inset in the figure).

(iii) After passing the damaged region, the wall is very clearly pinned at the position of the first pillar. Persisting as the field is increased by almost 1 mT, this pinning is particularly strong.

(iv) Finally, at a little over 6.6 mT, the wall de-pins and continues, without further delay, to the end of the wire.

The time between (i) and (iv) is approximately 65 seconds corresponding to a field sweep rate of ∼1.5 mT per minute.

From these results it appears as though the 0.1 nA pillars have no impact on DWM. The 0.41 nA pillars however, specifically the first, shortest one, clearly does pin a passing domain wall. From figure 5.14, the second and third 0.41 nA pillars appear to have no influence on the wall. However, under certain conditions, a minor effect was often observed. By applying a field just sufficient for a wall to pass the first pillar (∼6.5 mT) and then keeping it constant, the wall was often observed to pause momentarily (< 1 s) at the positions of the second and third pillars, as illustrated in figure 5.15. The pinning was very weak, and even if the applied field was switched off, thermal fluctuations were generally sufficient to induce depinning.

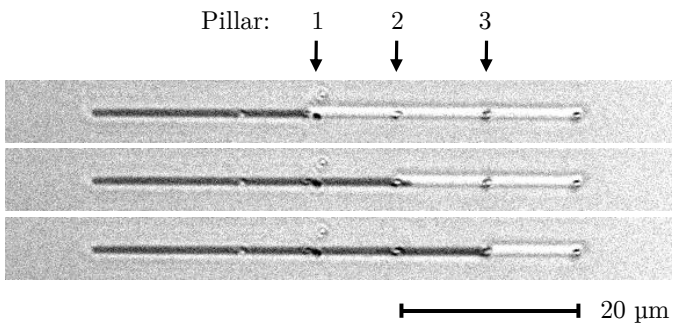

Figure 5.15: Kerr micrographs showing the occasional domain wall pinning induced by the second and third 0.41 nA pillars. This pinning was typically very brief (< 1 s).

To investigate the cause of the strong pinning induced by the first of the 0.41 nA pillars, additional experiments were carried out following the idea depicted in figure 5.11. The fields required either to make a domain wall approach, withdraw or pass the pillar were compared. If the pinning is magnetic in nature, the pillar is expected to behave as an energy barrier. As suggested in the figure, for such a barrier, the 'withdraw field' should be approximately equal to the 'approach field', and be significantly smaller than the field required to transit the pillar.

Measurements revealed that indeed, moving a wall towards and away from the pillar on either side required similar fields, at least 0.5 mT below that required to pass the pillar completely. This suggests that to a domain wall, the pillar appears as an energy barrier and although not unique, is a good indication that the cause of the pinning is magnetic in nature.

It is not completely clear why only the first pillar of the 0.41 nA set had this seemingly magnetic influence. One reasonable explanation is that the coercive field of all three pillars was very similar such that once a field sufficient to pass the first one was applied, the second two had also flipped. This assumes all three deposits are magnetic. It is possible that it is this magnetic character which is responsible for the very weak influence of the second and third pillars sometimes observed. Although the simulations predicted that with an aspect ratio of just 4, the coercive field of the first pillar should have been lower than that of the two larger pillars, this explanation is still consistent with the general idea that pillar length is not particularly important for H_c.

In addition to this, it is also unclear why all three of the 0.41 nA pillars had some kind of influence, but none of the 0.1 nA pillars did. One explanation may relate a difference in composition. The optimisation work of section 5.1 would suggest that the iron content of pillars grown at both these currents should be approximately equal. However, the precursor issue mentioned at the beginning of this subsection could have changed things. Although EDX could unfortunately not be performed to confirm these suspicions, with higher currents generally associated with higher purities, the 0.1 nA pillars may simple have insufficient iron to be magnetic. As was discovered in the previous chapter, once iron content begins to approach 50 at.% with the remainder mostly oxygen, as is likely the case here, ferromagnetic behaviour can become difficult to detect (at least optically). An additional explanation relates to the diameter the pillars, the only obvious physical way in which the two sets differ. The simulations argue that a thinner pillar, having a higher coercivity, would have a stronger pinning effect than a thicker pillar. However, if the pinning effect is considered to be purely physical in nature, to be the result of the deposit or deposition process itself, a larger pillar might have a larger influence. There are arguments both for and against such an idea. The Pt/Co/Pt wires are very thin and thus could be particularly sensitive to such an effect. In addition, the irradiative nature of the EBID technique is intrinsically rather violent. Conversely, the actual difference between the wires which do and do not exhibit such an effect on the scale of the width of the pillars is very small (80/1000 vs. 50/1000). Thankfully, due to the versatility of the dualbeam, such a 'presence effect' can be easily tested for by repeating a DWM experiment using non-magnetic pillars, as discussed below.

Using the platinum precursor available in the dualbeam and a 5 kV, 0.41 nA electron beam (in immersion mode), four platinum[†] pillars of different heights (1–2.2 µm) were deposited onto a new, Ga^+ irradiated, Pt/Co/Pt wire. Unfortunately, experimental conditions could not be exactly matched to earlier experiments. Due to availability issues, the pillars had to be deposited on a 2 µm wide wire. In addition, although the tips of the Pt deposits were similar to the iron pillars (ø 70 nm), their bases were very broad (200 nm, see figure 5.16b), likely the combined consequence of high precursor pressures ($> 1\times10^{-5}$ mbar, typical for the Pt GIS) and diffusion enhanced growth effects.[84] Regardless, the same DWM experiment (figure 5.10) was carried out and the results are shown in figure 5.16a. With the positions of the Pt pillars indicated with horizontal lines, it is clear that after depinning at around 5.65 mT, although travelling slower and less smoothly than in the narrower wires (due to increased intrinsic defect pinning in the wider wire), the domain wall was not specifically influenced by any of the Pt deposits.

[†]Platinum might seem a poor choice given the composition of the wires, but with EBID Pt deposits typically less than 30 at.% pure (the rest C and O) a modification of the multilayered wire structure is not expected.

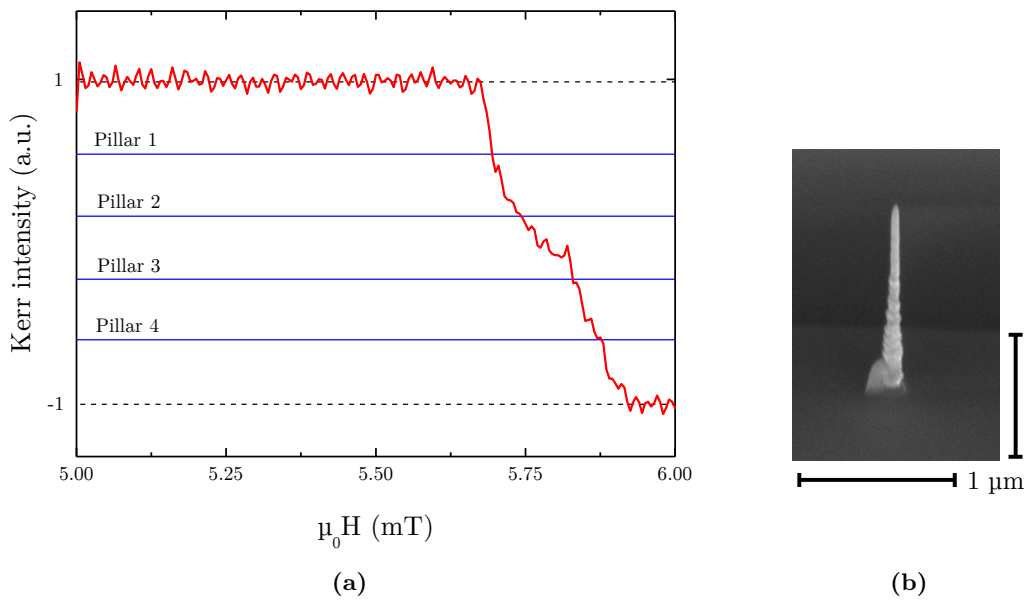

Figure 5.16: **(a)** The Kerr intensity of a wire containing 0.41 nA platinum pillars as a function of applied field. Intensity is normalised such that 1 corresponds to a unswitched wire (bright) and -1 to switched wire (dark). Following the experiment performed on the iron pillars, the field was increased linearly (∼1.5 mT per minute), inducing domain wall motion and a gradual switching (darkening) of the wire. The Kerr intensities corresponding to the positions of the pillars are indicated. No correlation between the positions of the pillars and the DWM is apparent. **(b)** A typical Pt pillar deposit, showing its unusual form (produced using a 5 kV, 0.41 nA electron beam with the immersion lens).

5.3.3 Conclusions

Although this was only a prelimary investigation, involving a very limited number of experiments, the results are already promising. Although not yet indisputable, there is significant evidence that iron pillars deposited by EBID are not only magnetic, but are sufficiently magnetic to influence domain wall motion with their stray fields. Given the very small number of experiments performed and the very large parameter space, the chance to observe this effect was very small. Had the depinning of the domain wall occurred at just a one or two millitesla more, nothing would have been observed. Although many of the dependencies of the magnetic pinning are not yet clear, most of these issues should be readily straightforward to address by simply performing more experiments on a larger range of pillar deposits.

Conclusions and Outlook

To end this thesis, the important findings and conclusions of the previous chapters are briefly summarised here. Detailed discussion of this nature has been presented at the end of the previous three chapters, so is kept short here. In addition to conclusions, an outlook on possible future research is also presented.

Conclusions

The general aim of the ongoing project between FNA and FEI is to investigate the potential of the $Fe_2(CO)_9$ precursor for EBID of magnetic nanomaterials. For this work specifically, two goals were defined: to further characterise the $Fe_2(CO)_9$ precursor and to begin investigating deposits suitable for preliminary magnetic applications. Both of these goals have been successfully achieved. Key results are presented in terms of these two goals below.

Microwires

In chapters 3 and 4, the characterisation of simple microwire deposits was discussed.

Chapter 3 considered deposits produced under optimal vacuum conditions. Using high electron beam currents (20 nA), and low energies (5 keV), such deposits consistently contained approximately 75 at.% iron. They displayed clear ferromagnetic behaviour, including AMR and hysteresis, and were highly conducting, with an average resistivity just ten times that of iron (100 µΩ·cm). With an almost flat temperature dependence (TCR: -23 ppm/K), conduction was slightly semiconducting in nature. Metallic conduction was achieved by annealing, however, following this process, oxidation appeared to become an issue. The microstructure of these deposits was found to depend on their thickness. Below approximately 200 nm, a mostly nanocrystalline structure was apparent, but growth above this thickness was crystalline.

In chapter 4, the influence of increasing oxygen content on these characteristics was considered. By worsening the vacuum conditions via controlled water vapour injection, the iron:oxygen ratio of deposits was varied from that of the optimal deposits (75:15) to as low as 50:50. As this ratio decreased, iron oxide grains were seen to develop, eventually leading to a columnar crystal structure in which both Fe_2O_3 and Fe_3O_4 were identified. Over the entire compositional range, resistivity was found to increase three orders of magnitude. Two separate exponential trends were apparent, corresponding to before and after percolation of the oxide grains. The temperature dependence of the resistivity was negative, but lower than expected for pure iron oxide. Deposits maintained some ferromagnetic character over the entire compositional range. As oxygen content increased, AMR was substituted by a grain boundary magnetoresistance (GBMR).

Nanopillars

In chapter 5, an investigation into freestanding iron pillars was presented. The influence of electron beam current and energy on deposit composition and size was considered. To maximise iron content (> 60 at.%) while minimising deposit size (diameter < 100 nm), a 5 keV electron beam and currents in the order of 100s of pA were found to be optimal. Beam induced heating phenomena were also investigated. Unusual crystalline pillar growth was both qualitatively and semi-quantitatively confirmed to be the result of the thermal dissociation of the precursor. Finally, in order to investigate both the magnetic properties and practical use of such pillars, a pilot experiment testing the influence of pillar deposits on domain wall motion was conducted. Of six deposited pillars, half had some influence, one very strongly. Further investigation of the strong influence suggested it was magnetic in origin. Non-magnetic platinum pillars were also deposited and had absolutely no influence.

Outlook

As was mentioned near the end of chapter 5, towards the end of this project, after the Fe GIS was refilled, deposits were found to contain much more oxygen than they had previously. Before research into the $Fe_2(CO)_9$ precursor can continue effectively, this issue will need to be addressed. Discussions with FEI are ongoing, but the cause is still not known. Assuming this issue is eventually overcome, some possible future investigations, both fundamental and more practical in nature, are briefly discussed below.

In terms of characterisation, the properties of the iron-rich microwires are now much better understood, however, there are still some open questions. The most significant of these relates to the cause of the thickness-dependent crystallisation. Although currently not coupled with an increase in composition, if better understood, it might be possible to also achieve increased purities. With disordered growth limited to regions near the substrate, it could be useful to more specifically investigate the influence of the surface on which depositions are made. In addition to different substrate materials or coatings (i.e., hydrophobic), the influence of seed layers (EBID or sputtered iron), or temperature could also be particularly interesting, and might eventually allow completely crystalline deposits to be produced.

Certain aspects of the water vapour investigations could also be expanded. Both the exact nature of the suspected GBMR effect, and the processes which disallow iron contents below ∼50 at.% to be achieved, are not yet clear. In both cases, further microstructural investigations would be beneficial. Also of particular interest is the ability to deposit half-metallic Fe_3O_4. Further work needs to be performed to optimise the deposition of this material, but eventually it might be possible to deposit near-pure crystalline Fe_3O_4 on demand, ideal for spintronic applications.

Investigations into performing *in situ* electrical measurements inside the dualbeam have begun recently. This also opens up a number of new experimental possibilities. Most specifically, this could allow the resistance of deposits to be monitor during deposition, giving a great deal of insight into growth processes.

The most exciting future work will undoubtedly relate to freestanding magnetic structures, such as the pillars investigated here. A particular issue for such deposits is characterisation. Due to their small size, composition measurements with EDX are already problematic, but direct electrical or magnetic characterisation is even more difficult. So far, the only indication that these pillar deposits are in fact magnetic has been the DWM experiment. The ability

to perform *in situ* electrical measurements would also open up some possibilities here. One approach could be to use the FIB of the dualbeam to 'cut down' the deposits and then, using nanomanipulators, orient them horizontally on electrical contacts. Similarly, by manipulating a small, sensitive, magnetic field sensor (such as a GMR or TMR stack) towards a pillar deposit, its stray field could be characterised. A final possibility, commonly mentioned in literature (see subsection 1.3.1) is to use electron holography.

Although beam induced heating effects are now better understood, their full potential for the deposition of high purity material has not yet been realised. So far, only very high currents and simple deposit geometries (pillars) have been investigated. The influence of beam energy has also not yet considered. Combined with the simulation program developed, it should also be possible to characterise the thermal properties of deposits dependent on the appearance of such effects.

The magnetic application of iron pillars in domain wall motion has so far shown promise, but further experimentation is required both to confirm the magnetic nature of the pillars and to gain better understand their effect. Once this is achieved, more complex structures could be investigated. A 'U' shaped geometry made out of iron essentially defines a horseshoe magnetic. With stray fields confined primarily between the ends, deposits of this nature could be used with in-plane magnetised materials. Given the versatility of the EBID technique, deposit intricacy is essentially only limited by the patience of the experimenter.

Appendix A

Deposit Longevity

Oxidation

With iron being deposited, an obvious concern is oxidation. Although no detailed oxidation investigations were carried out, the resistance of a few iron-rich microwire deposits was rechecked some time after their initial electrical characterisation. After being exposed to air for one month, the resistance of the three deposits was found to have *decreased* slightly (< 5 %). Oxidation could obviously not be responsible for such a result. The stability of these deposits is though to be the combined result of a rather high impurity concentration ($\sim$25 at.%) and a disordered microstructure in which these contaminates are mixed throughout. A similar stability was found in deposits with lower iron content.

It is possible that when deposits are first removed from the vacuum chamber of the dualbeam they oxidise slightly. However, given the generally low resistivity of deposits, the extent of this 'rusting' is not expected to be significant, and is likely limited to the surface.

Pillar Stability

A number of pillar deposits were revisited after the substrate they were deposited on had been exposed to air for almost three months. Stored in a sample box, glued to an aluminium stub, the deposits were generally not treated with care.

The majority of the large crystalline pillars grown using the immersion lens mode with high currents (section 5.2, figure 5.5) were found to have fallen over, as can be seen in figure A.1b and A.1a. Given the 'top heavy' nature of these deposits this result was of no great surprise. The crystal growth may also have made these particular pillars brittle. In contrast, the pillars also produced at high currents but in the regular lens mode remained standing (figure A.1c). Thin pillars, deposited at lower currents were also unaffected (figure A.1d).

The pillars utilised in section 5.3 for domain wall motion experiments were also found to be very robust and stable. The same domain pinning was observed many months after their original deposition.

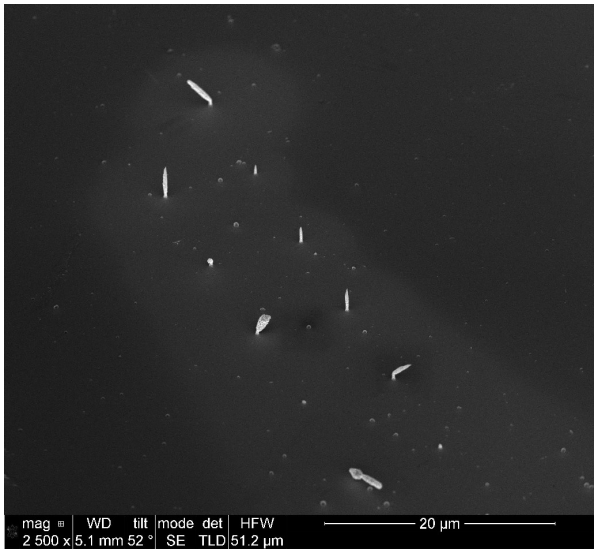

(a) Collapsed crystalline pillar deposits (5 keV, 18 nA, immersion lens mode).

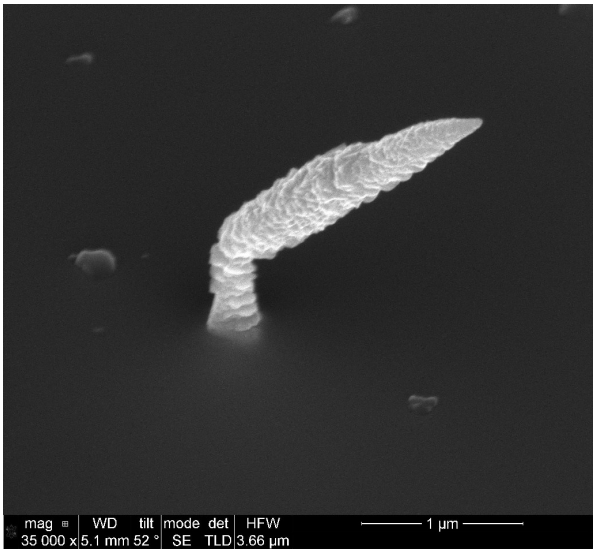

(b) A bent crystalline pillar deposit (5 keV, 18 nA, immersion lens mode).

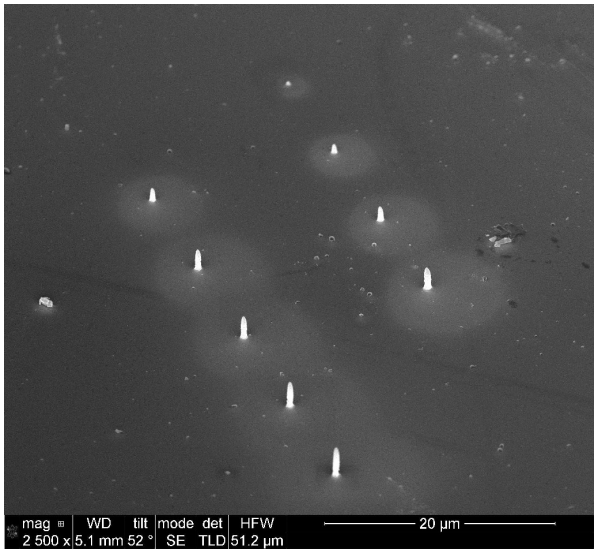

(c) Stable non-crystalline pillars (5 keV, 18 nA, regular lens mode).

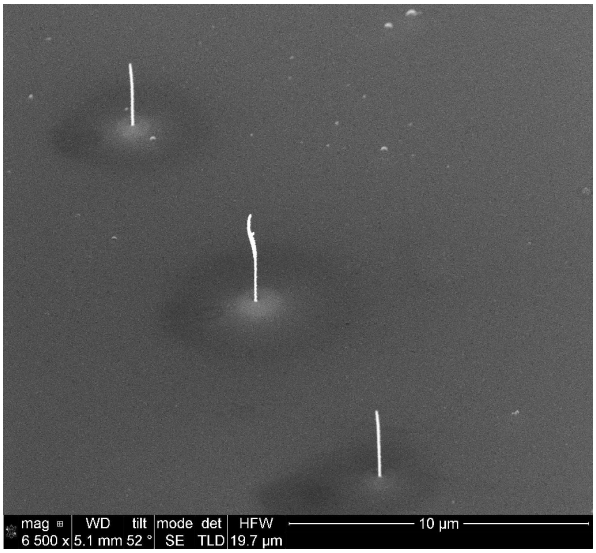

(d) Stable, low current thin pillars (5 keV, 0.46 nA, immersion lens mode).

Figure A.1: SEM images of a number of different pillars almost three months after their deposition.

Appendix B

Deposition on Thin Films: Thermal Effects

Figure B.1 shows the crystalline iron growth which resulting when the centre of a thin and thus thermally insulating film was irradiated with a high current electron beam.

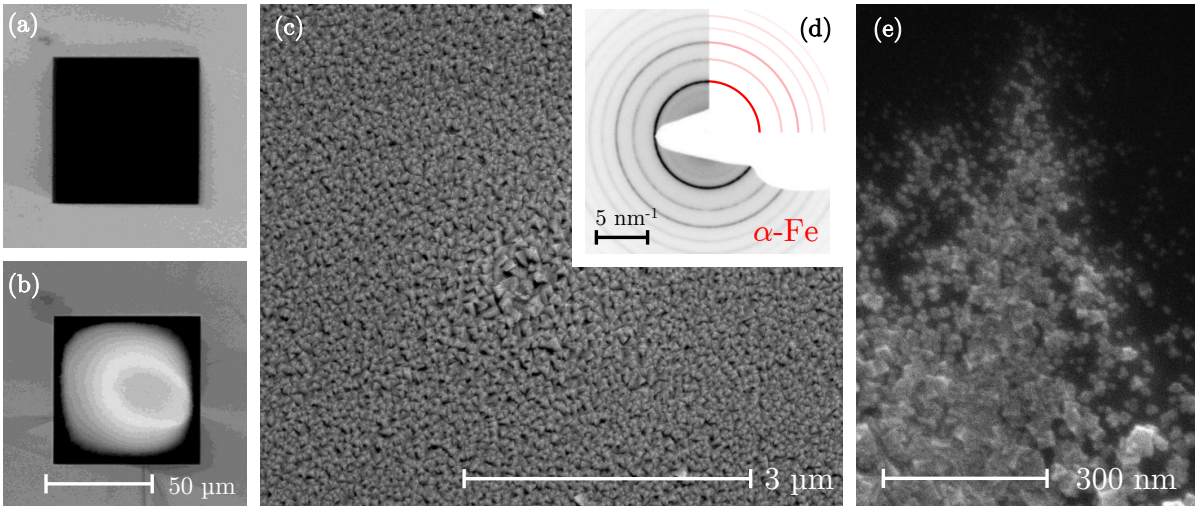

Figure B.1: Crystalline growth resulting after irradiating the centre of a thin (20 nm) Si_3N_4 membrane for 60 s with a 5 kV, 24 nA electron beam in spot-mode. With growth extending a distance of more than 20 µm away from the beam, precursor decomposition is undoubtedly thermally induced. EDX spectroscopy revealed a composition of 86/9/5 at.% (Fe/O/C) **(a)** TEM membrane window before irradiation. **(b)** After irradiation (the oval distortion is an imaging artifact resulting from charging). **(c)** The centre of the resulting crystalline deposition and where the electron beam was positioned. **(d)** The electron diffraction pattern resulting from the growth clearly indicating α-iron (bcc). **(e)** Dendritic crystal growth, 25 µm from the irradiation region.

Appendix C

Modelling Beam Induced Heating

In this appendix, the computational details of the beam induced heating simulations discussed in subsection 5.2.2 are presented.

Monte Carlo Scattering Simulations

A Monte Carlo (MC) based electron scattering simulation was developed with MATLAB, following the single scattering model detailed by Joy.[85,86] This model is based on two important assumptions.

Firstly, only elastic scattering events are considered important for determining electron trajectories. While elastic scattering is commonly responsible for scattering of 5 to 180°, inelastic collisions typically only cause very small deviations of fractions of a degree and thus have a significantly lesser effect on electron trajectories. Consequently, in the simulation, collisions are governed by an expression describing an interaction cross section for elastic scattering.

A common choice in this regard is the relativistically corrected screened Rutherford cross section,[64,86] classically derived from Coulomb scattering theory. Such an approach, however, becomes inaccurate for the low electron energies typically used in commercial SEMs (2–30 keV). Consequently, as a modification to the standard single scattering model, a cross section derived from Mott scattering theory is implemented instead. The more accurate Mott cross section is able to account for spin dependent scattering effects. However, since, as derived, this cross section cannot be expressed analytically, an empirical expression,[87] accurate over the energy range of interest, is used to approximate it:

$$\sigma = 4.7\times10^{-18}\cdot\frac{(Z^{1.33}+0.032Z^2)}{(E+0.0155Z^{1.33}\cdot E^{0.5})}\cdot\frac{1}{(1-0.02Z^{0.5}\cdot\exp(-(\log(8EZ^{-1.33})^2)))},(\mathrm{cm}^2) \quad \text{(C.1)}$$

where E is the electron energy (in keV) and Z the atomic number of the target material.

The second major assumption of this model relates to how electron energy loss is simulated. Since inelastic scattering, ordinarily responsible for energy loss, is ignored, an electron is instead assumed to lose energy continuously as it travels through the target material. By using an expression incorporating into it all possible energy loss mechanisms things are greatly simplified.

Such an expression was developed by Bethe[88]. It defines the rate (as a function of distance travelled) at which the energy of a scattering electron is transferred to the material in which it is travelling. Again modified for low energies[89], this takes the form:

$$\frac{dE}{dS} = -78500 \cdot \frac{\rho Z}{AE} \cdot \ln\left(\frac{1.166(E + 0.85J)}{J}\right), \qquad \text{(keV/cm)} \tag{C.2}$$

where S is the distance travelled (in cm), ρ is the density (g/cm^3), A the atomic weight, and J the mean ionisation potential ($J = (9.76Z + 58.5/Z^{0.19}) \cdot 10^{-3}$) of the target material (in keV).

It should be noted that the nature of this approach means that such scattering simulations are automatically restricted to modelling primary electrons. Although inelastic energy losses are accounted for, the possible creation and propagation of secondary electrons is not considered. Although important for BID in general, for a rudimentary energy deposition investigation such as this, the influence of these low energy (<50 eV) electrons is considered insignificant.

Within these assumptions, electron trajectories are simulated by modelling individual scattering events using a typical Monte Carlo algorithm:

Repeat
- Get energy of electron E
- Calculate mean free path λ for this energy in the target
- Probabilistically compute step length S and scattering angles θ & ϕ
- Calculate energy lost over step dE

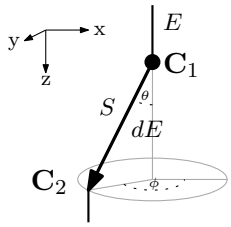

Beginning with user specified initial conditions (electron energy E, and position C_1), the scattering of an electron is governed by the cross section equation described above (equation C.1). From this expression the mean free path (MFP) of the electron in the target material can be calculated

$$\lambda = A/N_A \rho \sigma, \qquad \text{(cm)} \tag{C.3}$$

(ρ the density of the target material and N_A Avogadro's number), allowing the distance travelled before scattering, S, to be probabilistically determined

$$P(S) = \exp(-S/\lambda). \tag{C.4}$$

Scattering angles are then similarly determined. The polar angle (θ) from an empirical expression matching experimental results

$$\cos(\theta) = 1 - \frac{2 \cdot (3.4 \times 10^{-4} Z^{0.67}/E) rand^2}{1 + (3.4 \times 10^{-4} Z^{0.67}/E) - rand}, \tag{C.5}$$

for a random number $rand$, and the azimuthal angle (ϕ), randomly around 2π.

With the scattering event fully defined spatially ($C_1 \rightarrow C_2$), the last step of the simulation involves calculating the energy consequently lost by the electron, dE, in travelling the distance S, as given by the Bethe formula (equation C.2). At the end of an individual scattering event, the energy and position of the electron are updated ($C_1 = C_2$, $E = E - dE$), and the process is repeated. An electron trajectory continues until one of two conditions are met: electron energy drops below 50eV, or the electron leaves the volume representing the pillar.

Since the location (C_2) and energy loss (dE) of each scattering event can be recorded, by simulating a large number of these electron trajectories, a distribution representing how energy is deposited by an electron beam in a pillar structure is constructed. In preparation for the second phase of simulations, the resulting large array of continuous data is discretised. Assuming axial

symmetry, just a radial slice of the data is processed, with a resolution of 10 nm. Furthermore, given the number of electron trajectories simulated, the specified beam current to be modelled and the 10 nm binning, the data is converted from an energy to a power density before finally being exported to a text file.

Implementation

Pillars were modelled as cylindrical volumes with rounded tips. Although these simulations cannot account for interface scattering effects, the simulated shape of the tip of the pillar can still have a significant influence on resulting energy deposition predictions.[70] The simplest case of a dome tip was considered here. Also, to model the Gaussian shape of the electron beam, the starting position of an incident electron above the pillar was randomly varied distribution (2-D normal distribution).

Figure C.1 shows a typical result of such simulations for 10,000 5 keV electron trajectories scattering in a dome-tipped iron pillar. Figure C.1a shows the actually scattering simulation. Absorbed (blue), backscattered (red) and side-scattered electrons (green) are all shown. The limits of the modelled pillar are also shown as rings. Figure C.1b shows the resulting power density distribution slice.

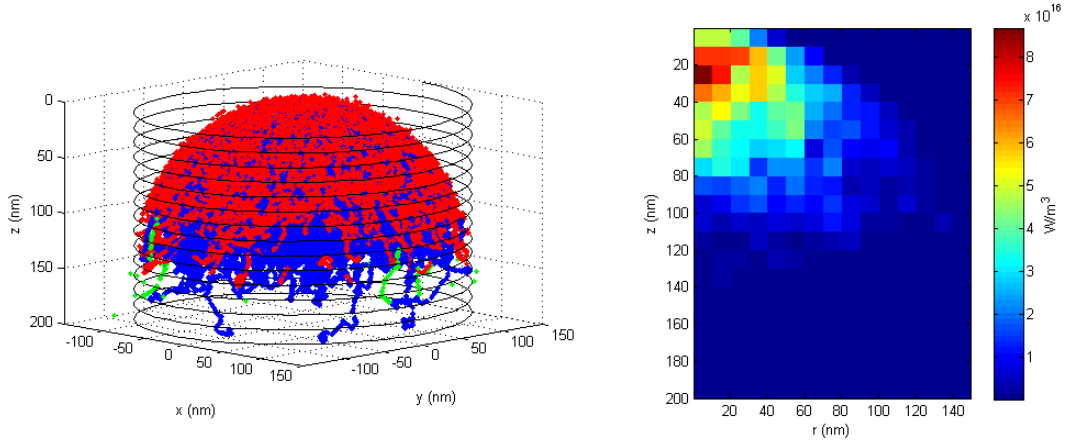

(a) **(b)**

Figure C.1: The typical output of a scattering simulation. **(a)** shows the simulated trajectories for 10,000 5 keV electrons from a gaussian (FWHM = 100 nm) beam in a pure iron pillar, ø 300 nm. Red traces represent backscattered paths; green, side exit paths; and blue, scattering trajectories which remained in the pillar. **(b)** the corresponding power density data (10 nm binning) for a 20 nA beam current.

Modelling Heat Flow

To model heat flow the commercial finite element analysis simulation package COMSOL Multiphysics has been used.[82] Pillar geometries matching those used in the scattering simulations are modelled in a 2-D environment with axial symmetry. Thermalisation is assumed to occur much faster than pillar growth[64] and consequently, the heat equation is solved in the steady-state as

$$\kappa \nabla^2 T + Q = \kappa \left(\frac{\partial^2 T}{\partial r^2} + \frac{1}{r}\frac{\partial T}{\partial r} + \frac{\partial^2 T}{\partial z^2} \right) + Q(r,z) = 0. \tag{C.6}$$

Here, κ is the thermal conductivity of the target material (assumed isotropic), T is the temper-

ature, and Q is the power density, determined from the previous scattering simulations. This simplified approach implies not only that all the kinetic energy of the electrons is transferred into heat,[68] but also that other heat transfer mechanisms such as convection or radiation, are ignored.

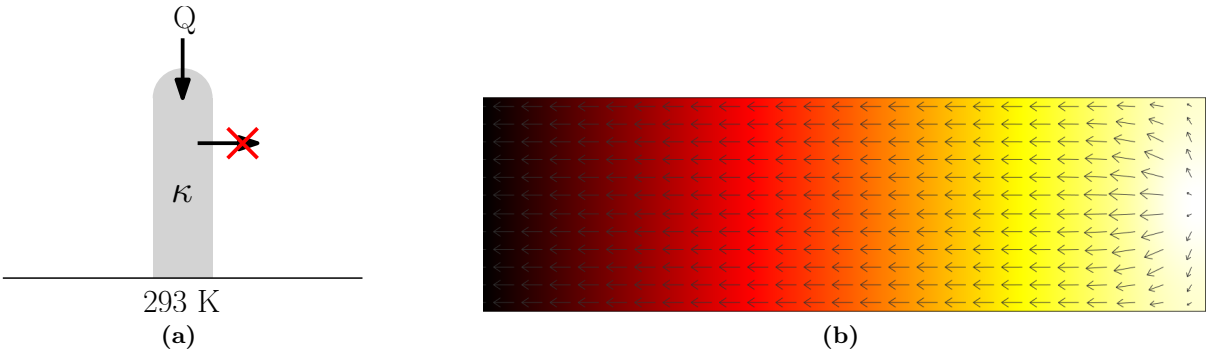

Figure C.2: **(a)** The basic assumptions used to model the heat flow through a pillar. **(b)** Solution to equation C.6 for a ø300 nm pillar of pure iron and the power distribution (Q) of figure C.1b. Colour gradient represents temperature, arrows heat flux (a.u.).

As illustrated in figure C.2a, equation C.6 is numerically solved under the conditions that the pillar is initially at room temperature (293K), that vacuum interfaces are thermally insulating, and that the pillar-substrate interface remains at 293K (this condition was found to be effectively equivalent to modelling a semi-infinite silicon substrate). Following this approach, using the energy distribution presented in figure C.1b (5 keV, 20 nA beam in a ø300 nm pillar of pure iron), produces figure C.2b.

Appendix D

Larger Depositions

While the electrical experimental techniques used extensively in this work lend themselves to wire geometries, to open up other characterisation possibilities while at the same time testing the limits of the EBID technique, a single very large iron deposit was also produced. Measuring 120 x 100 µm, a sample was deposited on a Si-B substrate over a continuous 22 hour 40 minute period (figure D.1).

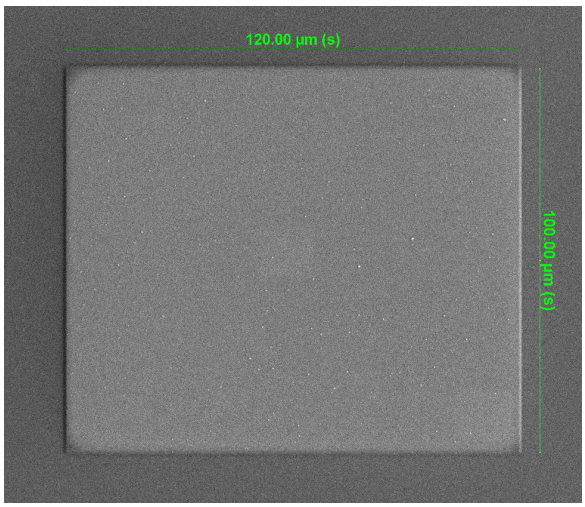

Figure D.1: A SEM image of a large EBID iron deposit produced over a 22:40 period (5 keV, 20 nA, regular lens mode).

From EDX spectroscopy, the content of the deposit was determined to be 62/21/17 at.% (Fe/O/C), lower than typically found for nanowires when no water is added. This result highlights the difficulty of performing EBID over such a long period. It is likely this lower content is the combined result of changes in the GIS and hence precursor flux as well as the electron beam. Furthermore, as well as being produced over an unusually long time, this deposit was also extremely large physically. Trying to pattern such an area with raster methods means the interval between passes is quite long (in this case, one second), and thus, so too is the possibility for vacuum contaminates to adsorb and eventually be integrated into the deposit. Using a surface profiler (an AFM device for larger lateral scales) the average height of the deposit was determined to be approximately 160nm giving a total volume of just over 1900 μm^3.

The original motivation for the creation of such a macroscopic deposit was to allow the magnetisation of the iron EBID material to be determined via SQUID (Superconducting QUantum

Interference Device) magnetometery; this goal defined the volume requirement of the deposit. However, even with supposedly sufficient magnetic material for detection, measurement results were inconclusive, indicating a magnetisation significantly above that expected for a pure iron deposit. Subsequently, the focus shifted to a Kerr microscopy investigation of the large and thus highly visible deposit.

Kerr Microscopy

Using the wide-field Kerr microscope described in subsection 2.2.4, the magnetisation structure and switching of the deposit was investigated. Figure D.2a shows the hysteresis behaviour of the deposit as a field is swept along its long axis (120 µm); Kerr images at saturation and remanence are also included. The magnetisation around the edges of the deposit was found to be harder to reorientate than the bulk, leading to the observed first gradual ($H > 1$ mT) and then sudden ($H < 1$ mT) switching behaviour. The formation of large magnetic domains is apparent in the Kerr images, with a clear non-zero remanent state. By investigating the deposit with both longitudinal (figure D.2b) and transverse (figure D.2c) Kerr sensitivity, the remanent state magnetisation was completely characterised, as shown in figure D.2d. The domain structure is such as to minimise stray fields; a flux closure structure exists.

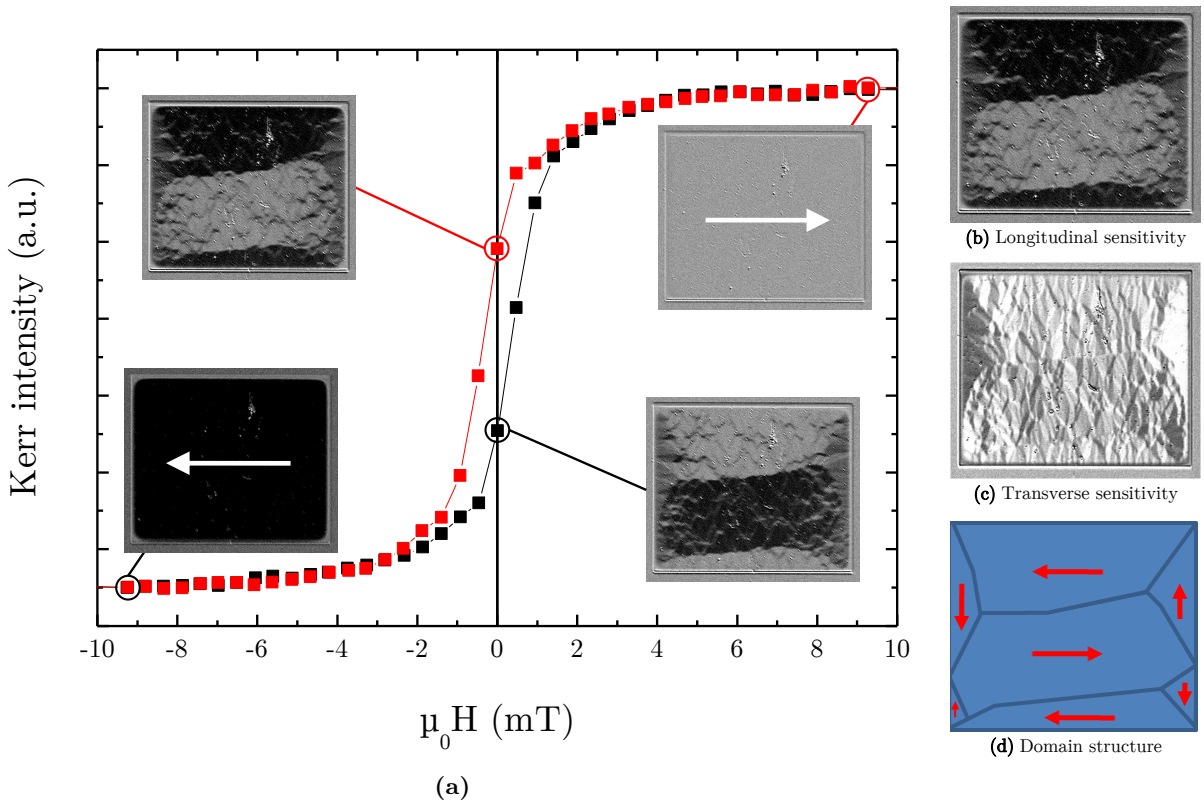

Figure D.2: **(a)** The hysteresis loop produced by the large deposit for a a longitudinally swept field (along the 120 µm dimension). Kerr images of specific in-plane magnetisation states are also shown, with dark the the left and bright to the right, as indicated. **(b-d)** By inspecting the deposit with Kerr sensitivity along both principal dimensions, the complete domain structure can be determined.

Appendix E

Ion Beam Induced Deposition

To briefly investigate the possibility of IBID with the $Fe_2(CO)_9$ precursor, two IBID depos microwires were produced and briefly characterised. IBID is typically capable of much higher yields than EBID and is subsequently often of more interest for commercial applications. Using a 30 keV, 37 pA beam, two 15 µm x 500 nm microwires were deposited, one is depicted in figure E.1. As is apparent from the insert AFM profile in the figure, the cross-section of the deposits was much more rectangular than that of equivalent EBID wires. This is likely due to combined milling-depositing action of the ions. As a result of gallium implantation, iron content was relatively low (55-4-13-28, Fe-O-C-Ga at.%).

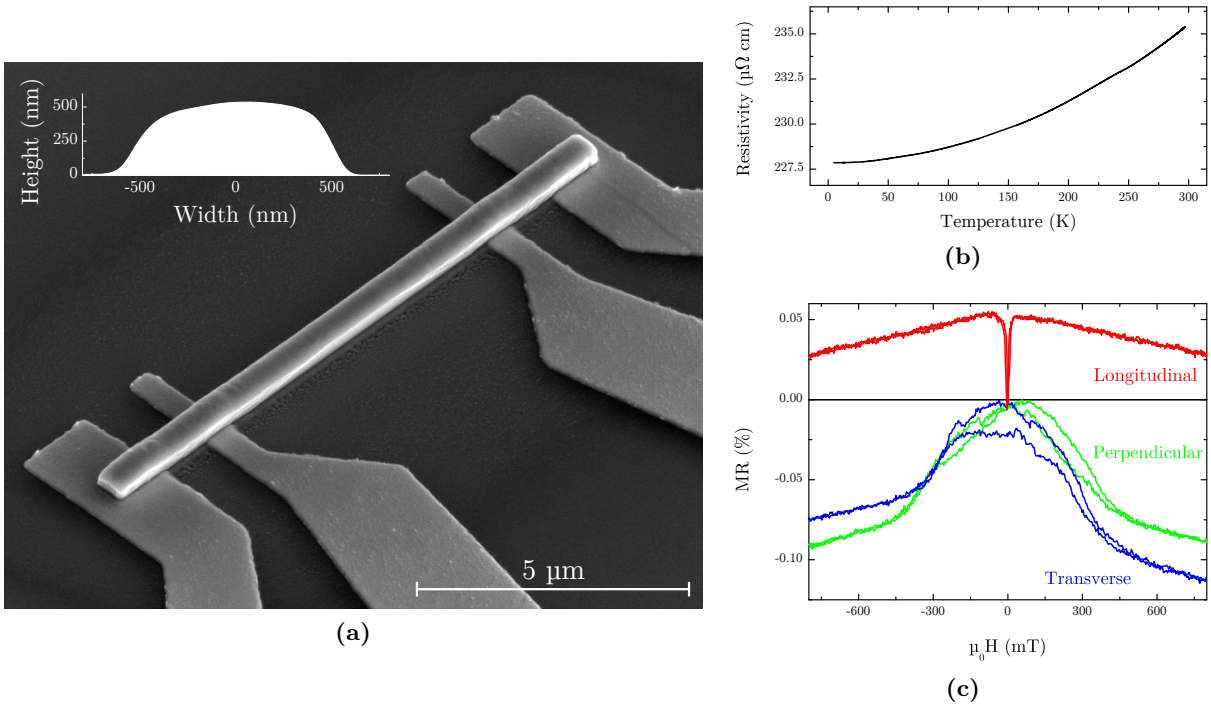

Figure E.1: **(a)** A SEM image of one of the IBID microwires with an AFM profile inset. **(b)** Deposit resistance as a function of temperature. **(c)** The magnetoresistive behaviour of the deposit.

Both electric and magnetic characterisation was carried out. In spite of the low iron content, the deposits had low resistivities (∼200 µΩ·cm) and as shown in figure E.1b, exhibited slightly metallic conduction. This was undoubtedly caused by the high gallium content. The magnetoresistance measured in one of the deposits is shown in figure E.1c. At low fields AMR is apparent,

while at higher fields, isotropic normal magnetoresistance effect can be seen. The cause of the asymmetry in the transverse AMR component is unknown. The large relative magnitude of the longitudinal AMR suggests that the remanent magnetisation is not well aligned to the easy axis of the wire. Furthermore, with both transverse and perpendicular AMR saturating at a rather low field of 400 mT, it appears as though the magnetisation is particularly easy to manipulate. This suggests that the ferromagnetic coupling in the deposits is rather weak.

Bibliography

1. W. F. van Dorp and C. W. Hagen. A critical literature review of focused electron beam induced deposition. *Journal of Applied Physics*, 104(8):081301, 2008. URL http://dx.doi.org/10.1063/1.2977587.

2. J. D. Fowlkes, S. J. Randolph, and P. D. Rack. Growth and simulation of high-aspect ratio nanopillars by primary and secondary electron-induced deposition. *Journal of Vacuum Science Technology B: Microelectronics and Nanometer Structures*, 23(6):2825 –2832, November 2005. ISSN 1071-1023. URL http://dx.doi.org/10.1116/1.2101732.

3. Ivo Utke, Patrik Hoffmann, and John Melngailis. Gas-assisted focused electron beam and ion beam processing and fabrication. *Journal of Vacuum Science & Technology B: Microelectronics and Nanometer Structures*, 26(4):1197–1276, 2008. URL http://dx.doi.org/10.1116/1.2955728.

4. M. Beljaars. Electron Beam Induced Deposition of Iron. Master's thesis, Eindhoven University of Technology, 2008.

5. Amikam Aharoni. Demagnetizing factors for rectangular ferromagnetic prisms. *Journal of Applied Physics*, 83(6):3432–3434, 1998. URL http://dx.doi.org/10.1063/1.367113.

6. H.J.M. Swagten. *Magnetism & Magnetic Materials*. 3S100 course syllabus, The Technical University of Eindhoven, 2008-2009.

7. N. F. Mott. The Electrical Conductivity of Transition Metals. *Royal Society of London Proceedings Series A*, 153:699–717, February 1936. URL http://www.jstor.org/stable/96578.

8. J. Smit. Magnetoresistance of ferromagnetic metals and alloys at low temperatures. *Physica*, 17(6):612 – 627, 1951. ISSN 0031-8914. URL http://dx.doi.org/10.1016/0031-8914(51)90117-6.

9. N.J. Turro. *Modern molecular photochemistry*, chapter A primitive model of spin-orbit coupling, pages 48–51. University Science Books, 1991.

10. A Botman, J J L Mulders, and C W Hagen. Creating pure nanostructures from electron-beam-induced deposition using purification techniques: a technology perspective. *Nanotechnology*, 20(37):372001, 2009. URL http://stacks.iop.org/0957-4484/20/i=37/a=372001.

11. B. Abeles, P. Sheng, M. D. Coutts, and Y. Arie. Structural and electrical properties of granular metal films. *Advances in Physics*, 24:407–461, May 1975. URL http://dx.doi.org/10.1080/00018737500101431.

12. Minoru Isshiki Yoshio Waseda. *Purification process and characterization of ultra high purity metals: application of basic science to metallurgical processing*, chapter 2. Principles of metal purification and purity evaluation. Springer series in materials processing. Springer, 2002.

13. I A Campbell, A Fert, and O Jaoul. The spontaneous resistivity anisotropy in ni-based alloys. *Journal of Physics C: Solid State Physics*, 3(1S):S95, 1970. URL http://stacks.iop.org/0022-3719/3/i=1S/a=310.

14. T. McGuire and R. Potter. Anisotropic magnetoresistance in ferromagnetic 3d alloys. *Magnetics, IEEE Transactions on*, 11(4):1018 – 1038, jul 1975. ISSN 0018-9464. URL http://dx.doi.org/10.1109/TMAG.1975.1058782.

15. M Ziese and H J Blythe. Magnetoresistance of magnetite. *Journal of Physics: Condensed Matter*, 12(1):13, 2000. URL http://stacks.iop.org/0953-8984/12/i=1/a=302.

16. Manabu Hasegawa, H. Yanagihara, Yuta Toyoda, Eiji Kita, and L. Ranno. Electrical and magnetic properties of [gamma]-fe2o3 epitaxial films. *Journal of Magnetism and Magnetic Materials*, 310(2, Part 3):2283 – 2285, 2007. ISSN 0304-8853. URL http://dx.doi.org/10.1016/j.jmmm.2006.10.749. Proceedings of the 17th International Conference on Magnetism, The International Conference on Magnetism.

17. E. Knittle and R. Jeanloz. High-pressure electrical resistivity measurements of fe2o3: Comparison of static-compression and shock-wave experiments to 61 gpa. *Solid State Communications*, 58(2):129 – 131, 1986. ISSN 0038-1098. URL http://dx.doi.org/10.1016/0038-1098(86)90869-0.

18. Toivo T. Kodsa and Mark J. Hampden-Smith. *The Chemistry of Metal CVD*, chapter 8: Chemical Vapor Deposition of Assorted Metals. VCH, 1994.

19. Patricia M. George and J.L. Beauchamp. Deposition of metal films by the controlled decomposition of organometallic compounds on surfaces. *Thin Solid Films*, 67(1):L25 – L28, 1980. ISSN 0040-6090. URL http://dx.doi.org/10.1016/0040-6090(80)90311-9.

20. R. R. Kunz and T. M. Mayer. Catalytic growth rate enhancement of electron beam deposited iron films. *Applied Physics Letters*, 50(15):962–964, 1987. URL http://dx.doi.org/10.1063/1.97999.

21. Y. M. Lau, P. C. Chee, J. T. L. Thong, and V. Ng. Properties and applications of cobalt-based material produced by electron-beam-induced deposition. *Journal of Vacuum Science & Technology A: Vacuum, Surfaces, and Films*, 20(4):1295–1302, 2002. URL http://dx.doi.org/10.1116/1.1481040.

22. A FernÃąndez-Pacheco, J M De Teresa, R CÃşrdoba, and M R Ibarra. Magnetotransport properties of high-quality cobalt nanowires grown by focused-electron-beam-induced deposition. *Journal of Physics D: Applied Physics*, 42(5):055005, 2009. URL http://stacks.iop.org/0022-3727/42/i=5/a=055005.

23. A. Fernández-Pacheco, J. M. De Teresa, R. Córdoba, M. R. Ibarra, D. Petit, D. E. Read, L. O'Brien, E. R. Lewis, H. T. Zeng, and R. P. Cowburn. Domain wall conduit behavior in cobalt nanowires grown by focused electron beam induced deposition. *Applied Physics Letters*, 94(19):192509, 2009. URL http://dx.doi.org/10.1063/1.3139068.

24. I. Utke, J. Michler, P. Gasser, C. Santschi, D. Laub, M. Cantoni, P. A. Buffat, C. Jiao, and P. Hoffmann. Cross section investigations of compositions and sub-structures of tips obtained by focused electron beam induced deposition. *Advanced Engineering Materials*, 7(5):323–331, 2005. URL http://dx.doi.org10.1002/adem.200500061.

25. Mihai Gabureac, Laurent Bernau, Ivo Utke, and Giovanni Boero. Granular co-c nano-hall sensors by focused-beam-induced deposition. *Nanotechnology*, 21(11):115503, 2010. URL http://stacks.iop.org/0957-4484/21/i=11/a=115503.

26. Masaki Takeguchi, Masayuki Shimojo, and Kazuo Furuya. Fabrication of magnetic nanostructures using electron beam induced chemical vapour deposition. *Nanotechnology*, 16(8):1321, 2005. URL http://stacks.iop.org/0957-4484/16/i=8/a=057.

27. M. Takeguchi, M. Shimojo, and K. Furuya. Fabrication of Alpha-Iron and Iron Carbide Nanostructures by Electron-Beam Induced Chemical Vapor Deposition and Postdeposition Heat Treatment. *Japanese Journal of Applied Physics*, 44:5631–+, July 2005. URL http://dx.doi.org/10.1143/JJAP.44.5631.

28. M. Takeguchi, M. Shimojo, R. Che, and K. Furuya. Fabrication of a nano-magnet on a piezo-driven tip in a tem sample holder. *Journal of Materials Science*, 41:2627–2630, 2006. ISSN 0022-2461. URL http://dx.doi.org/10.1007/s10853-006-7825-8.

29. M Shimojo, M Takeguchi, and K Furuya. Formation of crystalline iron oxide nanostructures by electron beam-induced deposition at room temperature. *Nanotechnology*, 17(15):3637, 2006. URL http://dx.doi.org/10.1088/0957-4484/17/15/003.

30. Masayuki Shimojo, Masaki Takeguchi, Kazutaka Mitsuishi, Miyoko Tanaka, and Kazuo Furuya. Mechanisms of crystalline iron oxide formation in electron beam-induced deposition. *Japanese Journal of Applied Physics*, 46(9B):6247–6249, 2007. URL http://dx.doi.org/10.1143/JJAP.46.6247.

31. Masaki Takeguchi, Masayuki Shimojo, and Kazuo Furuya. Nanostructure fabrication by electron-beam-induced deposition with metal carbonyl precursor and water vapor. *Japanese Journal of Applied Physics*, 46 (9B):6183–6186, 2007. URL http://dx.doi.org/10.1143/JJAP.46.6183.

32. Thomas Lukasczyk, Michael Schirmer, Hans-Peter Steinrück, and Hubertus Marbach. Electron-beam-induced deposition in ultrahigh vacuum: Lithographic fabrication of clean iron nanostructures. *Small*, 4 (6):841–846, 2008. URL http://dx.doi.org/10.1002/smll.200701095.

33. Jens Müller, Stephan von Molnár, and Steffen Wirth. Room temperature magnetoresistance switching of permalloy thin films induced by iron nanoparticles. *Applied Physics Letters*, 92(9):093121, 2008. URL http://dx.doi.org/10.1063/1.2890761.

34. F.J. Schoenaker. Exploring the fabrication of ferromagnetic nanostructures by electron beam induced deposition. Master's thesis, Eindhoven University of Technology, 2010.

35. J. A. Bearden. X-Ray Wavelengths and X-Ray Atomic Energy Levels. National Standard Reference Data Series 14, National Bureau of Standards, 1967.

36. Rudolf Schäfer. *Investigation of Domains and Dynamics of Domain Walls by the Magneto-optical Kerr-effect*, volume 3 of *Handbook of Magnetism and Advanced Magnetic Materials*, chapter Part 5. John Wiley & Sons, Ltd, 2007. URL http://dx.doi.org/10.1002/9780470022184.hmm310.

37. D. Drouin, A. R. Couture, D. Joly, X. Tastet, V. Aimez, and R. Gauvin. CASINO V2.42Âă-ÂăA Fast and Easy-to-use Modeling Tool for Scanning Electron Microscopy and Microanalysis Users. *Scanning*, 29:92–101, 2007. URL http://dx.doi.org/10.1002/sca.20000.

38. JCPDS International Centre for Diffraction Data. *Powder diffraction file: Inorganic volume*. JCPDS, 1984.

39. R Lavrijsen, R Córdoba, F J Schoenaker, T H Ellis, B Barcones, J T Kohlhepp, H J M Swagten, B Koopmans, J M De Teresa, C Magén, M R Ibarra, P Trompenaars, and J J L Mulders. Fe:o:c grown by focused-electron-beam-induced deposition: magnetic and electric properties. *Nanotechnology*, 22(2):025302, 2011. URL http://stacks.iop.org/0957-4484/22/i=2/a=025302.

40. S. Enthaler, K. Junge, and M. Beller. Sustainable metal catalysis with iron: From rust to a rising star? *Angew Chem Int Ed Engl*, 47(18):3317–3321, 2008.

41. R. R. Kunz and T. M. Mayer. Electron beam induced surface nucleation and low-temperature decomposition of metal carbonyls. *Journal of Vacuum Science & Technology B: Microelectronics and Nanometer Structures*, 6(5):1557–1564, 1988. URL http://dx.doi.org/10.1116/1.584214.

42. David R. Lide, editor. *CRC Handbook of Chemistry and Physics*. CRC Press, 90 edition, 2010. URL http://www.hbcpnetbase.com.

43. Mark Tondra, Daniel K. Lottis, K. T. Riggs, Youjun Chen, E. Dan Dahlberg, and G. A. Prinz. Thickness dependence of the anisotropic magnetoresistance in epitaxial iron films. *Journal of Applied Physics*, 73(10): 6393–6395, 1993. URL http://dx.doi.org/10.1063/1.352607.

44. R. P. van Gorkom, J. Caro, T. M. Klapwijk, and S. Radelaar. Temperature and angular dependence of the anisotropic magnetoresistance in epitaxial fe films. *Phys. Rev. B*, 63(13):134432, Mar 2001. URL http://dx.doi.org/10.1103/PhysRevB.63.134432.

45. Mark Rubinstein, F. J. Rachford, W. W. Fuller, and G. A. Prinz. Electrical transport properties of thin epitaxially grown iron films. *Phys. Rev. B*, 37(15):8689–8700, May 1988. URL http://dx.doi.org/10.1103/PhysRevB.37.8689.

46. Yu Mei, Zeng-Jun Zhou, and H. L. Luo. Electrical resistivity of rf-sputtered iron oxide thin films. *Journal of Applied Physics*, 61(8):4388–4389, 1987. URL http://dx.doi.org/10.1063/1.338431.

47. M Ziese. Extrinsic magnetotransport phenomena in ferromagnetic oxides. *Reports on Progress in Physics*, 65(2):143, 2002. URL http://stacks.iop.org/0034-4885/65/i=2/a=202.

48. M. Ziese, R. Höhne, H.C. Semmelhack, H. Reckentin, N.H. Hong, and P. Esquinazi. Mechanism of grain-boundary magnetoresistance in fe_3o_4 films. *The European Physical Journal B - Condensed Matter and Complex Systems*, 28:415–422, 2002. ISSN 1434-6028. URL http://dx.doi.org/10.1140/epjb/e2002-00245-3.

49. S. I. Rybchenko, Y. Fujishiro, H. Takagi, and M. Awano. Effect of grain boundaries on the magnetoresistance of magnetite. *Phys. Rev. B*, 72(5):054424, Aug 2005. URL http://dx.doi.org/10.1103/PhysRevB.72.054424.

50. Wendong Wang, Minhui Yu, Matthias Batzill, Jibao He, Ulrike Diebold, and Jinke Tang. Enhanced tunneling magnetoresistance and high-spin polarization at room temperature in a polystyrene-coated fe_3o_4 granular system. *Phys. Rev. B*, 73(13):134412, Apr 2006. URL http://dx.doi.org/10.1103/PhysRevB.73.134412.

51. Y. Kitamoto, Y. Nakayama, and M. Abe. Spin-dependent intergranular transport in magnetite films deposited by ferrite plating. *Journal of Applied Physics*, 87(9):7130–7132, 2000. URL http://dx.doi.org/10.1063/1.372953.

52. Chando Park, Yingguo Peng, Jian-Gang Zhu, David E. Laughlin, and Robert M. White. Magnetoresistance of polycrystalline fe[sub 3]o[sub 4] films prepared by reactive sputtering at room temperature. *Journal of Applied Physics*, 97(10):10C303, 2005. URL http://dx.doi.org/10.1063/1.1847853.

53. Robert C. O'Handley. *Modern magnetic materials: principles and applications*, chapter 15. Electronic Transport in Magnetic Materials, page 557. Wiley, 2000.

54. Mathias Getzlaff. *Fundamentals of Magnetism*. Springer, 2008.

55. D. Serrate, J. M. De Teresa, P. A. Algarabel, R. Fernández-Pacheco, J. Galibert, and M. R. Ibarra. Grain-boundary magnetoresistance up to 42 t in cold-pressed fe[sub 3]o[sub 4] nanopowders. *Journal of Applied Physics*, 97(8):084317, 2005. URL http://dx.doi.org/10.1063/1.1868877.

56. A. Gerber. Spin-dependent scattering versus spin-dependent tunneling in heterogeneous ferromagnets. *Physica B: Condensed Matter*, 280(1-4):331 – 332, 2000. ISSN 0921-4526. URL http://dx.doi.org/10.1016/S0921-4526(99)01723-8.

57. Joseph Goldstein, Dale E. Newbury, David C. Joy, Patrick Echlin, Charles E. Lyman, and Eric Lifshin. *Scanning electron microscopy and x-ray microanalysis*. Springer, 3 edition, 2003.

58. K. T. Kohlmann-von Platen, J. Chlebek, M. Weiss, K. Reimer, H. Oertel, and W. H. Brunger. Resolution limits in electron-beam induced tungsten deposition. *Journal of Vacuum Science Technology B: Microelectronics and Nanometer Structures*, 11(6):2219 –2223, November 1993. ISSN 1071-1023. URL http://dx.doi.org/10.1116/1.586460.

59. W.F. Van Dorp. *Sub-10 nm focused electron beam induced deposition*. PhD thesis, Delft University of Technology, 2008.

60. N. Silvis-Cividjian, C. W. Hagen, L. H. A. Leunissen, and P. Kruit. The role of secondary electrons in electron-beam-induced-deposition spatial resolution. *Microelectronic Engineering*, 61-62:693 – 699, 2002. ISSN 0167-9317. URL http://dx.doi.org/10.1016/S0167-9317(02)00515-4.

61. Willem F. van Dorp, Bob van Someren, Cornelis W. Hagen, Pieter Kruit, and Peter A. Crozier. Approaching the resolution limit of nanometer-scale electron beam-induced deposition. *Nano Letters*, 5(7):1303–1307, 2005. URL http://dx.doi.org/10.1021/nl050522i.

62. J. Fujita, M. Ishida, T. Ichihashi, Y. Ochiai, T. Kaito, and S. Matsui. Carbon nanopillar laterally grown with electron beam-induced chemical vapor deposition. *Journal of Vacuum Science & Technology B: Microelectronics and Nanometer Structures*, 21(6):2990–2993, 2003. URL http://dx.doi.org/10.1116/1.1624259.

63. M. Song, K. Mitsuishi, M. Tanaka, M. Takeguchi, M. Shimojo, and K. Furuya. Fabrication of self-standing nanowires, nanodendrites, and nanofractal-like trees on insulator substrates with an electron-beam-induced deposition. *Applied Physics A: Materials Science & Processing*, 80:1431–1436, 2005. ISSN 0947-8396. URL http://dx.doi.org/10.1007/s00339-004-2997-z.

64. S. J. Randolph, J. D. Fowlkes, and P. D. Rack. Effects of heat generation during electron-beam-induced deposition of nanostructures. *Journal of Applied Physics*, 97(12):124312, 2005. URL http://dx.doi.org/10.1063/1.1942627.

65. G. Hochleitner, H. D. Wanzenboeck, and E. Bertagnolli. Electron beam induced deposition of iron nanostructures. *Journal of Vacuum Science & Technology B: Microelectronics and Nanometer Structures*, 26(3):939–944, 2008. URL http://dx.doi.org/10.1116/1.2907781.

66. I. Utke, T. Bret, D. Laub, Ph. Buffat, L. Scandella, and P. Hoffmann. Thermal effects during focused electron beam induced deposition of nanocomposite magnetic-cobalt-containing tips. *Microelectronic Engineering*, 73-74:553 – 558, 2004. ISSN 0167-9317. URL http://dx.doi.org/10.1016/j.mee.2004.02.084. Micro and Nano Engineering 2003.

67. R. Saris. Electron & ion beam induced deposition of tungsten. Bachelor report, Eindhoven University of Technology, 2009.

68. Ludwig Reimer. *Scanning electron microscopy: physics of image formation and microanalysis*. Springer, 1985.

69. Wei Li and David C. Joy. Study of temperature influence on electron beam induced deposition. *Journal of Vacuum Science & Technology A: Vacuum, Surfaces, and Films*, 24(3):431–436, 2006. URL http://dx.doi.org/10.1116/1.2187995.

70. M Weber. Scattering of non-relativistic electrons in tip structures. *Journal of Physics D: Applied Physics*, 27(7):1363, 1994. URL http://stacks.iop.org/0022-3727/27/i=7/a=004.

71. J. Mølgaard and W. W. Smeltzer. Thermal conductivity of magnetite and hematite. *Journal of Applied Physics*, 42(9):3644–3647, 1971. URL http://dx.doi.org/10.1063/1.1660785.

72. Lavaughn M. Fillman and Sunny C. Tang. Thermal decomposition of metal carbonyls: A thermogravimetry-mass spectrometry study. *Thermochimica Acta*, 75(1-2):71 – 84, 1984. ISSN 0040-6031. URL http://dx.doi.org/10.1016/0040-6031(84)85008-X.

73. Philip D Rack, Jason D Fowlkes, and Steven J Randolph. In situ probing of the growth and morphology in electron-beam-induced deposited nanostructures. *Nanotechnology*, 18(46):465602, 2007. URL http://stacks.iop.org/0957-4484/18/i=46/a=465602.

74. V Friedli, I Utke, K MÃÿlhave, and J Michler. Dose and energy dependence of mechanical properties of focused electron-beam-induced pillar deposits from cu(c 5 hf 6 o 2) 2. *Nanotechnology*, 20(38):385304, 2009. URL http://stacks.iop.org/0957-4484/20/i=38/a=385304.

75. Ping Chen, Huub W. M. Salemink, and Paul F. A. Alkemade. Smooth and narrow nanopillars fabricated by ion-beam-induced deposition under charging conditions. *Japanese Journal of Applied Physics*, 47(10): 8120–8123, 2008. URL http://dx.doi.org/10.1143/JJAP.47.8120.

76. M. Ishida, J. Fujita, T. Ichihashi, Y. Ochiai, T. Kaito, and S. Matsui. Focused ion beam-induced fabrication of tungsten structures. *Journal of Vacuum Science & Technology B: Microelectronics and Nanometer Structures*, 21(6):2728–2731, 2003. URL http://dx.doi.org/10.1116/1.1627806.

77. Kai He, David J. Smith, and Martha R. McCartney. Observation of asymmetrical pinning of domain walls in notched permalloy nanowires using electron holography. *Applied Physics Letters*, 95(18):182507, 2009. URL http://dx.doi.org/10.1063/1.3261753.

78. J.H. Franken. Domain wall motion in perpendicularly magnetized ultrathin pt/cofeb/pt films. Master's thesis, Eindhoven University of Technology, 2010.

79. P. J. Metaxas, P.-J. Zermatten, J.-P. Jamet, J. Ferré, G. Gaudin, B. Rodmacq, A. Schuhl, and R. L. Stamps. Periodic magnetic domain wall pinning in an ultrathin film with perpendicular anisotropy generated by the stray magnetic field of a ferromagnetic nanodot array. *Applied Physics Letters*, 94(13):132504, 2009. URL http://dx.doi.org/10.1063/1.3105988.

80. Ruquian Wu, Chun Li, and A.J. Freeman. Structural, electronic and magnetic properties of co/pd(111) and co/pt(111). *Journal of Magnetism and Magnetic Materials*, 99(1-3):71 – 80, 1991. ISSN 0304-8853. URL http://dx.doi.org/10.1016/0304-8853(91)90048-F.

81. Huang T. Zeng, D. Read, D. Petit, A. V. Jausovec, L. O'Brien, E. R. Lewis, and R. P. Cowburn. Combined electrical and magneto-optical measurements of the magnetization reversal process at a domain wall trap. *Applied Physics Letters*, 94(10):103113, 2009. URL http://dx.doi.org/10.1063/1.3098359.

82. COMSOL. Comsol multiphysics. Finite element analysis software, 2008. URL http://www.comsol.com.

83. M. J. Donahue and D. G Porter. *OOMMF user's guide*. National Institute of Standards and Technology, Gaithersburg, MD, 1999. URL http://math.nist.gov/oommf.

84. Harald Plank, Thomas Haber, Christian Gspan, Gerald Kothleitner, and Ferdinand Hofer. Controlling structure, chemistry, and morphology of free standing platinum nanorods via process parameters during electron beam induced deposition. In *FIB Workshop*. Graz University of Technology, June 2010. URL http://www.felmi-zfe.tugraz.at/FIB/WS5_Beitraege/Plank.pdf. Lecture Presentation.

85. David C. Joy. *Monte Carlo modeling for electron microscopy and microanalysis*. Oxford University Press, 1995.

86. David C. Joy. An introduction to monte carlo simulations. *Scanning Microscopy*, 5(2):329–337, 1991.

87. R. Browning. Universal elastic scattering cross sections for electrons in the range 1–100 kev. *Applied Physics Letters*, 58(24):2845–2847, 1991. URL http://dx.doi.org/10.1063/1.104754.

88. H Bethe. Zur theorie des durchgangs schneller korpuskularstrahlen durch materie. *Annalen der Physik*, 397 (3):325–400, 1930. URL http://dx.doi.org/10.1002/andp.19303970303.

89. DC Joy and S Luo. An Empirical Stopping Power Relationship for Low-Energy Electrons. *Scanning*, 11(4): 176–180, Jul-Aug 1989. ISSN 0161-0457.